ISBN: 978-93-48620-63-7

# PHYSICAL AND MATERIAL SCIENCE INNOVATION AND ITS SOCIETAL IMPACT

**Editors:**
**Dr. Jitendra Pal Singh**
**Dr. Atanu Nag**
**Dr. L. Anandaraj**
**Dr. Yogesh Kumar Sharma**

Bhumi Publishing, India
First Edition: March 2025

# Physical and Material Science Innovation and its Societal Impact

(ISBN: 978-93-48620-63-7)

## Editors

**Dr. Jitendra Pal Singh**

Department of Physics,

School of Sciences, IFTM University,

Moradabad, Uttar Pradesh

**Dr. Atanu Nag**

Department of Physics,

School of Sciences, IFTM University,

Moradabad, Uttar Pradesh

**Dr. L. Anandaraj**

Department of Physics,

Sacred Heart College (Autonomous),

Tirupattur-Dt, Tamilnadu

**Dr. Yogesh Kumar Sharma**

Professor in Physics and Principal,

Mahayogi Guru Gorkhnath Govt. Degree

College, Bithyani, Yamkeshwar

(Pauri Garhwal) Uttarakhand

Bhumi Publishing

**March 2025**

Title: Physical and Material Science Innovation and its Societal Impact

Editors: Dr. Jitendra Pal Singh, Dr. Atanu Nag, Dr. L. Anandaraj, Dr. Yogesh Kumar Sharma

First Edition: March 2025

ISBN: 978-93-48620-63-7

**Published by:**

**BHUMI PUBLISHING**

**Nigave Khalasa, Tal – Karveer, Dist – Kolhapur, Maharashtra, INDIA 416 207**

**E-mail:** bhumipublishing@gmail.com

## ***PREFACE***

*In today's era; Scientific and Technological Innovation have always played a driving role in the advancement of human civilization and the associated societal transformation. With the constant evolution of humankind, new trends in scientific advancement and technological exploration materialize, offering ground-breaking solutions to the societal challenges. Research in physical science and material science holds incomparable significance for the scientific and technological development of humankind.*

*This book, Physical and Material Science Innovation and its Societal impact, highlights some of the most innovative advancements of physical science and material science researchers to collaborate under one roof in order to advance for some relevant impact on the society. This book brings together prominent academic scientists, researchers, and research scholars of physical and material sciences to discuss and share their knowledge and research findings on different areas of physical and material science. Our goal is to provide a great platform for the basic and advanced outstanding research from the most fundamental theoretical and practical works in the relevant field.*

*The chapters in this book cover a diverse range of fields, each contributing to the relevant theme of scientific innovation. Whether it is physical science or material science or any interdisciplinary field; the research presented in this book demonstrates unique approaches of recent physical science and material science research by qualified academicians of reputed higher educational institutions.*

*We anticipate this book serves as a resource for academicians, practitioners, and educators to present and debate the latest discoveries, trends, concerns, practical difficulties, solutions in their domains to adopt innovative approaches in their own work. By embracing the spirit of innovation, we can collectively bring new possibilities to construct a brighter, more sophisticated future for physical science and material science researchers.*

**- Editors**

## TABLE OF CONTENT

# GREEN EMISSION PROPERTIES OF L-TYROSINE GUANIDINE CARBONATE SINGLE CRYSTAL

**L. Anandaraj*[1], K. Venkatesan[2] and Jitendra Pal Singh[3]**
[1]PG and Research Department of Physics,
Sacred Heart College (Autonomous), Tirupattur-635601, India
[2]Department of Physics,
Sri Vidya Mandir Arts and Science College, Uthangarai - 636902, India
[3]Department of Physics, School of Sciences, IFTM university, Moradabad-244102, India
* Corresponding author E-mail: anandaraj1828@gmail.com

**Abstract:**

A new Non-linear optical material L-tyrosine Guanidine Carbonate single crystal is synthesized by slow evaporation solution growth technique at room temperature using water as solvent. Good transparent LTGC crystal is sized. Single crystal X-ray diffraction reveals the crystal belongs to the Tetragonal P structure and a space group of P41212. The sharp intense peak in Powder XRD analysis confirms the good crystalline nature and purity of the crystal. The presence of various functional groups and their modes of vibration were identified by FTIR spectral analysis. The UV-Vis spectroscopic study shows that the lower cut-off wavelength is 234.6 nm with wide transparency range and very low absorbance. The optical band gap spectrum shows the Energy gap of the crystal is about 5.6 eV. The LTGC was subjected to fluorescence analysis and it was ascertained that the maximum emission was in green region at 532.4 nm. The mechanical behavior was studied by Vickers microhardness test.

**Keywords:** Single Crystal XRD, Microhardness, Fluorescence.

## 1. Introduction:

The researchers are encouraged in the recent days to grow a nonlinear optical (NLO) material due to their high optical transparency, high laser damage threshold, extremely high optical response, wide phase angle and high mechanical strength [1-3]. Wide range of applications in the field of optical switching optoelectronics, optical data storage, optical communication and telecommunication etc., are in the current research of NLO material [4-6]. For NLO applications the amino acids are interesting organic nonlinear optical material, a compound with improved NLO activity and mechanical, thermal stability is formed when the amino acids are coordinated with strong acids or metallic bonds [9]. Some organic NLO materials having less environmental stability, poor optical and mechanical property, low laser damage threshold and poor phase matching property due to their weak Vander Waal bonds. The growths of semi-organic crystal were used to overcome this difficulty second order optical nonlinearity, high transparency range, high nonlinear co efficient, high mechanical stability and high laser damage threshold etc. [5]. By slow evaporation method the semi-organic crystal was grown and which is crystallized by monoclinic system with non-Centro symmetric space group P41212. KDP, $ZnO_4$ doped Zno4 are inorganic materials potassium lithium niobite, are niobite crystals borate crystals like lithium triborate have been already reported to NLO active materials. Materials like glycine selenite proves to be highly NLO active. Lithium sulphate family are excellent NLO materials also many new crystals in the material. Compounds is already reported and the title is detailed structure and analyzed [10]. Remarkable changes in the properties of inorganic crystals recently it confirmed that the effect of dopants. The properties of the material such as transparency, reflectance, refractive index, optical electrical conductivity, electrical susceptibility, dielectric constant, Mayer's number, stiffness constant, yield strength, fracture toughness and brittle index is varied by adding dopants to the undoped inorganic crystals.

In advanced laser technology and telecommunication applications the ferromagnetic and nonlinear optical material plays a huge role. In the field of electronic industries, the NLO material have a vast range of demand, so to enhance the properties of a material it is require to synthesis a new NLO. Considering all the above facts, L-tyrosine and guanidine carbonate single crystals have been synthesized and grown at low cost. L-tyrosine, a natural amino acid, is a major nutrient having a phenolic hydroxyl group [8]. L-tyrosine is a centrosymmetric molecule, when coordinated with metal ions it becomes non-centrosymmetric materials and these metal-organic coordination compounds have attracted attention for their considerable high NLO coefficients, favor physico-chemical properties [9]. Guanidine is a strong base that readily protonated by most organic acids with the resulting guanidine species being useful for molecular assembly purposes, forming hydrogen bonding associations through its six donor protons [10].

The grown crystal was subjected to powder X-ray diffraction due to the single crystal X-ray diffraction the crystalline system and space groups are determined and the functional groups are analyzed with help of FTIR. Using a UV-Visible analysis, the optical transmission and optical absorption was studied and the fluorescence study exhibits that material having a green color emission.

## 2. Experimental procedure:

The L-tyrosine was prepared in an equimolar ratio of 1:1, diluted in distilled water using a magnetic stirrer and filtered through Whatman filter paper. Guanidine carbonate, on the other hand, was produced at an equimolar ratio of 1:1 and dissolved in distilled water using a magnetic stirrer before being filtered through Whatman filter paper [11]. The filtered L-tyrosine and Guanidine carbonate solutions were then combined in a single beaker and agitated for 1 hour before being filtered again with Whatman filter paper. For the slow evaporation procedure, the solution was held at a steady temperature.

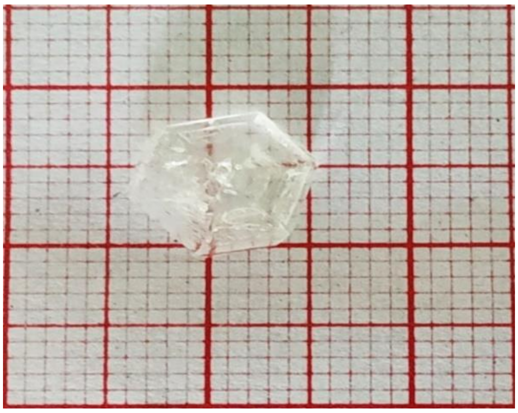

**Fig. 1: Photograph of L-tyrosine Guanidine carbonate single crystals**

## 3. Characterization studies:

### *3.1. Single crystal XRD*

Single crystal XRD studies are carried out to obtain reliable details on lattice characteristics that are comparable to powder XRD research. For the xrd analysis and cell parameter calculations, a fitting crystal size was chosen [12]. The Tetragonal P system is associated with L-tyrosine and Guanidine carbonate crystals, according to a single XRD result.

Bruker D8 VENTURE SC-XRD equipped with MoKα radiation was used to collect the unit cell dimensions and X-ray intensity data of LTGC [8]. The crystal belongs to the Tetragonal P structure, with unit cell dimensions of a=6.982 Å; b=6.982 Å; c=19.635 Å; α=90°; β= 104.24°; γ=90° and a space group of P41212. The obtained lattice parameters are displayed in table 1.

**Table 1: Lattice Parameters**.

| **Identification code** | **Crystal system** |
|---|---|
| Crystal system | Tetragonal P |
| Space group | P41212 |
| Unit Cell dimensions | a=6.982Å, b=6.982Å, c=19.635Å, α=90°, β=104.24°, γ=90° |
| Volume | 957.173 $Å^3$ |

### *3.2 Powder XRD analysis*

Powder XRD was performed on L-tyrosine and Guanidine carbonate crystals using a Rich Seifert diffractometer with CuK radiations of wavelength 1.5418 [15]. The powder XRD pattern of LTGC is shown in the figure 2. The peaks detected in the XRD spectrum were analyzed and indexed, and the produced crystals belong to the orthorhombic system, with the computed lattice parameters agreeing well with the data acquired from a single XRD.

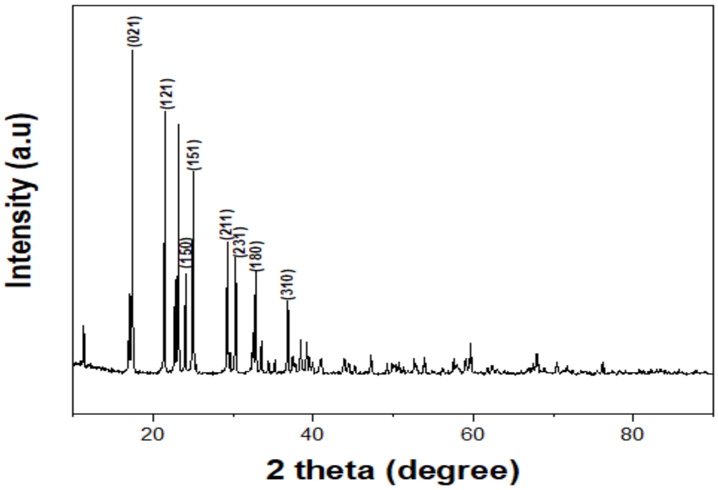

**Fig. 2: Powder X-Ray diffraction pattern for LTGC**

### *3.3. FTIR Analysis*

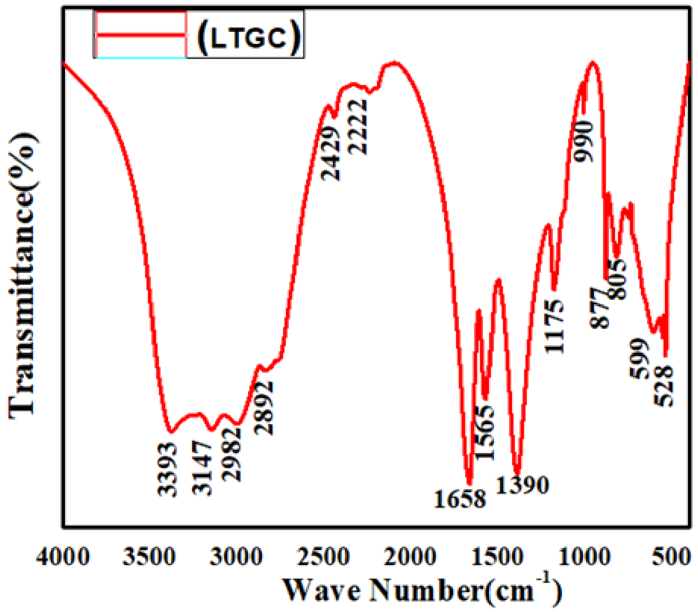

**Fig. 3: FTIR spectrum of LTGC**

**Table 2: FTIR analysis**

| S. No. | Wave Number (cm$^{-1}$) | Functional group |
|---|---|---|
| 1 | 528 | C-C-C (Bending) |
| 2 | 805 | $NH_2$ (Stretching) |
| 3 | 877 | $CH_2$ (Stretching) |
| 4 | 990 | CH (Stretching) |
| 5 | 1390 | OH (Bending) |
| 6 | 1658 | (C(N)=O) (Carbonyl Stretching) |
| 7 | 3147 | OH (Stretching) |

Spectral analysis is used in Fourier Transform Infrared spectrometers to analyses molecule structure and chemical bonding. 3000 $cm^{-1}$ – 2500 $cm^{-1}$ stretching vibration of OH band in $H_2O$ absorbed by a sample can be attributed to the sample that occurs at the peak. The peak is attributed to the stretching vibration $CH_2$ band at 2441 $cm^{-1}$ and 2239 $cm^{-1}$. The carbonyl stretching vibration of (C(N)=0) bands produces the peak attributed to 1665 $cm^{-1}$.

### *3.4 UV-Visible spectral analysis*

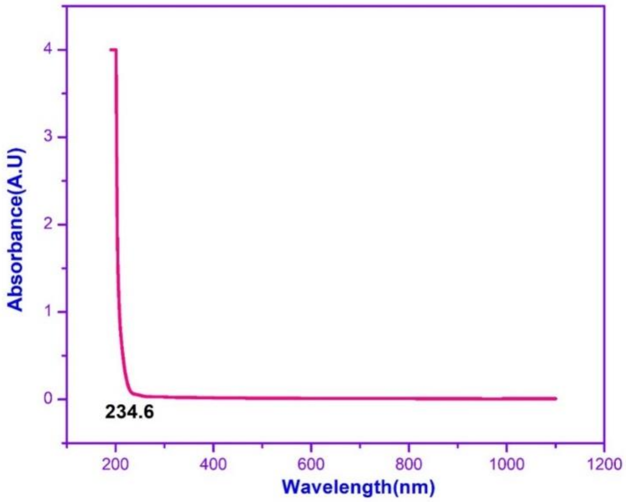

**Fig. 4: UV-Visible Absorbance spectrum of LTGC**

The absorbance of L-tyrosine and Guanidine carbonate crystal is shown in the diagram above. In the region of 200-1200 nm, the L-tyrosine and Guanidine carbonate crystal absorbs light[16]. The lower cutoff wavelength for the absorption spectrum is 234.6 nm. The spectrum demonstrates that it will absorb a specific wavelength of light from the source while transmitting all other visible wavelengths. The crystal's low absorption indicates that it can transmit a laser beam in the 200-1200 nm range. It demonstrates the crystal's transparency.

### *3.5 UV -Visible band gap spectrum LTGC crystal*

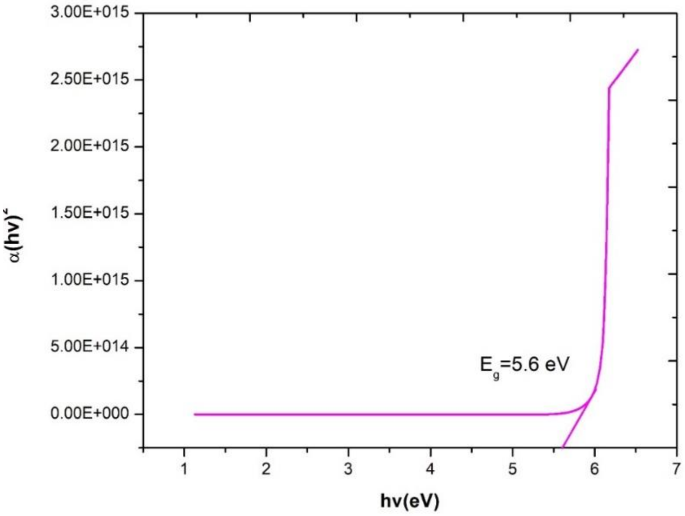

**Fig. 5: UV-Visible spectrum of band gap for LTGC**

The wavelength of the optical cut-off is found to be 234.6 nm. We may use the formula to get the absorption coefficient using that cut-off wavelength value.

$$\alpha = \frac{2.3023 \log 1}{t}$$

where, α – absorption co-efficient, T – transmittance, t – thickness of the crystal.

The band gap of a LTGC crystal is determined by using a following relation,

$$Eg = (\alpha hv)^2/hv$$

The LTGC crystal has a large optical band gap of 5.6eV, making it appropriate for optoelectronics applications.

### *3.6 Fluorescence Study*

L-tyrosine and Guanidine carbonate crystals were identified from the fluorescence spectrum. With the help of a VARIAN CARY ECLIPSE fluorescence spectrometer, the sample is placed at ambient temperature. The fluorescence emission spectra were measured in the 500-700 nm range [17]. The big peak and the tiny peak are both GREEN in color. The tiny peak's range is around 582.4 nm, while the high peak's range is around 532.4 nm.

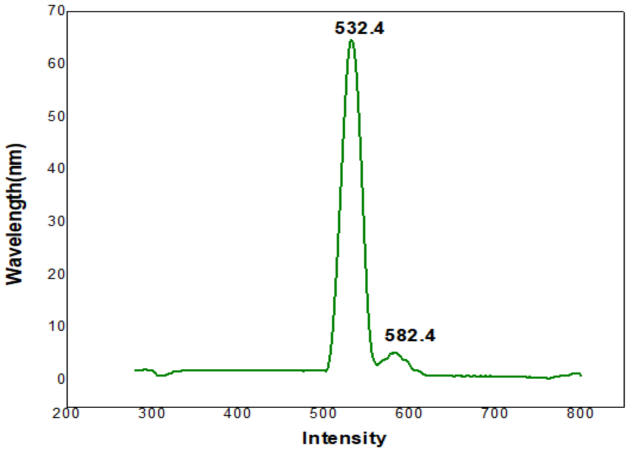

**Fig. 6: Fluorescence study of LTGC**

### *3.7 Micro Hardness Analysis*

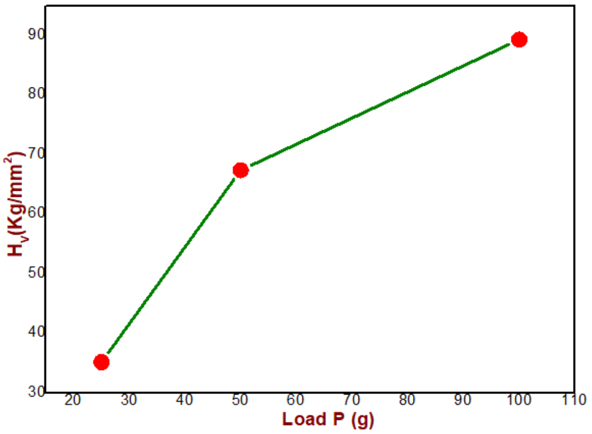

**Fig. 7: Load P and Vs Hardness number of LTGC**

A micro hardness tester is used to investigate the mechanical properties of the LTGC single crystal. The hardness of a material is a measure of its resistance to deformation. The micro hardness characterization is just as important as the device fabrications, and this investigation of the produced LTGC crystals was done at room temperature using the Vickers hardness test.

The generated crystal's Vickers hardness number was estimated using the formula

$$Hv = (1.854P)/d^2 \text{ Kg/mm}^2.$$

Where Hv is the Vickers hardness number in kilograms per square meters, and
Kg/mm2 is the Vickers hardness number in kilograms per square metre.
P denotes the applied load in kilograms.
D is the indentation mark's average diagonal length in millimeters.
The hardness number (Hv) and the applied load P were shown on a graph. The graph shows that the value of toughness increases as the number of people increases.

## 4. Conclusion

A new nonlinear semi – organic material of L–tyrosine with Guanidine carbonate was synthesized by slow evaporation method. The functional group and molecular structure of the material was concluded by FTIR analysis. The single crystal XRD confirmed that the grown LTGC crystal was said to be TETRAGONAL P system and it exhibit a P41212 space group and lattice parameters a=6.982Å, b=6.982Å and c=19.635Å. The UV cutoff wavelength was found to be 234.2 nm and it shows that material has a good candidate of NLO. The emission spectrum of LTGC is around 532.4 nm which exhibit a green color emission.

## References:

[1] Ilayabarathi, P., J. Chandrasekaran, and P. Maadeswaran. "Synthesis, growth and characterization of l-tyrosine hydrochloride a semi-organic nonlinear optical crystal", Optik - International Journal for Light and Electron Optics, 2012.

[2] Debanjan Sankar, Jui-Chen Yang, Anirban Sen Gupta, * Stephanie T. Lopina. Synthesis and characterization of L-tyrosine based polyurethane for biomaterial applications, published online 21 May 2008 in Wiley Interscience. DOI: 10.1002/jbm.a.32095.

[3] P. Rajasekar, K. Tamizharasan Enhanced optical, structural and thermal properties of copper (0.5, 1 and 1.5 mol %) doped sodium acid phthalate single crystals, J.mater.sci. ( 2018) 29: 6012-6018. http://doi.org/10.1007/s19854-018-8575-5.

[4] S.Nirmala Sri Devi, R. Arun kumar, E.K. Girija, Investigations on the effect of transition metals on the growth and characterization of sodium acid phthalate single crystals, optik 2015 / 0030-4026 http://dx.doi.org/10.1016/j.ijleo.2015.11.176

[5] R. Manimegalai, A. Puhal Raj, C. Ramachandra raja, Growth and Characterization of Ethylene Diamine Tetra Acetate (EDTA) Doped Lithium Sulphate monohydrate crystals, Optics and Photonics Journal, 2012,2,216-22, http://dx.doi.org/10.4236/opj.2012.223033.

[6] R. Manimekalai, A. Antony Joseph, C. Ramachandra Raja, Crystal growth and spectroscopic characterization of Aloevera amino acid added lithium sulfate monohydrate: A non - linear optical crystal, Elsevier, Molecular and Biomolecular spectroscopy 122 (2014) 232-237, http://dx.doi.org/10.1016/j.saa.2013.11.085.

[7] D. Sathya1, V. Sivashankar2, D. Prem Anand3, Growth and characterization of Guanidine benzoate (GuBzt).

[8] D. Saravanan, V.P. Senthil, S. Gokulraj, G. Sudalai raja, G. Anbalagan, G. Ramesh kumar, Growth of Bulk Sodium Acid Phthalate (NaAP) crystals for high frequency laser generation in nonlinear optical applications, Elsevier 4(2017)758-762

[9] P. Aishwarya, E. Ilango, G. Ramalingam, V. Vetrivelan. "Growth and characterization of Ltyrosine magnesium chloride single crystal: A promising NLO crystal", Materials Today: Proceedings, 2021

[10] R. Priya, S. Krishna, C. Justin Raj and S. Jerome das, Growth and characterization of NLO active lithium sulphate monohydrate single crystals, NO. 12, 1272-1276 (2009) DOI 10.1002 / crat.200900504

[11] S. Nandhini, K. Sudhakar, S. Muniyappan, P. Murugakoothan. "Growth and Characterization of a Potential Organic NLO Single Crystal: Guanidinium 4-Aminobenzene Sulfonate (GuAS)", Materials Today: Proceedings, 2019

[12] Singh, N. "Growth and characterization of new nonlinear optical thiourea l-alanine acetate single crystal", Journal of Crystal Growth, 20081001

[13] Praveen Menezes, Anthoni, A Jayarama, and Seik Weng Ng. "Synthesis, crystal growth and characterization of a D-π-A type novel organic nonlinear optical single crystal", Journal of Crystal Growth, 2014.

[14] N. R. Rajagopalan, P. Krishnamoorthy. "Growth and Characterization of Bis(thiourea) Antimony Tribromide: A Reliable Non-Linear Optical Crystal", Journal of Inorganic and Organometallic Polymers and Materials, 2016

[15] Growth and Characterization of Strontium Chloride Added Nicotinic Acid Single Crystals S. Chidambaram, A. David Kalaimani Raj, R. Punniyamoorthy, R. Manimekalai

[16] Study on Second Order Nonlinear Properties of Organic Material: Guanidine Hydrogen Maleate Single Crystals D. Sathya, V. Sivashankar, S. Anbarasu & D. Prem Anand

[17] Growth and Characterization of L-Tyrosine Zinc Acetate Single Crystals: A Promising Material for Opto-Electronic Applications Ilango, Aishwarya Sathyaseelan and Vetrivelan

# NANOSCALE MATERIALS: PROPERTIES, SYNTHESIS, CHARACTERIZATION AND APPLICATIONS

**Priya Paneru*[1], Munish Kumar[2], Vidhi Goyal[1], Ajeet Singh[1], Manish Kumar[1], Atanu Nag[1], Jitendra Pal Singh[1], Narender Singh[1] and Bal Krishna Yadav[1]**
[1]Department of Physics, School of Sciences, IFTM University, Moradabad, U.P., India
[2]Department of Physics,
G. B. Pant University of Agriculture and Technology, Pantnagar- 263145, India
*Corresponding author E-mail: priya.paneru@iftmuniversity.ac.in

**Abstract:**

Nanomaterials, defined by their nanoscale dimensions (typically less than 100 nanometers), exhibit unique physical, chemical, mechanical, and optical properties that differ significantly from their bulk counterparts. These materials form the foundation of nanotechnology and are classified into various types, including nanoparticles, nanotubes, nanowires, and nanocomposites. Their high surface area, quantum effects, and tunable properties enable diverse applications in medicine, electronics, energy, and environmental science. Understanding the fundamental principles of nanomaterials, including their synthesis, characterization, and behaviour, is essential for harnessing their potential in advanced technological and industrial applications. Nanomaterials, characterized by their nanoscale dimensions and unique physicochemical properties, have gained significant attention due to their wide-ranging applications. The synthesis of nanomaterials involves various techniques, including physical, chemical, and biological methods, each influencing their size, shape and functional properties. Characterization techniques such as electron microscopy, spectroscopy, and X-ray diffraction are essential for analyzing their structure, composition and performance. These materials have transformative applications in medicine, electronics, energy storage, catalysis and environmental remediation. Understanding the synthesis, characterization and applications of nanomaterials is crucial for advancing nanotechnology and developing innovative solutions across multiple scientific and industrial domains.

**Keyword:** Nanomaterial, Properties, Characterisation, Synthesis.

## 1. Introduction:

The term "nano" originates from the Greek word "nanos," meaning dwarf. In scientific terms, "nano" refers to one-billionth of a meter ($10^{-9}$ meters). Materials display special qualities at this extraordinarily small scale that are very different from those of their bulk counterparts. This field, known as nanotechnology, involves the manipulation, control, and application of materials and devices at the nanometer scale [1]. Nanotechnology is the scientific discipline that deals with materials, systems and devices at the nanometer scale, typically ranging from 1 to 100 nanometers. It involves the manipulation and control of matter at the atomic and molecular levels to develop new materials with unique properties. Nanotechnology has revolutionized various scientific fields, including medicine, electronics, energy and environmental science. The fundamental principle behind nanotechnology is that when materials are reduced to the nanoscale, their physical, chemical and biological properties change dramatically compared to their bulk counterparts. This is due to the increased surface area-to-volume ratio, quantum effects and altered electronic structure. The development of nanotechnology has led to the creation of highly efficient catalysts, advanced drug delivery systems, high-performance materials and miniaturized electronic components [2]. The interdisciplinary nature of nanotechnology, integrating physics, chemistry, biology, and engineering, has accelerated its applications in various sectors, offering promising solutions for global challenges.

Nanomaterials, the building blocks of nanotechnology, are materials that exhibit unique nanoscale properties due to their reduced dimensions. These materials can be classified into various types based on their composition, structure, and dimensionality. For instance, carbon-based nanomaterials like graphene and carbon nanotubes exhibit remarkable electrical conductivity, mechanical strength and thermal stability, making them ideal for applications in flexible electronics, energy storage and structural reinforcement. Similarly, metallic and semiconductor nanoparticles such as gold, silver and zinc oxide possess optical, antibacterial and photocatalytic properties, which are widely used in medical imaging, drug delivery and environmental remediation [3]. The synthesis of nanomaterials can be achieved through top-down (e.g., lithography, milling) or bottom-up (e.g., chemical vapor deposition, self-assembly) approaches, each offering different advantages in terms of precision and scalability. Despite the remarkable benefits of nanomaterials, concerns related to toxicity, environmental impact, and long-term stability must be addressed to ensure their safe and sustainable use.

The impact of nanotechnology and nanomaterials on modern industries and daily life is profound. In medicine, nanotechnology has paved the way for targeted drug delivery systems, allowing for precise treatment of diseases such as cancer while minimizing side effects. In electronics, nanomaterials have enabled the development of faster, smaller and more efficient transistors, memory devices and flexible displays. The energy sector has also benefited from nanotechnology, with advancements in solar cells, batteries and fuel cells improving energy efficiency and sustainability. Additionally, nanotechnology plays a critical role in environmental protection, offering solutions for water purification, air filtration and waste management. However, as nanotechnology continues to evolve, ethical considerations, regulatory frameworks and risk assessments must be addressed to mitigate potential hazards associated with nanomaterials. Future research in this field aims to develop greener synthesis methods, improve the biocompatibility of nanomaterials and harness their potential for solving pressing global issues such as climate change, disease prevention and resource scarcity [4-6].

## 2. Understanding the Nanoscale

### *2.1What is the Nanoscale?*

The nanoscale refers to a size range typically between 1 and 100 nanometers (nm), where materials exhibit unique physical, chemical and biological properties different from their bulk counterparts. A nanometer is one-billionth of a meter, making nanoscale objects incredibly small—comparable to the size of individual molecules and atoms. At this scale, the behavior of materials is governed by quantum mechanics rather than classical physics, leading to significant changes in optical, electrical and mechanical properties [7]. The high surfacearea-to-volume ratio at the nanoscale enhances reactivity, making nanomaterials highly effective in applications such as catalysis, drug delivery and energy storage. For example, gold, which appears yellow in the bulk form, can exhibit different colors at the nanoscale due to changes in its electron behavior and light absorption properties [8].

The significance of the nanoscale extends across various scientific and technological fields, including medicine, electronics and environmental science. In nanomedicine, nanoparticles are used for targeted drug delivery, allowing precise treatment of diseases while reducing side effects. In electronics, nanoscale transistors enable the development of smaller, faster and more efficient devices such as smartphones and quantum computers. Additionally, nanoscale materials contribute to the advancement of renewable energy technologies, including high-efficiency solar cells and supercapacitors [9]. However, working at the nanoscale presents challenges, such as controlling material properties, potential toxicity concerns and difficulties in large-scale manufacturing. Understanding and harnessing the nanoscale is crucial for the continued development of nanotechnology, enabling groundbreaking innovations that impact various aspects of modern life.

The following table provides a comparison of the sizes of various materials

**Table 1: Size Comparison of Materials**

| Material | Approximate Size |
|---|---|
| Water molecule | ~0.3 nm |
| DNA strand | ~2 nm |
| Virus | ~20-300 nm |
| Bacteria | ~500-5000 nm |
| Red blood cell | ~7,000 nm |
| Human hair | ~80,000-100,000 nm |
| Grain of sand | ~500,000 nm |

**Table 2: A table highlighting significant discoveries in nanoscience and nanotechnology that have been recognized with Nobel Prizes**

| Year | Discovery | Nobel Laureates | Nobel Prize Category |
|---|---|---|---|
| 1996 | Discovery of fullerenes ($C_{60}$), a new form of carbon molecule. | Harold Kroto, Richard Smalley, Robert Curl | Chemistry |
| 2007 | Discovery of giant magnetoresistance, a quantum mechanical effect in thin film structures. | Albert Fert, Peter Grünberg | Physics |
| 2010 | Isolation of graphene, a single layer of carbon atoms with exceptional properties. | Andre Geim, Konstantin Novoselov | Physics |
| 2016 | Design and synthesis of molecular machines, paving the way for advancements in nanorobotics. | Jean-Pierre Sauvage, Fraser Stoddart, Bernard Feringa | Chemistry |
| 2023 | Discovery and synthesis of quantum dots, nanoparticles with size-dependent optical properties. | MoungiBawendi, Louis Brus, Alexei Ekimov | Chemistry |

### *2.2 Unique Properties at the Nanoscale*

Materials at the nanoscale exhibit size-dependent properties, including:

**(a) Enhanced Strength:** Nanomaterials often exhibit superior mechanical strength compared to their bulk counterparts, primarily due to their high surface area-to-volume ratio and nanoscale interactions. At the atomic level, reducing the size of a material alters its structural properties, making it less prone to defects such as dislocations, which are common in bulk materials. For example, carbon nanotubes and graphene possess extraordinary tensile strength, making them ideal for reinforcing composite materials used in aerospace, automotive and construction industries. Additionally, nanoceramics and nanometals display enhanced hardness and wear resistance, contributing to their application in protective coatings and biomedical implants. The improved strength of nanomaterials not only extends the lifespan of materials but also reduces their weight, leading to innovations in lightweight yet durable materials[10].

**(b) Optical Properties:** At the nanoscale, materials exhibit unique optical properties due to quantum confinement effects, which alter their interaction with light. Unlike bulk materials, nanoparticles can display distinct colors and fluorescence based on their size, shape and composition. For instance, gold nanoparticles, which appear yellow in bulk form, can exhibit red, blue, or even green hues at the nanoscale due to localized surface plasmon resonance (LSPR). Similarly, semiconductor quantum dots, such as cadmium selenide (CdSe), emit different colors when excited by light, making them valuable in bioimaging, display technologies and light-emitting diodes (LEDs). These unique optical behaviors enable the development of advanced imaging techniques, high-efficiency solar cells and innovative sensors with enhanced sensitivity and accuracy [11].

**(c) Electrical Conductivity:** Nanomaterials have revolutionized the field of electronics due to their exceptional electrical conductivity. Materials like graphene, carbon nanotubes and silver nanowires exhibit high electron mobility, enabling faster and more efficient electronic devices. Graphene, for instance, has nearly zero electrical resistance, making it an excellent candidate for next-generation transistors, flexible electronicsand transparent conductive films. Carbon nanotubes, known for their unique one-dimensional structure, provide superior conductivity and thermal stability, making them suitable for nanoelectronic circuits and high-performance batteries [12]. The integration of these nanomaterials into semiconductor and computing technologies has the potential to enhance processing speeds, reduce energy consumptionand enable the development of ultra-miniaturized electronic components.

**(d) Chemical Reactivity:** One of the most significant advantages of nanomaterials is their enhanced chemical reactivity, which stems from their high surface area-to-volume ratio. This property makes them highly effective catalysts in chemical reactions, improving efficiency in applications such as drug delivery, environmental remediation and industrial processing. For example, titanium dioxide ($TiO_2$) nanoparticles are widely used as photocatalysts for breaking down pollutants in water and air purification systems. In medicine, silver nanoparticles exhibit strong antibacterial properties, making them valuable in wound dressings, coatings and antimicrobial agents [13]. Additionally, nanomaterials play a crucial role in energy storage and conversion, such as in fuel cells and hydrogen production, by facilitating faster and more efficient reactions. However, their increased reactivity also raises concerns about toxicity and environmental impact, necessitating further research to ensure their safe and sustainable use.

## 3. Principles of Nanotechnology:

**(a) Quantum Effects:** At the nanoscale, quantum mechanics governs the behavior of materials, leading to unique and unpredictable properties compared to their bulk counterparts. Unlike classical physics, where electrons move in continuous energy bands, nanoscale materials exhibit discrete energy levels due to quantum confinement. This significantly impacts their electrical, optical and magnetic properties. For example, semiconductor quantum dots emit different colors of light depending on their size, making them valuable in bioimaging and display technologies. Similarly, nanomaterials like graphene and carbon nanotubes exhibit exceptional electrical conductivity due to altered electron movement, making them highly suitable for advanced nanoelectronics and energy applications. Quantum effects enable the development of highly efficient nanoscale devices, pushing the boundaries of technology in computing, communication and medicine [13,14].

**(b) Surface Area-to-Volume Ratio:** One of the most defining principles of nanotechnology is the dramatic increase in the surface area-to-volume ratio as the size of a material decreases. This means that a greater proportion of atoms or molecules are exposed at the surface, making nanomaterials highly reactive and efficient in various applications [14]. For example, nanoparticles used as catalysts in chemical reactions have significantly enhanced reactivity compared to bulk materials, improving industrial processes such as fuel production and environmental remediation. Similarly, nanomaterials in medicine, like drug carriers, interact more effectively with biological systems, enabling targeted drug delivery. This principle also plays a crucial role in adsorption-based applications, such as water purification and air filtration, where nanomaterials efficiently trap and remove contaminants.

**(c) Self-Assembly:** Nanotechnology leverages the natural phenomenon of self-assembly, where molecules and nanoparticles spontaneously organize into well-defined structures without external manipulation. This principle is particularly significant in biological systems, where proteins and DNA naturally fold into functional structures essential for life processes. In nanofabrication, self-assembly enables the creation of nanoscale devices with precision and efficiency, reducing the need for complex manufacturing techniques. For instance, block copolymers can self-assemble into nanostructures useful in developing high-density storage devices and advanced coatings [14]. Additionally, self-assembly is being explored in tissue engineering and regenerative medicine, where nanoscale scaffolds help guide the growth of cells into functional tissues. This approach paves the way for cost-effective, scalableand sustainable advancements in nanotechnology.

## 4. Types of Nanomaterials:

Nanomaterials are classified based on their composition and structural characteristics, leading to diverse applications in fields such as medicine, electronics, energy and environmental science. These materials exhibit unique physical and chemical properties that differ from their bulk counterparts, making them highly useful in advanced technologies. The three primary categories of nanomaterials include carbon-based nanomaterials, metal and metal oxide nanoparticles and polymeric and composite nanomaterials. Each type possesses distinct structural configurations and functionalities, allowing for their tailored use in specific applications [15].

### *4.1 Carbon-Based Nanomaterials*

Carbon-based nanomaterials are composed entirely of carbon and exhibit remarkable electrical, mechanical and thermal properties. These materials have revolutionized nanotechnology due to their exceptional strength, conductivity and flexibility.

**Fullerenes** are spherical carbon molecules arranged in a cage-like structure, resembling a soccer ball. They possess unique electrical and mechanical properties, making them suitable for applications in superconductors, drug delivery and nanomedicine. Their hollow structure allows them to be used as carriers for delivering drugs and other therapeutic agents.

**Carbon Nanotubes (CNTs)** are cylindrical structures composed of rolled graphene sheets. They have extraordinary tensile strength, lightweight characteristics and superior electrical and thermal conductivity. CNTs are widely used in reinforced composites, nanoelectronics, and energy storage devices such as batteries and supercapacitors.

**Graphene** is a single layer of carbon atoms arranged in a hexagonal lattice. It is known for its flexibility, exceptional electrical conductivity and mechanical strength. Graphene is utilized in flexible electronics, transparent conductive films, high-performance batteriesand biomedical applications. Due to its superior properties, graphene has the potential to revolutionize multiple industries, including computing, energy and biomedicine [16].

### *4.2 Metal and Metal Oxide Nanoparticles*

Metal and metal oxide nanoparticles consist of metallic elements or their oxides, exhibiting diverse functionalities such as optical, catalytic and antimicrobial properties. These nanoparticles have significant applications in medicine, environmental science and consumer products.

**Gold and Silver Nanoparticles** are widely used in medicine, electronics and sensors due to their biocompatibility and antimicrobial properties. Gold nanoparticles are commonly employed in targeted drug delivery, cancer therapy and biosensing, while silver nanoparticles are incorporated into antimicrobial coatings, textiles and medical devices.

**Titanium Dioxide ($TiO_2$) Nanoparticles** are extensively used in sunscreens, cosmeticsand photocatalytic applications. They provide effective UV protection in skincare products and serve as powerful photocatalysts in environmental remediation by breaking down pollutants in water and air.

**Zinc Oxide (ZnO) Nanoparticles** are well known for their antibacterial and UV-blocking properties. They are used in sunscreens, transparent electronics and antimicrobial coatings for healthcare and food packaging applications. ZnO nanoparticles also play a crucial role in photocatalysis and energy harvesting technologies.

### *4.3 Polymeric and Composite Nanomaterials*

Polymeric and composite nanomaterials are designed by integrating nanoscale polymers with other nanomaterials to enhance their mechanical, thermal and functional properties. These materials find applications in drug delivery, coatings and high-performance materials.

**Dendrimers** are branched polymeric nanostructures with a well-defined, tree-like architecture. They have a high degree of surface functionality, making them ideal for drug delivery, gene therapy and nanomedicine. Their ability to encapsulate drugs and target specific sites in the body has made them a promising tool in pharmaceutical research.

**Nanocomposites** are hybrid materials that incorporate nanoparticles into polymer matrices to improve their mechanical strength, electrical conductivity and thermal stability. These materials are used in automotive components, aerospace structures and packaging materials. Nanocomposites enhance product durability while reducing weight, making them ideal for applications requiring lightweight yet strong materials [17].

## 5. Classification of Nanomaterials Based on Structural Dimensions:

Nanomaterials are categorized into four main types based on their structural dimensions: zero-dimensional (0D), one-dimensional (1D), two-dimensional (2D) and three-dimensional (3D). Each of these classifications is determined by the number of dimensions within the nanoscale range (1–100 nm), which influences their unique properties and applications. These materials play a crucial role in advanced technologies, including electronics, medicine, energy storage and environmental remediation.

### *5.1 Zero-Dimensional (0D) Nanomaterials*

Zero-dimensional (0D) nanomaterials have all three spatial dimensions confined within the nanoscale (1–100 nm). Due to their quantum confinement effects, these materials exhibit unique optical, electrical and chemical properties that differ significantly from their bulk counterparts.

Examples of 0D nanomaterials include nanoparticles and quantum dots. Quantum dots are semiconductor nanocrystals that emit light at specific wavelengths depending on their size, making them valuable for applications in bioimaging, display technologies and solar cells. Metal nanoparticles, such as gold and silver, exhibit enhanced catalytic and antimicrobial properties, making them widely used in medical treatments, sensors and antibacterial coatings. Additionally, magnetic nanoparticles, such as iron oxide, are used in targeted drug delivery and imaging techniques in the medical field. The small size and high surface area of 0D nanomaterials make them highly reactive and efficient in various applications.

### *5.2 One-Dimensional (1D) Nanomaterials*

One-dimensional (1D) nanomaterials have two dimensions within the nanoscale range, while the third dimension is significantly larger. These materials exhibit unique mechanical, electrical and optical properties, making them essential for nanoelectronics, photonics and energy storage applications.

Examples of 1D nanomaterials include nanowires, nanorodsand nanotubes. Carbon nanotubes (CNTs) are cylindrical structures composed of rolled graphene sheets, known for their exceptional strength, electrical conductivity and thermal stability. They are widely used in lightweight composite materials, flexible electronics and energy storage devices like batteries and supercapacitors. Nanowires, such as silicon and gold nanowires, are used in nanoelectronic circuits, sensors and photodetectors due to their superior electrical properties. Nanorods, often made of gold or semiconductor materials, are applied in medical imaging, targeted drug delivery and catalysis. The high aspect ratio of 1D nanomaterials allows for efficient charge transport, making them essential for high-performance electronic devices.

### *5.3 Two-Dimensional (2D) Nanomaterials*

Two-dimensional (2D) nanomaterials have one dimension confined within the nanoscale while the other two dimensions extend beyond 100 nm. These materials exhibit exceptional electrical, mechanical and optical properties due to their high surface area and atomic-scale thickness.

Examples of 2D nanomaterials include thin films, nanolayers and graphene sheets. Graphene, a single layer of carbon atoms arranged in a hexagonal lattice, is one of the most well-known 2D nanomaterials. It has extraordinary electrical conductivity, mechanical strength and flexibility, making it ideal for applications in flexible electronics, transparent conductive films and energy storage. Transition metal dichalcogenides (TMDs), such as molybdenum disulfide ($MoS_2$), exhibit semiconducting properties and are used in transistors, optoelectronic devices, and photodetectors. Thin films and nanocoatings are widely employed in protective coatings, anti-reflective surfaces and photovoltaic cells. The unique properties of 2D nanomaterials enable advancements in nanotechnology, particularly in miniaturized electronic and optical devices.

### *5.4 Three-Dimensional (3D) Nanomaterials*

Three-dimensional (3D) nanomaterials are not confined to the nanoscale in any single dimension but contain nanostructured features that enhance their properties. These materials often consist of interconnected nanostructures that improve mechanical strength, porosity and functionality.

Examples of 3D nanomaterials include nanoporous materials, nanocomposites and aerogels. Nanoporous materials, such as metal-organic frameworks (MOFs) and mesoporous silica, have high surface areas and tunable pore structures, making them useful for gas storage, catalysis and drug delivery. Nanocomposites are hybrid materials that combine nanoparticles with polymers, ceramics, or metals to enhance mechanical, thermal and electrical properties. These materials are used in aerospace, automotive and biomedical applications. Aerogels, ultra-lightweight porous nanostructures, provide excellent thermal insulation and are used in energy-efficient building materials and space applications. The hierarchical structures of 3D nanomaterials make them highly versatile for various industrial and scientific applications [18].

## 6. Synthesis of Nanomaterials:

Nanomaterials exhibit unique properties that distinguish them from their bulk counterparts, primarily due to their size, shape and controlled synthesis conditions. The ability to manipulate these properties through synthesis techniques has enabled advancements in fields such as electronics, medicine, energy storage and environmental applications. The synthesis of nanomaterials is broadly categorized into two main approaches: bottom-up and top-down methods. Bottom-up approaches involve assembling nanomaterials from atomic or molecular precursors, while top-down methods involve reducing bulk materials to the nanoscale. Each method offers distinct advantages and the selection depends on factors such as material type, precision, scalability and intended application [19].

### *6.1 Bottom-Up Approaches*

Bottom-up approaches focus on assembling materials from atomic, molecular, or nanoscale building blocks to form nanostructures. These techniques provide precise control over the size, shape and composition of the nanomaterials, allowing for the design of highly tailored structures.

- **(a) Chemical Vapor Deposition (CVD):** This method involves introducing gaseous reactants into a reaction chamber, where they undergo chemical reactions on a substrate to form a solid thin film or nanostructure. CVD is widely used in the production of carbon nanotubes, graphene and semiconductor nanowires. Its advantages include high purity, uniformity and scalability, making it a preferred method in nanoelectronics and coatings.
- **(b) Solvothermal and Hydrothermal Methods**: These methods utilize high-pressure and high-temperature environments within a liquid medium to facilitate the controlled growth of nanocrystals. Hydrothermal synthesis occurs in aqueous solutions, while solvothermal synthesis involves organic solvents. These methods are commonly used for the production of metal oxide nanoparticles, quantum dots and other nanostructures, offering control over crystallinity, size and morphology.

Other bottom-up techniques include molecular self-assembly, electrodeposition and biosynthesis, each of which provides unique benefits for specific applications in nanotechnology.

### *6.2 Top-Down Approaches*

Top-down methods involve starting with bulk materials and progressively breaking them down to the nanoscale. These approaches often utilize physical and mechanical processes to shape or fragment materials into nanoparticles or nanostructures.

- (a) **Mechanical Milling:** This process involves using mechanical forces, such as ball milling, to break down bulk materials into nanoscale particles. Mechanical milling is widely used for producing nanopowders and is particularly effective for creating metal and ceramic nanoparticles. However, this method may result in structural defects and require post-processing treatments to enhance material properties.

(b) **Lithography:** Lithographic techniques, such as electron beam lithography, enable the patterning of nanoscale structures with high precision. This method is essential in semiconductor fabrication, where nanostructures are designed for microchips, transistors and other electronic components. Although lithography allows for precise structuring, it is often limited by high costs and complex fabrication processes.

Other top-down approaches include laser ablation, etching and high-energy radiation techniques, which are employed in advanced nanofabrication for various high-performance applications [20].

## 7. Characterization of Nanomaterials:

Characterization of nanomaterials is essential for understanding their unique properties and optimizing their applications in various fields, including electronics, energy storage, catalysis, and nanomedicine. Due to their extremely small size and high surface area-to-volume ratio, nanomaterials exhibit distinct physical, chemicaland optical properties that require specialized analytical techniques for accurate measurement. These techniques help determine critical parameters such as size, morphology, crystallinity, composition, surface chemistry and charge. A comprehensive characterization ensures the reproducibility, stability and functionality of nanomaterials for specific applications.

### *7.1 Microscopy Techniques*

Microscopy techniques are crucial for analyzing the morphology, size and structural features of nanomaterials at the nanoscale. These techniques provide high-resolution imaging and allow for direct visualization of nanoparticles and nanostructures.

**Transmission Electron Microscopy (TEM):** TEM uses electron beams to penetrate ultrathin samples, producing high-resolution images that reveal internal structures, crystallinity and particle size. It is widely used for analyzing nanoparticles, nanowires and quantum dots.

**Scanning Electron Microscopy (SEM):** SEM scans a focused electron beam across the sample surface, generating detailed images of surface morphology and topographical features. It is commonly used for assessing the shape and dispersion of nanomaterials.

**Atomic Force Microscopy (AFM):** AFM operates by scanning a sharp tip over the sample surface to measure topography and surface roughness. It provides three-dimensional profiling and can manipulate individual nanoparticles, making it valuable for nanomechanical studies.

### *7.2 Spectroscopic Techniques*

Spectroscopic techniques help determine the chemical composition, molecular interactions and electronic properties of nanomaterials. These techniques are essential for understanding functional groups, oxidation states and optical behaviors.

**X-ray Diffraction (XRD):** XRD identifies the crystalline structure and phase composition of nanomaterials by analyzing diffraction patterns produced when X-rays interact with atomic arrangements. It is widely used in materials science and semiconductor research.

**Fourier Transform Infrared Spectroscopy (FTIR):** FTIR detects molecular vibrations and functional groups, providing insights into the surface chemistry of nanomaterials. This technique is essential for studying surface modifications and interactions with biomolecules.

**X-ray Photoelectron Spectroscopy (XPS):** XPS analyzes surface elemental composition and oxidation states by measuring the energy of emitted photoelectrons [21]. It is crucial for understanding surface coatings, chemical bonding and electronic properties.

### *7.3 Particle Size and Surface Area Analysis*

Nanomaterial performance is strongly influenced by particle size and surface area, making it essential to measure these parameters accurately.

**Dynamic Light Scattering (DLS):** DLS measures the hydrodynamic size and size distribution of nanoparticles in liquid suspension. It is widely used in pharmaceutical and colloidal studies to assess nanoparticle stability.

**Brunauer-Emmett-Teller (BET) Analysis:** BET measures the specific surface area of nanomaterials based on gas adsorption. This is particularly important for applications in catalysis, adsorption and energy storage, where surface interactions play a key role.

### *7.4 Optical and Electronic Characterization*

Nanomaterials exhibit unique optical and electronic properties that require specialized techniques to analyze their absorption, emission and electronic structures.

**UV-Visible Spectroscopy:** This technique examines optical absorption and band gap properties, essential for applications in optoelectronics, photovoltaics and sensors. It is widely used to study quantum dots, metal nanoparticles and semiconductor nanomaterials.

**Photoluminescence (PL) Spectroscopy:** PL spectroscopy analyzes the emitted light from nanomaterials after excitation, providing information about electronic structures, defect states and energy transitions. It is extensively used in LED and display technologies.

### *7.5 Surface Charge Analysis*

Surface charge plays a crucial role in nanoparticle stability, aggregation and interactions in biological and chemical systems.

**Zeta Potential Measurement:** Zeta potential determines the electrostatic charge on the surface of nanoparticles, providing insights into colloidal stability and aggregation behavior [22]. A higher absolute zeta potential value indicates better stability, which is important for drug delivery and nanofluid applications.

## 8. Applications of Nanotechnology:

Nanotechnology is transforming multiple industries by introducing innovative solutions at the molecular level. Its unique ability to manipulate materials at the nanoscale has led to groundbreaking advancements in medicine, electronics, energyand environmental science. By enhancing efficiency, precision and functionality, nanotechnology is paving the way for new scientific discoveries and practical applications.

### *8.1 Medicine and Healthcare*

Nanotechnology has made significant contributions to medicine, particularly in drug delivery, diagnostics and regenerative medicine.

**Targeted Drug Delivery:** Traditional drug treatments often affect healthy cells along with diseased ones, leading to side effects. Nanocarriers, such as liposomes and polymeric nanoparticles, enable targeted drug delivery by directing therapeutic agents precisely to diseased cells, improving treatment efficacy and minimizing adverse effects. This approach is particularly beneficial in cancer therapy.

**Medical Imaging:** Nanoparticles and quantum dots enhance imaging techniques such as MRI, fluorescence imaging and computed tomography (CT) scans. These nanoparticles improve contrast and resolution, enabling early disease detection and more accurate diagnoses.

Tissue Engineering: Nanoscale scaffolds made of biocompatible materials, such as biodegradable polymers and hydrogels, promote cell growth and tissue regeneration [23]. These scaffolds mimic the natural extracellular matrix, supporting the development of artificial organs and wound healing applications.

### *8.2 Electronics and Computing*

Nanotechnology has revolutionized the electronics industry by enabling the development of smaller, faster and more energy-efficient devices.

**Nanochips and Transistors:** The miniaturization of electronic components, such as transistors and semiconductor chips, has led to the creation of powerful and compact devices. Nanotechnology allows for increased computing power while reducing energy consumption, enhancing the performance of smartphones, computers, and other digital devices.

**Flexible Electronics:** Materials like graphene and silver nanowires enable the development of bendable and stretchable electronics. These advancements have given rise to wearable technology, flexible displays and foldable smartphones, enhancing user convenience and device durability [23].

### *8.3 Energy Sector*

Nanotechnology plays a crucial role in improving energy generation, storage and efficiency.

**Efficient Solar Cells:** Conventional solar cells face limitations in energy conversion efficiency. Nanomaterials, such as perovskite nanoparticles and quantum dots, enhance light absorption and charge transport, significantly improving the efficiency of photovoltaic cells. This innovation makes solar energy more viable and cost-effective [24].

**Nanobatteries:** The development of nanostructured electrodes and electrolytes enhances the performance of rechargeable batteries. Nanobatteries store more energy in smaller, lightweight designs, improving the longevity and capacity of electric vehicle batteries, wearable devices and grid storage solutions.

### *8.4 Environmental Science*

Nanotechnology offers innovative solutions for addressing environmental challenges, including pollution control and resource conservation.

**Water Purification:** Nanofilters, composed of nanomaterials like carbon nanotubes and silver nanoparticles, effectively remove contaminants such as heavy metals, bacteria and toxins from water sources. These nanofilters enhance filtration efficiency and provide clean drinking water in areas facing water scarcity.

**Pollution Control:** Nanocatalysts accelerate the breakdown of toxic chemicals and pollutants, reducing environmental harm. They are used in air purification systems, industrial wastewater treatment and catalytic converters in vehicles to minimize harmful emissions [25,26].

## 9. Challenges and Ethical Considerations:

Despite its vast potential, nanotechnology presents several challenges related to safety, environmental impact, ethical concerns and regulatory frameworks. Addressing these issues is crucial to ensuring responsible development and implementation of nanotechnology in various fields.

### *9.1 Safety and Toxicity*

The interaction of nanomaterials with biological systems and the environment raises concerns about their potential toxicity.

**Health Risks:** Due to their small size, some nanoparticles can penetrate biological membranes, accumulate in organs and disrupt cellular functions. Studies have suggested that prolonged exposure to certain nanomaterials, such as carbon nanotubes and metal nanoparticles, may cause inflammation, oxidative stress, or even DNA damage, posing risks to human health. More research is needed to fully understand their long-term effects.

**Environmental Impact:** Nanoparticles can persist in air, water and soil, potentially disrupting ecosystems. Their small size and high surface reactivity may cause unintended consequences, such as bioaccumulation in aquatic organisms or toxicity in beneficial microbes. Proper disposal and recycling methods must be developed to minimize environmental contamination.

### *9.2 Ethical and Regulatory Issues*

As nanotechnology continues to evolve, it raises ethical and regulatory challenges that require careful consideration.

**Privacy Concerns:** The integration of nanosensors in surveillance and tracking devices has raised concerns about personal privacy and data security. These advanced sensors can be embedded in everyday objects, leading to potential misuse in monitoring individuals without their consent. Clear ethical guidelines must be established to prevent such violations.

**Regulation Challenges:** The rapid growth of nanotechnology has outpaced the development of comprehensive regulations. Governments and organizations face difficulties in assessing risks, ensuring safety standards and enforcing responsible usage. Updated policies and international cooperation are needed to create uniform regulations for nanotechnology applications in medicine, industry and consumer products.

## 10. Future Prospects of Nanotechnology:

The future of nanotechnology is filled with exciting possibilities, with continuous advancements shaping various fields.

**Nanorobotics:** The development of microscopic robots (nanobots) for medical applications could revolutionize healthcare. These nanorobots could navigate the bloodstream, deliver drugs with precision, repair damaged tissues and even assist in non-invasive surgeries. Such innovations hold the potential to significantly improve disease treatment and recovery times.

Quantum Computing: Nanoscale quantum dots and transistors are paving the way for ultra-fast quantum computing. Unlike traditional computers, which use binary bits (0s and 1s), quantum computers operate on quantum bits (qubits), enabling complex calculations at unprecedented speeds. This technology could transform fields such as cryptography, artificial intelligence and material science.

**Sustainable Nanotechnology:** Researchers are focusing on eco-friendly nanomaterials for renewable energy, pollution control and green manufacturing [27]. Innovations such as nanostructured catalysts for carbon capture, biodegradable nanomaterials and energy-efficient nanocoatings could contribute to sustainability and climate change mitigation.

## 11. Conclusion:

Nanotechnology has emerged as a transformative scientific discipline, offering groundbreaking advancements across diverse fields such as medicine, electronics, energy and environmental science. By manipulating materials at the nanoscale, scientists and engineers have unlocked unique properties—enhanced strength, superior electrical conductivity and remarkable optical behaviors—that were previously unattainable with bulk materials. These innovations have paved the way for applications like targeted drug delivery, flexible electronics, high-efficiency solar cells and advanced water purification techniques, ultimately improving the quality of life and driving technological progress.

However, alongside these advancements, nanotechnology presents significant challenges that require careful consideration. Issues related to the toxicity of nanoparticles, their long-term environmental impact and ethical concerns about privacy and surveillance must be addressed to ensure responsible and safe implementation. The rapid evolution of nanotechnology also poses regulatory challenges, necessitating updated policies and global cooperation to establish standardized safety guidelines. As research continues, a balance must be maintained between innovation and ethical responsibility, ensuring that nanotechnology serves humanity without compromising health or environmental sustainability.

Looking ahead, the future of nanotechnology is exceptionally promising, with emerging fields such as nanorobotics, quantum computing and sustainable nanomaterials set to revolutionize industries. Whether through precision medicine, ultra-fast computing, or eco-friendly innovations, nanotechnology is poised to drive the next era of scientific and industrial advancements. By fostering interdisciplinary collaboration, prioritizing safetyand addressing ethical considerations, society can harness the full potential of nanotechnology, unlocking new frontiers of discovery while ensuring a sustainable and responsible future.

**References:**

[1] R. P. Feynman, 1959. *There's Plenty of Room at the Bottom*. Engineering and Science, 23(5), 22-36.

[2] G.L. Hornyak, H.F. Tibbals, J. Datta and J.J. Moore, 2009. *Introduction to Nanoscience and Nanotechnology*, CRC Press, London.

[3] W. Qi, 2016.Nanoscopic thermodynamics. *Accounts of Chemical Research*49(9), 1587-1595.

[4] C.C. Yang and Y.W. Mai, 2014.*Thermodynamics at the nanoscale: A new approach to the investigation of unique physicochemical properties of nanomaterials*. Material Science and Engineering: R: Reports, 79(4), 1-40.

[5] M. Born and E. Wolf,2003. *Principles of Optics*, Cambridge University Press, Cambridge.

[6] W.D. Callister, 1997. *Materials Science and Engineering: An Introduction*, 4th edn. Wiley, New York.

[7] A. P.Alivisatos, 1996. Perspectives on the Physical Chemistry of Semiconductor Nanocrystals. *Journal of Physical Chemistry*, 100(3), 13226-13239.

[8] M. A. Ratnerand D. Ratner,2003. *Nanotechnology: A Gentle Introduction to the Next Big Idea*. Prentice Hall.

[9] G. V. Lowry,A.Avellan and L. M. Avellan, 2019. Opportunities and challenges for nanotechnology in the agri-tech revolution. *Nature nanotechnology*, 14(6), 517-522.

[10] Q.Wu, W. S.Miao, Y. D.Zhang, H. J. Gao and D.Hui, 2020. Mechanical properties of nanomaterials: A review. *Nanotechnology Reviews*, 9(1), 259-273.

[11] A. B. Asha and R.Narain, 2020. *Nanomaterials properties. In Polymer science and nanotechnology* (pp. 343-359). Elsevier.

[12] L. Bokobza, 2017. Mechanical and electrical properties of elastomer nanocomposites based on different carbon nanomaterials. *C*, 3(2), 10-12.

[13] S.Tanimizu, S. Shionoya, W. M. Yenand H. Yamamoto, 1999. *Principal phosphor materials and their optical properties* (pp. 177-200). Boca Raton, FL: CRC Press.

[14] G. A.Mansoori, 2005. *Principles of nanotechnology: molecular based study of condensed matter in small systems*. World Scientific Publishing Company.

[15] C. J. Brinker and J.W. Scherer, 1990. *Sol-Gel Science: The Physics and Chemistry of Sol-Gel Processing*, Academic, Boston.

[16] M. Sajid, 2022. Nanomaterials: types, properties, recent advances, and toxicity concerns. *Current Opinion in Environmental Science & Health*, 25(1), 100319-100330.

[17] C. Buzea and I.Buzea, 2016. *Nanomaterials and their classification. In EMR/ESR/EPR spectroscopy for characterization of nanomaterials* (pp. 3-45). New Delhi: Springer India.

[18] T. A.Saleh, 2020. Nanomaterials: Classification, properties, and environmental toxicities. *Environmental Technology & Innovation*, 20(15), 101067.

[19] U. Schubert and N. Hüsing, 2005. *Synthesis of Inorganic Materials*, 2nd edn., *Wiley-VCH*.

[20] N. Baig, I. Kammakakam, and W. Falath, 2021. Nanomaterials: A review of synthesis methods, properties, recent progress, and challenges. *Materials advances*, 2(5), 1821-1871

[21] P. S.Kumar, K. G. Pavithra and M. Naushad,2019. *Characterization techniques for nanomaterials. In Nanomaterials for solar cell applications* (pp. 97-124). Elsevier.

[22] P. C. Lin, S. Lin, P. C. Wangand R. Sridhar, 2014. Techniques forphysicochemical characterization of nanomaterials. *Biotechnology advances*, 32(4), 711-726.

[23] V. P. Sharma,U. Sharma, M.Chattopadhyay and V. N.Shukla, (2018). Advance applications of nanomaterials: a review. *Materials Today: Proceedings*, 5(2), 6376-6380.

[24] M.A. Green, 2003. *Third Generation Photovoltaics, Advanced Solar Energy Conversion*,Springer, Berlin/New York.

[25] A.W. Miziolek, S.P. Karna, J.M. Mauro and R.A. Vaia, 2005. *Defense Applications of Nanomaterials.*ACS Symposium Series 891.

[26] L. R. Khot, S. Sankaran, J. M. Maja, R. Ehsaniand E. W. Schuster, 2012. Applications of nanomaterials in agricultural production and crop protection: a review. *Crop protection*, 35(6), 64-70.

[27] C. N. R. Rao, and A. K. Cheetham, 2001. Science and technology of nanomaterials: current status and future prospects. *Journal of Materials Chemistry*, 11(12), 2887-2894.

# THE ROLE OF ATOMIC STRUCTURE AND IMPERFECTION IN FORMATION OF METALS

**Manoj Kumar and Vineet Singh**

Department of Mechanical Engineering, IFTM University, Moradabad, India

Corresponding author E-mail: manoj_kumar@iftmuniversity.ac.in,

vineet.singh@iftmuniversity.ac.in

**Abstract:**

The atomic structure plays a crucial role in the physical, chemical, thermal and electrical properties of the material. Even, the material cost and use depend on its crystal structure, atomic packing factor, and stacking fault. This chapter includes the arrangement of atoms in a unit cell, the role of unit cell in a crystal, sharing of atoms, atomic radius, atomic packing factor, imperfections in the crystal structure, and properties of metals. Additionally, it provides the overall knowledge about crystal structure andformation of metals.

**Keywords:** Crustal Structure, Atomic Packing Factor, Unit Cell, Imperfections.

## 1. Introduction:

Since the development of civilization, men are using different vital materials for day-to-daylife. Initially, humans were dependent on the materials available in natural form. This age of civilization was called as Stone Age[1]. With the development of science and technology, a wide variety of materials have been developed and the civilization moved towards Bronze Age and Iron Age. Based on the materials we are using today, the civilization is called as Tailor Made Materials Age. In the modern era the materials can be defined as, substances whose constituent atoms or molecules are arranged in a systematic pattern. Till date, the materials available are said to be made from 118 types of elements (atoms) and their arrangement to form a particular structure. As per the available scientific literature the human body has been made from 25-27 types of elements in which oxygen atom alone is present 65% by weight. It is very much important to note that 90% mass of human body is made from oxygen, carbon, nitrogen, hydrogen, calcium and phosphorus. So it is the era in which the scientists and engineers are able to create or develop the materials by playing with Nano size particles.

There are three basic state of materials at atmospheric conditions i.e., solid, liquid and gas. The state of a material can be changed by changing their surrounding atmospheric conditions. Materials in solid state may be termed as metals and nonmetals. On the basis of crystalline structure, the metals (solid materials) may be crystalline or non-crystalline (amorphous). In case of solid materials, there may be solids having single crystal structure or an aggregate of all crystals to form polycrystalline structure. In every crystal, atoms are arranged in similar pattern. The boundary where this pattern changed is called crystal boundary and the metal is non as polycrystalline metal. So, the metals can be crystalline or polycrystalline [2]. Atoms are the main constituents to form a material. A metal may be made from single atom or it may have more than one atom. Metals with more than one atom are called alloys (such as steel).

## 2. Arrangement of Atoms:

The metals such as steel, aluminum, copper etc., which are being used in our daily life, are extracted from their raw materials available in the crust of our Earth. Initially, these metals are in liquid state at the time of extracting process. During extraction process, the metal in liquid state has to be cooled following some cooling rate [3]. This process of transformation from liquid to solid phase is called solidification. The type of atom and its atomic structure plays a very significant role in the development of any crystal structure of metals. In the process of solidification, the atoms of liquid metal reach to static position (equilibrium) to from solid and they get freeze at lattice point [4]. As per the bonding theory such as metallic bond in metals; the atoms freeze at some distance from each other in space lattice and this way a unit cell is formed. On the base of parameters of this unit cell, the lattice structure can be anyone of the proposed Bravais lattices; such as cubic in case of copper, iron and aluminum.

## 3. Role of Unit Cell:

A unit cell is the building block of any crystal in a metal (crystalline or polycrystalline) [5]. When the atoms of a liquid start to get arranged in a unit cell; the transformation starts to form solid. Now, if unit cell is considered to be cubic as in case of gold (Au), it will be having its dimensions in all three coordinates (X, Y and Z) and these dimensions have to be at some angles ($\alpha$, $\beta$ and $\gamma$)[3]. These dimensions and angles are called parameters of a unit cell. As per Bravais, there are fourteen (14) possible space lattices and maximum materials existing in our surrounding are based on them.

The atoms are regarded as rigid sphere and are identical in size for a particular metal. In case of metals the most common types of unit cell are given below [6].

i) Body centered cubic (BCC) unit cell (Mo, Va, Mn, Nb, Cr, $\alpha$-Fe etc.)
ii) Face centered cubic (FCC) unit cell (Al, Cu, Au, Ag, Pb, $\gamma$ -Fe, etc.)
iii) Hexagonal closed packed (HCP) unit cell (Be, Ca, Mg, Zn, Cd, Ti, etc.) [7]

In the development of unit cell the atoms are supposed to be at the lattice points. These lattice points in a unit cell are shown for FCC structure in Figure 1.

In the development of unit cell the atoms are supposed to be at the lattice points. These lattice points in a unit cell are shown for FCC structure in figure 1.

Figure-1The FCC unit cell is shown in the diagram in Cartesian coordinates.The side of the cube is shown by “p” equal for all sides [8]. In the figure letters a, b, c, d, e, f, g and h are the lattice points, where the atoms are supposed to occupy these sites.There are six sites, at the diagonal of faces and atoms will occupy these sites also. Total Number of atoms: 04, APF: 0.74 [9].

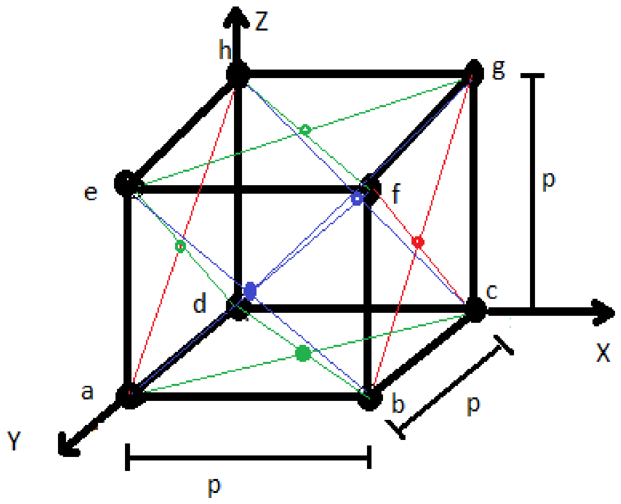

**Fig. 1: Structure of unit cell**

## 4. Arrangement of Atoms in Unit Cell:

In a unit cell at room temperature the arrangement of atoms can be in such way as shown in Figure-2 & Figure-3

i) In case of every cubic unit cell there is one atom at each corner of it.

ii) In case of BCC unit cell, one atom at the center of it.

iii) In case of FCC unit cell, one atom at the center of every face of it [10].

iv) In case of HCP unit cell, one atom at each corner and one atom at the center of upper and bottom face three atoms at the center plane; parallel to the bottom and upper face [11].

## 5. Sharing of Atoms in Unit Cell:

Sharing of atoms of in a unit cell is explained below in different possible ways. So, the number of atoms in unit cell can be calculated by following it.

i) In every cubic unit cell, the atom at every corner shares with eight adjoining unit cells [12].

ii) In case of BCC unit cell, the atom at center of the body shares all atoms at corner

iii) In case of FCC unit cell, the atom at the face shares half of it and half to the adjoining unit cell

iv) In case of HCP unit cell; each corner atom shares six adjoining unit cell. The atom at the top face and bottom faces, shares half to adjoining unit cell. There are three atoms in the center plane of a unit cell [13].

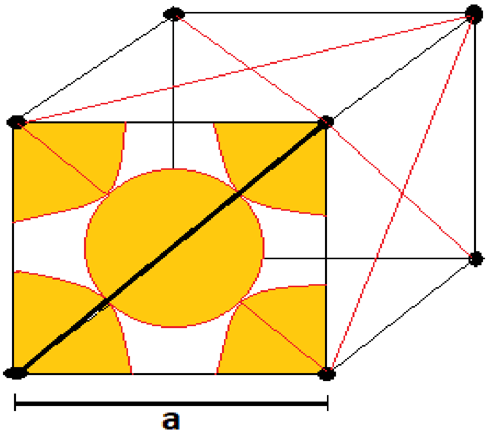

**Fig. 2: A FCC unit cell, showing atomic arrangement on one face and touching corner atoms. At other faces the atoms will be arranged in same way.**

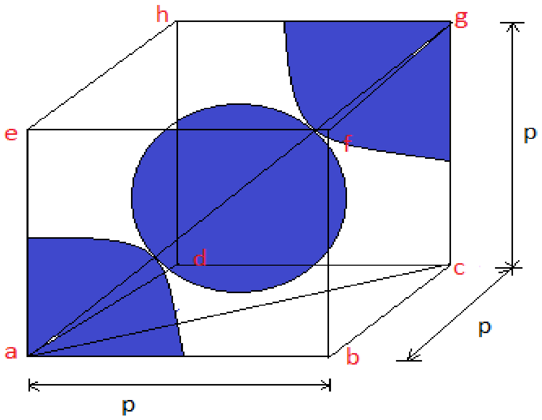

**Fig. 3: A BCC Unit Cell, showing how the atom at body centre, touching the corner atom and other corner atoms will also touch this, which are not shown.**

### 6. Number of Atoms in a Unit Cell:

Based on above rules the number of atoms in a unit cell can be found out as below;

In case of BCC = (1/8) x 8 (corners) + 1 (at the center of body) = 2

In case of FCC = (1/8) x 8 (corners) + (1/2) x 6 (at the center of face) = 4

In case of HCP = 2{(1/6) x 6 (corners)} + (1/2) x 2 (at the center of upper and bottom face) + 3 (at the center of cell) = 6[14].

### 7. Atomic Radius:

Apart from the sharing of atoms, some specific rules are there for atoms in different unit cell. In body centered cubic (BCC) unit cell the atom at the center; touches the atoms at the corner of it. In another case the atom at the center of a face centered cubic (FCC) unit cell touches the four atoms at the corner of the same face [15].

So based on the above rule; considering atom as sphere the atomic radius of it can be find out. (Figure-2 and figure- 3).

### 8. Atomic Packing Factor:

The atomic packing factor of a unit cell is the ratio of volume occupied by the atoms in a unit cell. It can be found out with the help of the relation between atomic radius and the dimension of the unit cell; and the number of atoms in a unit cell. In case of BCC, FCC and HCP unit cell it is 0.67, 0.74 and 0.74 respectively.

This way, development and the role of a unit cell can be understood very well. The internal atomic structure can be studied by X-ray diffraction method [16].

## 9. Crystal Structure and Imperfections:

A crystal is one in which all the atoms are arranged in a particular geometry, following the repetition of the unit cells. Sometimes a crystal is also known as grain. In actual practice; at the start of the atomic arrangement, number of unit cells start to form at various locations in different orientations. These unit cells are known as the nuclei and they grow with adjoining number of unit cells simultaneously at different locations in the molten material. This process of unit cells growing is called nucleation and growth.

With this phenomenon of the nucleation growth, these crystals meet with the nearby crystals and a boundary among them is formed, which is called crystal boundary (Figure-4). As the crystals are also known by grains; so crystal boundary are also known as grain boundary. In polycrystalline metal there are number of crystals which are separated from each other. These crystal structures and their boundaries can be seen by electron diffraction method and X-rays [17].

The properties of the materials are directly dependent on its structure. Scientists and Engineers are continuously in search of new materials; or creating new structures which are possible only on the basis of knowledge of earlier available structures [18]. This way the new materials are developing since the Stone Age to Tailor Made Materials Age [19].

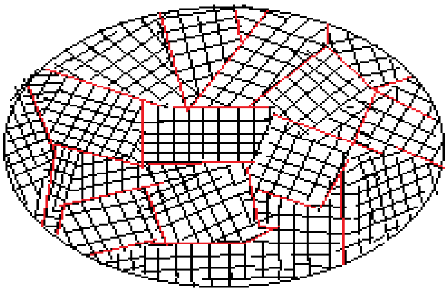

**Fig. 4: A polycrystalline structure: Showing grain boundaries**

The main objective of materials scientist is to investigate the relationships between the structure and the properties of a material.

### *9.1. Imperfection in Crystal Structure*

In actual practice it is very difficult task to achieve the perfect structure of a material. There is always some defect or disorder in the structure of a metal. The defects or imperfections may be developed during solidification process. The disorder in the crystal structure may be with zero, one, two or three dimensions [20]. Generally; the imperfections (defects) are classified in following ways;

i) Point Imperfection (Zero dimensional defect)
ii) Line imperfection or Dislocations (One dimensional defect)
iii) Surface or Grain Boundary Imperfection (Two dimensional defect)
iv) Volume Imperfection (Three dimensional defect)

In the interest of the development of metals, it is always made sure that there should not be any kind of imperfection in the crystal structure. Some time there is a need to create the impurities in an existing structure of a material; but actually, it is not in sense of the defect rather it is the requirement of the designed material with some specific properties. Steel is an alloy of iron; in which the element carbon is added to increase the hardness and strength of it. There are number of alloys which are developed to achieve some specific properties for engineering purposes.

## 10. Properties of Metals:

Materials are required to be tested with proposed standards to know their structure and the properties before use. The selection of material is very important task for an engineer, which is done based on the knowledge of the properties of materials. There are some important properties of engineering materials; such as physical, chemical, mechanical, electrical, thermal, magnetic and optical properties.

This way it is very important to know about how the materials are developed and used based on their properties.

## 11. Conclusion:

This chapter concludes that the unit cell is the smallest unit of the structure. Although, the physical, chemical, and electrical properties depend on the structure of the atoms inside the molecules. Additionally, three types of crystal structures are represented by the molecules that are BCC, FCC, and HCP. Moreover, imperfection is a defect that may be at the level of point, line, surface, and volume. The number of metal particles are added inside the material to strengthen the material like adding the carbon to enhance the hardness of the steel.

## References:

[1] H. Tsuzuki, P. S. Branicio, and J. P. Rino, “Structural characterization of deformed crystals by analysis of common atomic neighborhood,” *Comput. Phys. Commun.*, vol. 177, no. 6, pp. 518–523, 2007, doi: 10.1016/j.cpc.2007.05.018.

[2] R. Heimann, “Materials science of crystalline bioceramics: a review of basic properties and applications,” *Chiang Mai Univ. J.*, vol. 1, pp. 23–46, 2002.

[3] S. B. Sinnott and E. C. Dickey, “Ceramic/metal interface structures and their relationship to atomic- and meso-scale properties,” *Mater. Sci. Eng. R Reports*, vol. 43, no. 1–2, pp. 1–59, 2003, doi: 10.1016/j.mser.2003.09.001.

[4] “Materials Interfaces: Atomic-Level Structure and Properties,” no. JANUARY 1995, p. 2019, 2019.

[5] M. S. Hybertsen and L. Venkataraman, “Structure-Property Relationships in Atomic-Scale Junctions: Histograms and beyond,” *Acc. Chem. Res.*, vol. 49, no. 3, pp. 452–460, 2016, doi: 10.1021/acs.accounts.6b00004.

[6] D. C. Ghosh, R. Biswas, T. Chakraborty, N. Islam, and S. K. Rajak, "The wave mechanical evaluation of the absolute radii of atoms," *J. Mol. Struct. THEOCHEM*, vol. 865, no. 1–3, pp. 60–67, 2008, doi: 10.1016/j.theochem.2008.06.020.

[7] H. Lu, Y. Liu, B. Bin Xu, D. Hui, and Y. Q. Fu, "Spontaneous biaxial pattern generation and autonomous wetting switching on the surface of gold/shape memory polystyrene bilayer," *Compos. Part B Eng.*, vol. 122, pp. 9–15, 2017, doi: 10.1016/j.compositesb.2017.04.004.

[8] J. Pontius, J. Richelle, and S. J. Wodak, "Deviations from standard atomic volumes as a quality measure for protein crystal structures," *J. Mol. Biol.*, vol. 264, no. 1, pp. 121–136, 1996, doi: 10.1006/jmbi.1996.0628.

[9] D. B. Miracle and O. N. Senkov, "A geometric model for atomic configurations in amorphous Al alloys," *J. Non. Cryst. Solids*, vol. 319, no. 1–2, pp. 174–191, 2003, doi: 10.1016/S0022-3093(02)01917-8.

[10] A. Toriyabe *et al.*, "Mechanical property enhancement of the Ag–tailored Au–Cu–Al shape memory alloy via the ductile phase toughening," *Intermetallics*, vol. 139, no. February, 2021, doi: 10.1016/j.intermet.2021.107349.

[11] Q. rong Feng, J. dong Guo, X. lin Xu, H. Zhang, X. Zhu, and S. qi Feng, "The effect of ionic radius of metal element (M) on (Pb,M)-1212 superconductors (M= Sr, Ca, Mg, Hg, Cd, Cu)," *Solid State Commun.*, vol. 94, no. 1, pp. 21–25, 1995, doi: 10.1016/0038-1098(95)00019-4.

[12] Y. Zare and K. Y. Rhee, "A multistep methodology for effective conductivity of carbon nanotubes reinforced nanocomposites," *J. Alloys Compd.*, vol. 793, pp. 1–8, 2019, doi: 10.1016/j.jallcom.2019.04.070.

[13] S. Petrov, V. Marinova, C. C. Sun, K. Y. Hsu, and S. H. Lin, "Inch-scale graphene-based LC tunable phase retarders: Experimental study of surface interaction between liquid crystal-polyimide-graphene layers," *Appl. Surf. Sci.*, vol. 566, no. March, 2021, doi: 10.1016/j.apsusc.2021.150646.

[14] Y. Q. Cheng and E. Ma, "Atomic-level structure and structure-property relationship in metallic glasses," *Prog. Mater. Sci.*, vol. 56, no. 4, pp. 379–473, 2011, doi: 10.1016/j.pmatsci.2010.12.002.

[15] R. D. A. Pinto, L. D. R. Ferreira, and R. A. G. Silva, "Size matters: Influence of atomic radius from the ternary addition on the properties of Cu79Al19X2 (X = Be, Mn, Ag) alloys," *Mater. Chem. Phys.*, vol. 294, no. November 2022, 2023, doi: 10.1016/j.matchemphys.2022.127021.

[16] K. Wang *et al.*, "Evolution of microstructure and texture of moderately warm-rolled pure tungsten during annealing at 1300 °C," *J. Nucl. Mater.*, vol. 540, 2020, doi:

10.1016/j.jnucmat.2020.152412.

[17] A. Mannheim, J. A. W. van Dommelen, and M. G. D. Geers, “Long-term microstructural evolution of tungsten under heat and neutron loads,” *Comput. Mater. Sci.*, vol. 170, no. July, 2019, doi: 10.1016/j.commatsci.2019.109146.

[18] Z. S. Fan, D. P. Xiang, Y. L. Pan, and H. Jiang, “Effect of two-time spark plasma sintering on microstructure and mechanical properties of W–6Ni–4Mn alloy,” *Mater. Sci. Eng. A*, vol. 745, no. December 2018, pp. 300–306, 2019, doi: 10.1016/j.msea.2018.12.109.

[19] J. L. do Vale, C. H. da Silva, and G. Pintaude, “Tribological performance assessment of lamellar and compacted graphite irons in lubricated ring-on-cylinder test,” *Wear*, vol. 426–427, no. August 2018, pp. 471–480, 2019, doi: 10.1016/j.wear.2019.02.020.

[20] E. Ageev, R. Latipov, and E. Ageeva, “X-ray diffraction analysis of powders, obtained by electroerosive dispersion of a W-Ni-Fe alloy,” *Mater. Today Proc.*, vol. 38, pp. 1463–1466, 2021, doi: 10.1016/j.matpr.2020.08.127.

# CLUSTER RADIOACTIVITY: A TWENTY-YEAR PERSPECTIVE

**Ajeet Singh*[1], Manish Kumar[1], Priya Paneru[1], Jitendra Pal Singh[1], Atanu Nag[1], Narender Singh[1], Bal Krishna Yadav[1], Richa Saxena[2] and Vidhi Goyal[1]**
[1]Department of Physics, IFTM University Moradabad, UP India-244102
[2]Department of Physics, Shri Guru Ram Rai University, Dehradun, UK, India
*Corresponding author E-mail: ajeet5132singh@gmail.com

## Abstract:

This chapter reviews the current state of research on cluster radioactivity, focusing on the recent experimental and theoretical findings. Different theoretical methods were briefly explained and compared with the latest experimental results for various clusters. This chapter also highlights the different regions in which cluster radioactivity occurs. This provides a short summary of earlier studies of cluster radioactivity in the trans-lead and trans-tin regions. Additionally, an overview of semi-empirical formulas, latest developments in cluster radioactivity, and research on super-heavy nuclei are presented.

**Keywords:** Cluster Radioactivity, Nuclear Structure, Alpha Decay, And Half-Life.

## 1. Introduction:

The study of radioactive decay has greatly helped scientists to understand the structure of atomicnuclei. Henri Becquerel made the discovery of radioactivity in 1896, and the Curie pair verified it in 1898. Radioactivity, also known as nuclear decay, is a process by which an unstable atomic nucleus loses energy by producing radiation. By examining radioactivity around the start of the 20th century, scientists were able to make their first observations of the atomic nucleus. Alpha, beta, and gamma are the three primary forms of radioactive decay that were discovered by early studies. In 1940, a different kind of decay was identified, where heavy atomic nuclei split into two approximately equal pieces [1]. We call this process spontaneous fission.

In 1980, Poenaru, Sandulescu, and Greiner [2, 3] introduced a new type of radioactive decay called cluster radioactivity. This form of decay involves the nucleus releasing a fragment that is larger than an alpha particle but smaller than the smallest fission fragment. During this process, a parent nucleus (A, Z) splits into two parts: a daughter nucleus ($A_1$, $Z_1$) and the emitted cluster ($A_2$, $Z_2$), following the relations $A = A_1 + A_2$ and $Z = Z_1 + Z_2$. The term "cluster radioactivity" was created in similar to other types of radioactive decay. When a nucleus releases a proton, this is called proton radioactivity. When an alpha particle is emitted, it is called alpha radioactivity. Similarly, when a nucleus releases a small group of particles (a cluster), it is called the cluster radioactivity.

Cluster decay is different from nuclear fission because, in cluster decay, a small cluster of particles is thought to already exist inside the nucleus before it escapes by overcoming the nuclear force barrier. In contrast, during fission, the nucleus gradually changes shape until it reaches a critical point (called the saddle point), where the sizes and charges of the two resulting fragment is determined. From there, the fragments separate due to the repelling force between their charges. Experiments that measure both cluster decay and spontaneous fission at the same time show that spontaneous fission happens more quickly than cluster decay. This indicates that there is no relationship between the two processes. A further significant difference is that only the lighter particles emitted during cluster decay are quantified, whereas both lighter and heavier pieces are detected during fission. We can characterize a radioactive nucleus as one that decays by releasing a variety of particles, such as clusters heavier than alpha particles, alpha particles themselves, beta particles, gamma rays (when the nucleus is in an excited state), or any combination of these, since cluster decay competes with alpha decay but differs completely from fission. This idea was suggested by Gupta [4] and is illustrated in Figure 1.

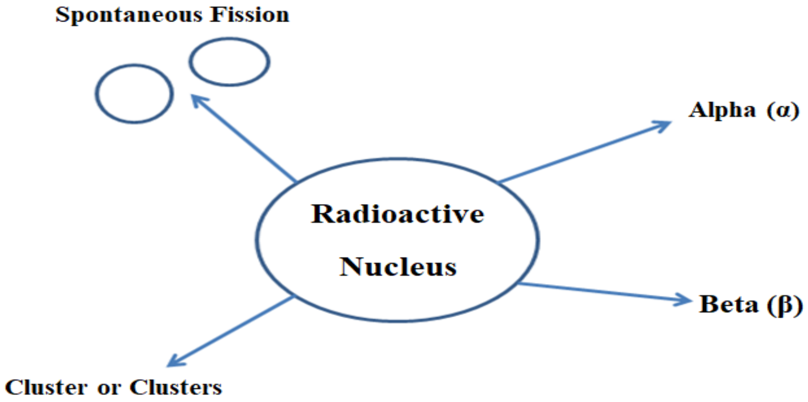

**Fig. 1: Diagram illustrating various possible modes of spontaneous radioactive decay in the nucleus.**

## 2. A Short Summary of the Experimental Study on Cluster Radioactivity:

Cluster decay was first observed experimentally in 1984 by Rose and Jones [5] at Oxford University, who detected the spontaneous emission of $^{14}$C from the decay of $^{223}$Ra using a solid-state counter telescope. The probability of $^{14}$C emission relative to alpha decay in $^{223}$Ra is $(8.5\pm2.5)\times10^{-10}$, meaning that for every alpha particle emitted, approximately $(8.5\pm2.5)\times10^{-10}$ carbon nuclei are also released. However, the reduced width (or preformation probability) of $^{14}$C is lower by a factor of ~$10^5$ to $10^6$, indicating that carbon emissions are significantly less likely than alpha decay. Aleksandrov *et al.* [6] confirmed the spontaneous emission of $^{14}$C decay from $^{223}$Ra parent isotopes. In this process, the branching ratio for $^{14}$C decay relative to alpha decay was determined to be $(7.6 \pm 3.0) \times 10^{-10}$. The researchers employed a ΔE-E detection system to analyze the emitted $^{14}$C particles emitted from the source. Subsequently, this discovery was independently verified by S. Gales *et al.* [7] and Price *et al.* [8].

Experimental observations have confirmed the decay of nuclear clusters such as $^{14}$C, $^{20}$O, $^{24}$Ne, $^{28}$Mg, and $^{32}$Si [9,10], which predominantly transform into daughter nuclei in the trans-lead region, specifically into doubly magic $^{208}$Pb or its neighboring nuclei. Additionally, theoretical predictions suggest the existence of another region of cluster radioactivity (CR) in the trans-tin region, where emitted clusters decay into daughter nuclei near doubly magic $^{100}$Sn [11].

Notably, heavier cluster emissions, such as $^{24}$Ne from $^{231}$Pa, $^{233}$U, and $^{230}$Th, were first detected by Sandulescu and colleagues [12] in Dubna. Bonetti *et al.* [13] experimentally studied the spontaneous emission of neon clusters ($^{22}$Ne and $^{24}$Ne) from $^{230}$U using glass track detectors. Several research groups worldwide have reported observations of specific cluster decays, including $^{14}$C emission from $^{221}$Fr, $^{221-224,226}$Ra, and $^{225}$Ac; $^{20}$O emission from $^{228}$Th; $^{23}$F emission from $^{231}$Pa; $^{24}$Ne emission from $^{230,232}$Th, $^{231}$Pa, and $^{232-236}$U; $^{28}$Mg emission from $^{232-236}$U, $^{237}$Np, and $^{236,238}$Pu; $^{30}$Mg emission from $^{238}$Pu; $^{32}$Si emission from $^{238}$Pu; and $^{34}$Si emission from $^{238,240}$Pu, $^{241}$Am, and $^{242}$Cm [14, 15].

## 3. A brief summary of earlier theoretical research on cluster radioactivity in various regions:

Poenaru *et al.* [16] proposed that all stable nuclei with atomic numbers (Z) $>$ 40, lighter than lead, are in a metastable state when it comes to spontaneous cluster decay, based on an analytical super-asymmetric fission model. They reported half-lives ranging from $10^{40}$ to $10^{50}$s for nuclei with Z > 62. The authors concluded that parent nuclei with Z > 60 were likely to undergo cluster decay, emitting clusters such as $^{12}$C, $^{16}$O, $^{30}$Si, $^{32}$Si, $^{48}$Ca, $^{50}$Ca, and $^{68}$Ni. These decays, with half-lives $T_{1/2} > 10^{40}$s, would result in the formation of daughter nuclei with atomic numbers Z = 50-58 and neutron numbers N = 78-82.

Poenaru, Greiner, and Gherghescu [17] used the ASAFM model to predict a new region of proton-rich parent nuclei undergoing spontaneous cluster emission. They calculated the half-lives and branching ratios for the emissions of $^{12}$C, $^{16}$O, $^{28}$Si, and several other clusters decayed from nuclei with proton numbers ranging from Z=56 to 64 and neutron numbers between N=58-72. Their findings led them to conclude that cluster decay from these proton-rich parent isotopes results in the formation of a doubly magic daughter nucleus, $^{100}$Sn.

Gupta *et al.* [18] investigated possible exotic cluster decay modes of certain stable nuclei within the atomic number range of 50 to 82 using the preformed cluster model (PCM). Their study revealed that some deformed nuclei, located near the spherical magic numbers at Z = 50 and 82 and the deformed stable shell at N = 108, exhibit significant instability against various heavy cluster decay modes. The authors provided predicted half-life estimates for specific decay processes, including the decay of $^{120}_{56}Ba$ via $^{12}$C and $^{16}$O, and the decay of $^{186}_{80}Hg$ via $^{8}$Be, with half-lives of approximately ~$10^{22}$, $10^{26}$, and $10^{28}$ s respectively.

In 1994, Satish *et al.* [19] studied cluster emissions from $^{112-120}$Ba nuclei using a PCM model. Their findings indicated that the emission of $^{4}$He and $^{12}$C from $^{112}$Ba was the most probable decay mode, with a half-life of approximately $10^{4}$ s. They identified the shortest half-life for $^{112}$Ba decay via $^{12}$C emission, emphasizing the importance of the doubly magic $^{100}$Sn daughter nucleus in the trans-tin region.

In 1996, Satish *et al.* [20] used the PCM model to study cluster decays from neutron-rich nuclei such as $^{146}$Ba, $^{152}$Ce, $^{156}$Nd, $^{160}$Sm, and $^{164}$Gd. These nuclei appeared to be resistant to $^{4}$He and $^{10}$Be decay based on their examination of the shell effects on the binding energies and relative preformation probability. Furthermore, they discovered that decays that resulted in the daughter being a doubly magic $^{132}$Sn nucleus had the shortest half-lives for non-alpha-like metastable decays with $Q > 0$.

A study on the half-lives of $^{12}$C decay from Ba isotopes was carried out in 1999 by Santhosh *et al.* [21] who used the Coulomb and proximity potential model (CPPM) to define the potential energy barrier. In contrast to the experimentally determined value of $5.620 \times 10^{3}$ s, their calculations produced a half-life of $6.020 \times 10^{3}$ s for the $^{12}$C decay of $^{112}$Ba. The most probable decay mode, according to the study, was $^{12}$C emission from $^{112}$Ba.

The logarithmic half-lives for the decay of $^{4}$He, $^{8}$Be, $^{12}$C, $^{20}$Ne, $^{24}$Mg, and $^{32}$S from different isotopes of the Nd parent were predicted by Santhosh *et al.* [22] using the CPPM model. The $^{16}$O and $^{20}$Ne emissions from $^{120}$Nd had the shortest half-lives, at $10^{10}$ s, according to their findings. The authors emphasized the significance of the doubly magic $^{100}$Sn daughter nucleus in the trans-tin region in light of these findings. They also contrasted their estimated half-life values for various cluster decay modes with those published by Satish *et al.* using the PCM model, Poenaru *et al.* using the ASAFM model, and Shanmugam *et al.* using the CYEM model.

In 2009, Sushil Kumar [23] conducted a study on the decay of $^{118-132,140-170}$Ce nuclei, focusing on the closed-shell configuration of the daughter nucleus Sn. The study revealed that the half-lives of the cluster decay were at their lowest when the neutron number of the daughter nucleus ($N_d$) was 50 or 82, corresponding to a closed-shell configuration. For the Oxygen cluster decay from $^{118-132,140-170}$Ce isotopes, the shortest decay half-lives were observed at the magic numbers $N_d$=50 and 82. The findings indicate that the minimal half-lives for cluster decay modes leading to $^{100}$Sn and $^{132}$Sn demonstrate the high stability of these nuclei against such decay processes.

Santhosh *et al. [*24] investigated the influence of neutron magicity on the cluster radioactivity. Using the CPPM model, they analyzed the cluster decay half-lives of $^{15}$N from $^{206-230}$Ac, $^{23}$F from $^{212-238}$Pa, $^{25}$Ne from $^{217-240}$U, and $^{29}$Mg from $^{217-239}$U. Their findings were compared with the results from UNIV, UDL, and Horoi's Scaling Law. This study highlighted the importance of the doubly magic daughter nucleus $^{208}$Pb in cluster radioactivity. Moreover, it was observed that neutron shell closure played a more significant role than proton shell closure in this process.

In 2013, Santhosh *et al.* [25] analyzed the stability of isotopes $^{248-254}$Cf against alpha and cluster decay using the CPPM model. Their study revealed that these nuclei remain stable against the emission of light clusters but are unstable when it comes to the emission of heavier clusters ($A_2 \geq 40$). They observed that heavy cluster emissions from these isotopes typically lead to the formation of a doubly magic $^{208}$Pb nucleus or a closely related nucleus. The authors concluded that in most cases of cluster decay, the inclusion of quadrupole deformation ($\beta_2$) reduces both the width and height of the barrier, leading to shorter half-lives. However, they found that hexadecapole deformation had no effect on the half-life.

The decay of $^{4}$He, $^{12}$C, $^{16}$O, $^{20}$Ne, and $^{24}$Mg from proton-rich platinum isotopes was investigated by Deepthy *et al.* [26] using the efficient liquid drop model. The most likely of these decay modes, according to their results, is $^{4}$He emission from $^{166}$Pt. Additionally, they determined that because $^{12}$C decay has the shortest logarithmic half-life among platinum isotopes, it is the most likely mode. A shell closure effect was also predicted by the study for the decays of $^{16}$O, $^{20}$Ne, and $^{24}$Mg at neutron number N=82, also referred to as a magic number.

Yonghao *et al.* [27] investigated the possibility of cluster radioactivity (CR) in trans-tin region neutron-deficient nuclei in 2020. Several analytical formulas, the GLDM, and the ELDM served as the foundation for their analysis. The half-lives of these decays are affected by the existence of a Q-value shell effect (shell closure) at $N_d = 50$ ($^{100}$Sn), according to this study. Additionally, daughter nuclei with $N_d = 50$ had the shortest cluster decay half-lives, according to the investigators. The half-lives of α-like cluster decays that produce isotopes with $N_d = 50$ are also simpler to quantify than those of non-α-like decays, they reported.

In 2022, Joshua *et al.* [28] studied the cluster decay half-lives of even-even isotopes of barium ($^{112-122}$Ba) in both their ground and intrinsic excited states along the proton drip line. They calculated the decay half-lives using the preformed-cluster decay model (PCM) and determined the penetration probability from the interaction potential using the Wentzel-Kramers-Brillouin (WKB) approximation. Their results showed that the shortest half-lives for the cluster decay of $^{12}$C from $^{112-122}$Ba isotopes occurred when the decay led to the formation of the daughter nucleus $^{100}$Sn.Additionally, they observed that while excitation plays a role, it does not overshadow or negate the effect of nuclear magicity. The study concluded that the calculated decay half-lives using both the relativistic R3Y NN potential and the M3Y potential are in reasonably good agreement with the experimental lower limit observed for $^{114}$Ba.

## 4. Empirical formulas can be used to determine the half-lives of cluster decay:

Numerous empirical formulas, such as the Royer formula [29], KPS formula [30], UNIV formula [31], Ni-Ren-Dong-Xu (NRDX) formula [32], BKAG formula [33],VSS formula [34], UDL formula [35], Horoi formula [36,37,38] Viola-Seaborg-Sobiczewski (VS) formula [39], and TM formula [40], are commonly used to estimate and predict alpha and cluster decay half-lives. In this chapter, we explore the calculation of half-lives using the empirical UDL formula [35] proposed by C. Qi et al., the Viola-Seaborg (VS) formula, the scaling law introduced by Horoi et al., and the TM formula, which is discussed in detail below.

### *4.1 Viola-Seaborg formula (VS)*

Viola and Seaborg proposed the Viola-Seaborg semi-empirical formula, which includes various parameters, as expressed in the following form,

$\log_{10}T_{1/2}(\mathrm{VS}) = (aZ_P + b)Q_\alpha^{-1/2} + (cZ_P + d) + h_{\log},$

The atomic number of the parent nucleus is denoted as $Z_P$. The four parameters, a, b, c, and d are fitting constants with values 1.66175, -8.5166, -0.20228, and -33.9069, respectively. The hindrance factor ($h_{\log}$)is assigned as follows:

$h_{\log}$=0 when both Z (proton number) and N (neutron number) are even.$h_{\log}$=0.722 when Z is odd and N is even.$h_{\log}$=1.066 when Z is even and N is odd.$h_{\log}$=1.114 when both Z and N are odd.

### *4.2 Universal Decay Law (UDL)*

The Universal Decay Law (UDL) for alpha and cluster decay was introduced by C. Qi et al., based on the R-matrix theory [41]. This formula applies to the monopole radioactive decay of all the clusters. The model depends on the mass and charge numbers of the daughter nucleus and the emitted cluster, as well as the Q value. The UDL formula is expressed as follows.

$$\mathrm{Log}_{10}T_{1/2}(\mathrm{UDL}) = aZ_eZ_d\sqrt{\frac{\mu}{Q}} + b\sqrt{\mu ZeZd(A_e^{\frac{1}{3}} + A_d^{\frac{1}{3}})} + C$$

The reduced mass, denoted as μ given by $\mu = \frac{A_eA_d}{A_e+A_d}$where $A_d$and $A_e$represent the mass numbers of the daughter nucleus and the emitted cluster, respectively.

### *4.3 Scaling law of Horoi et al.*

We have determined the half-life of alpha and cluster decays using the empirical formula proposed by M. Horoi *et al.* [36,37,38]. This formula is expressed in terms of the reduced mass (μ), with the coefficients a, b, c, and d as predefined constants.

$\log_{10}T_{1/2}(\mathrm{Horoi}) = (a\mu^{0.146} + b)[(Z_eZ_d)^{(0.613)}/\sqrt{Q} - 7] + (c\mu^{0.416} + d);$

where $Z_e$ and $Z_d$ stand for the atomic numbers of the emission and daughter nuclei, and $T_{1/2}$ is the cluster decay half-life. a = 9.1, b = -10.2, c = 7.39, and d = -23.2 are the four sets of factors.

## 5. Conclusions:

This chapter discusses past theoretical and experimental studies on cluster radioactivity, especially in elements beyond the trans-tin and trans-lead regions.Scientists have developed various empirical formulas (models) to describe alpha and cluster emissions.Some of these include the Royer formula, BKAG formula, TM formula, VSS formula, UNIV formula, UDL formula, Viola-Seaborg-Sobiczewski (VS) formula, Horoi formula, KPS formula, and NRDX formula.The study of magic numbers in nuclei and their shell structures is important for understanding the cluster radioactivity. According to the nuclear shell model and other theoretical studies, nuclei with a specific number of protons and neutrons (magic numbers) are more stable. Research has mainly focused on doubly magic nuclei, as predicted by the nuclear shell model. Cluster decay often results in doubly magic daughter nuclei like $^{100}$Sn and $^{208}$Pb, which are experimentally easier to observe. This was confirmed experimentally.

## References:

[1] K.A. Petrzhak and G.N. Flerov,“Spontaneous fission of Uranium", Zh. Eksp. Teor.Fiz.10, pp. 1013-1017(1940).

[2] A. Sandulescu, D.N. Poenaru, and W. Greiner, “New type of decay of heavy nuclei intermediate between fission and alpha decay", Sov. J. Part. Nucl.11, pp. 528-541(1980).

[3] K.P. Santhosh and InduSukumaran, “Studies on cluster decay from trans-lead nuclei using different versions of nuclear potentials", Eur. Phys. J. A 53, 136 (2017).

[4] Raj K. Gupta, Sarbjit Singh, Rajeev K. Puri, and Werner Scheid, “Instabilities against exotic cluster decays in “stable" nuclei with Z and N in the neighborhood of spherical and deformed closed shells", Phys. Rev. C 47, pp. 561-566, (1993).

[5] H.J. Rose and G.A. Jones, “208Pb-daughter cluster radioactivity and the deformations and orientations of nuclei", Nature (London) 307, pp. 245-247 (1984).

[6] D.V. Aleksandrov, A.F. Belyatskii, Yu.A. Glukhov, Nikol'skii, B. G.Novatskii, A. A. Ogloblin, and D.N. Stepanov, “Observation of the spontaneous emission of $^{14}$C nuclei from $^{223}$Ra", JETP Lett.40, pp 909-912(1984).

[7] S. Gales, E. Hourani, M. Hussonnois, J.P. Schapira, L. Stab, and M. Vergnes, “Exotic Nuclear Decay of $^{223}$Ra by Emission of $^{14}$C Nuclei", Phys. Rev. Lett.53, pp. 759-762(1984).

[8] P.B. Price, J.D. Stevenson, S.W. Barwick, and H.L. Ravn, “Discovery of Radioactive Decay of $^{222}$Ra and $^{224}$Ra by $^{14}$C Emission", Phys. Rev. Lett.54, pp. 297-299(1985).

[9] D.N. Poenaru, in ed. D.N. Poenaru, Nuclear Decay Modes, Institute of Physics, Bristol, UK, 1996.

[10] P. Buford Price, “Heavy-Particle Radioactivity (A> 4)", Annu. Rev. Nucl. Part. Sci. 39, pp. 19-42(1989).

[11] W. Greiner, M. Ivascu, D.N. Poenaru, and S. Sandulescu, in Treatise on Heavy Ion Science, edited by D.A. Bromley (Plenum, New York, 1989), Vol. 8, p. 641.

[12] P.B. Price, K.J. Moody, E.K. Hulet, R. Bonetti, and C. Migliorino, "High-statistics study of cluster radioactivity from $^{233}$U", Phys. Rev. C 43, pp. 1781-1788(1991).

[13] R. Bonetti, C. Carbonini, A. Guglielmetti, M. Hussonnois, D. Trubert and C.LeNaour, "Cluster decay of $^{230}$U via Ne emission", Nucl.Phys.A 686, pp. 64-70(2001).

[14] R. Bonetti, C. Chiesa, A. Guglielmetti, C. Migliorino, A. Cesana, M. Terrani, and P.B. Price, "Neon radioactivity of uranium isotopes", Phys. Rev. C 44, pp. 888-890(1991).

[15] Shicheng Wang, D. Snowden-lift, P.B. Price, K.J. Moody, and E.K. Hulet, "Heavy fragment radioactivity of $^{238}$Pu: Si and Mg emission", Phys. Rev. C 39, 1647(R)(1989).

[16] D.N. Poenaru, W. Greiner, M. Ivascu, and A. Sandulescu "Heavy cluster decay oftrans-zirconium "stable" nuclides", Phys. Rev. C 32, pp. 2198-2200, (1985).

[17] D.N. Poenaru, W. Greiner, and R. Gherghescu, "New island of cluster emitters",Phys. Rev. C 47, pp. 2030-2037, (1993).

[18] Raj K. Gupta, Sarbjit Singh, Rajeev K. Puri, and Werner Scheid, "Instabilitiesagainst exotic cluster decays in \stable" nuclei with Z and N in the neighborhoodof spherical and deformed closed shells", Phys. Rev. C 47, pp. 561-566, (1993).

[19] Satish Kumar, and Raj K. Gupta, "Measurable decay modes of barium isotopesvia exotic cluster emissions", Phys. Rev. C 49, pp. 1922-1926, (1994).

[20] Satish Kumar, J.S. Batra and Raj K. Gupta, "Cluster emissions with $^{132}$Sn daughterfrom neutron-rich nuclei", J. Phys. G: Nucl. Part. Phys. 22, pp. 215-219, (1996).

[21] K.P. Santhosh, and Antony Joseph, "Exotic decay in Ba isotopes via $^{12}$C emission",Pramana J. Phys. 55, pp. 375-382, (2000).

[22] K.P. Santhosh, R.K. Biju, SabinaSahadevan, and Antony Joseph, "Exotic decayin proton-rich Nd isotopes", Phys. Scr. 77, 065201, (2008).

[23] Sushil kumar, "Shell closure effects associated with tin daughter", Proc. Int. Sym.Nucl. Phys. 54, pp. 204, (2009).

[24] K.P. Santhosha, M.S. Unnikrishnan and B. Priyanka, "Role of neutron magicity inthe cluster radioactivity", Proc. DAE Symp.Nucl.Phys. 57, pp. 342-343 (2012).

[25] K.P. Santhosh, and R.K. Biju, "Stability of $^{248-254}$Cf isotopes against alpha andcluster radioactivity", Annals of Physics 334, pp. 280-287 (2013).

[26] Deepthy Maria Joseph, Nithu Ashok, and Antony Joseph, "A theoretical study ofcluster radioactivity in platinum isotopes", Eur. Phys. J. A 54, 8 (2018).

[27] Yonghao Gao, Jianpo cui, Yanzhao Wang and JianzhongGu, "Cluster radioactivityof neutron-de_cient nuclei in trans-tin region", Sci. Rep. 10, 9119 (2020).

[28] Joshua T. Majekodunmi, M. Bhuyan, D. Jain, K. Anwar, N. Abdullah, and Raj Kumar, “Cluster decay half-lives of $^{112\text{-}122}$Ba isotopes from the ground state and intrinsic excited state using the relativistic mean-field formalism within the preformed-cluster-decay model", Phys. Rev. C 105, 044617, (2022).

[29] G. Royer, “Alpha emission and spontaneous fission through quasi-molecular shapes", J. Phys. G: Nucl. Part. Phys. 26, pp. 1149-1170 (2000).

[30] K.P. Santhosh, R.K. Biju, Sabina Sahadevan,“Semi-empirical formula for spontaneous fission half life time", Nucl. Phys.A 832, pp. 220-232 (2009).

[31] D.N. Poenaru, R. A. Gherghescu, and W. Greiner, “Single universal curve for clusterradioactivities and alpha decay", Phys. Rev. C 83, pp. 014601 (2011).

[32] Dongdong Ni, Zhongzhou Ren, Tiekuang Dong, and Chang Xu, “Unified formula of half-lives for alpha decay and cluster radioactivity", Phys. Rev. C 78, 044310 (2008).

[33] M. Balasubramaniam, S. Kumarasamy, N. Arunachalam, and Raj K. Gupta, “Newsemiempirical formula for exotic cluster decay", Phys. Rev. C 70, 017301 (2004).

[34] Zhongzhou Ren, Chang Xu, and Zaijun Wang, “New perspective on complex clusterradioactivity of heavy nuclei", Phys. Rev. C 70, 034304 (2004).

[35] C. Qi, F.R. Xu, R.J. Liotta, and R. Wyss, “Universal Decay Law in Charged-Particle Emission and Exotic Cluster Radioactivity", Phys. Rev. Lett.103, 072501(2009).

[36] Mihai Horoi, “Scaling behavior in cluster decay", J. Phys. G: Nucl. Part. Phys.30, pp. 945-55 (2004).

[37] Ajeet Singh, A. Shukla, and M.K. Gaidarov, “Cluster decay half-lives in trans-tinand transition metal region using RMF theory", J. Phys. G: Nucl. Part. Phys.49, 025101 (2021).

[38] Ajeet Singh, A. Shukla, and M.K. Gaidarov, “Structure and decay modes studyof Th, U, and Pu isotopes using Relativistic mean-field model", Nuclear Physics A,1023, 122439 (2022).

[39] A. Sobiczewski, Z. Patyk, and S. Cwiok, “Deformed super-heavy nuclei", Phys. Lett.B 224, pp. 1-4 (1989).

[40] O.A.P. Tavares, E.L. Medeiros, “A calculation method to estimate partial half-livesfor exotic radio-activities", Eur. Phys. J. A 49 (6), pp. 1-4(2013).

[41] A.M. Lane and R.G. Thomas, “R-Matrix Theory of Nuclear Reactions", Rev. Mod.Phys. 30, pp. 257-353(1958).

# GRAVITATIONAL WAVES IN MODIFIED GRAVITY MODELS

**Bal Krishna Yadav*[1], Atanu Nag[1], Narender Singh[1], Jitendra Pal Singh[1],**
**Ajeet Singh[1], Manish Kumar[1], Vidhi Goyal[1], Priya Paneru[1],**
**Vipin Kumar Sharma[2] and Murli Manohar Verma[2]**
[1]Department of Physics, School of Sciences, IFTM University, Moradabad-244102
[2]Department of Physics, University of Lucknow, Lucknow-226007
*Corresponding author E-mail: balkrishnalko@gmail.com

## Abstract:

In this research work, we studied the modified gravity models. In these models, we focused on f(R) gravity models in which we generalize the General Theory of Relativity. Other modified gravity models on which my research is focused, are Scalar-Tensor theories, Braneworld models etc. We studied the chameleon mechanism for some viable f(R) gravity models. We use the Gravitational Waves as a tool to constrain our models. The study of polarization modes of Gravitational Waves in modified gravity models is very important.

## 1. Introduction:

Einstein's General Theory of Relativity (GTR) predicts the existence of the Gravitational Waves (GWs). The observation of GWs is also a test of GTR. But the dark energy and dark matter problems in cosmology require the modification of GTR. We have many observational evidences of dark energy like Supernovae type Ia, Baryon Acoustic Oscillation (BAO), Cosmic Microwave Background anisotropies, weak gravitational lensing etc. [1-3]. Dark energy accelerates the expansion of the present universe. The approaches to modify the GTR are broadly classified in two classes (i) modified gravity models (ii) modified matter models. In modified gravity models [4-10], we modify the gravitational part of the Einstein-Hilbert action in different ways. There are many modified gravity models like f(R) theory, Scalar-Tensor theories, Braneworld models, Gauss-Bonnet dark energy models etc.[12-19,27]. In modified matter models an extra component of matter is added in the energy momentum tensor of GTR. Quintessence, k-essence and phantom dark energy models etc., are examples of modified matter models [20-24]. The standard model of cosmology also known as Lambda Cold Dark Matter ($\Lambda$CDM) model is a perfect model to explain the late time cosmic acceleration but it faces the problems with cosmological constant $\Lambda$.

The observation of flat rotation curves of galaxies [10,11] and gravitational lensing indicate the presence of new matter often known as dark matter. Rather strangely, this matter does not experience the electromagnetic interaction, even though it has the gravitational interaction with the normal matter and radiation. The fundamental nature of the dark matter is still mysterious. There are some famous candidates of dark matter like weakly interacting massive particles (WIMPs). At the same time, there exist several alternative approaches to explain the effects of dark matter in modified gravity theories. Dark matter and dark energy problems are explained by scalar field in several references [23, 25]. Some authors studied the oscillations of the scalar field [24, 26].

$f(R)$gravity is one of the simplest modified gravity model. In this model, we mainly study the dark energy problem of the Cosmology. Beside the dark energy problem, we study the inflation and dark matter problem in $f(R)$ models. Till now we do not have complete form of $f(R)$, which can explain the whole evolution of the universe. Different observations like Cosmic Microwave Background, Lensing, Large Scale Structure etc. are used to constrain the theoretical models of gravity and $f(R)$ gravity models also.

Since GWs can act as a tool in constraining the different gravity models, it is important to study the GWs in $f(R)$ gravity. Authors have used the data of observed GW170817 and GRB170817A to impose the conditions on the parameters of different modified gravity models along with $f(R)$ models [28, 29]. The polarization modes and speed of GWs in $f(R)$ models and other modified gravity models have been studied in some references [30-32]. It is found that these parameters of GWs in modified gravity are different from those in the General Relativity (GR). In General Theory of Relativity (GTR), we have two polarization modes + and × of gravitational waves. Speed of GWs is equal to that of the speed of light in GTR. In $f(R)$ gravity we have an extra scalar mode of polarization and a breathing mode of GWs.

The detection of recently observed gravitational waves by the Laser Interferometer Gravitational-Wave Observatory (LIGO) Scientific Collaboration and VIRGO Collaboration further supports Einstein's General Relativity (GR) and provides a new tool to study gravitational physics [33]. In order to confirm gravitational waves predicted by GR, it is necessary to determine the polarization of gravitational waves. This can be done by the network of ground-based detectors such as the LIGO (United States), VIRGO (France-Italy), GEO (Germany-United Kingdom), and KAGRA (Japan). They are geared to operate in the range of a few tens of Hz to kHz range. There are also plans for future ground-based detectors in Australia (AIGO) and in our country India (INDIGO). The Laser Interferometric Space Antenna (LISA) is also a proposed space mission to observe low-frequency GW in the range of 0.1 MHz to 0.1 Hz. In the recent GW170814, the Advanced VIRGO detector joined the two aLIGO detectors, so they were able to test the polarization content of gravitational waves for the first time. The polarization of a wave gives information about the geometrical orientation of oscillations. A common method to discuss polarization modes (PMs) of GWs in the linearized theory consists of metric perturbations around Minkowski background.

In GR, the gravitational wave propagates at the speed of light and it has two polarization states, the plus and cross modes.

Because of the advancement of GW probes, several scientists attempted to test the deviation in the Einstein-Hilbert gravity action integral by studying the properties of GWs. It is usually started by assuming Einstein's GR as a null hypothesis and then considering deformations away from GR. It is started from a particular modified gravity model, developing its equations and solutions, and it predicts certain observables that then might or might not agree with the experiment. With alternate theories of gravity, one has complete control over the theory under study and is able to write down the full equations of motion, answer questions about the well-posedness and stability of solutions, and predict observables in the context of planned future probes.

## 2. Lambda Cold Dark Matter ($\Lambda$CDM) Model:

To study the GWs in ΛCDM model and modified gravity theories, we take perturbation in the field equations of these theories. Here, we will give some basic equations, that will be used in our analysis.

The action for ΛCDM model is:

$$A = \frac{1}{16\pi G}\int d^4x(R - 2\Lambda) + A_m \ (1)$$

where $G$ is the universal gravitational constant, $A_m$ is the action of matter fields and $R$ is the Ricci scalar. The variation of the action (1) with respect to metric tensor $g_{\mu\nu}$ gives the field equations as:

$$R_{\mu\nu} - \frac{1}{2}g_{\mu\nu}R + \Lambda g_{\mu\nu} = 8\pi G T_{\mu\nu} \ (2)$$

where $R_{\mu\nu}$ is the Ricci tensor and $T_{\mu\nu}$ is the energy-momentum tensor of the matter.

On taking the perturbation in the space-time metric $g_{\mu\nu}$, we get the perturbation equations of the field equations (2). The tensor modes of GWs in $f(R)$ models are same as those in the General Theory of Relativity (GTR). Therefore, we would focus on the scalar modes of GWs in modified gravity theories. To make a comparative study of the gravitational waves in $\Lambda$CDM model and modified gravity, we would study perturbation in the field equations of these theories.

## 3. $f(R)$ gravity models:

$f(R)$gravity is one of the simplest modified gravity model. There are three formalisms to derive the field equations of $f(R)$ gravity, (i) metric formalism (ii) Palatini formalism and (iii) metric-affine formalism. As the number of polarization modes of GWs are different in metric and Palatini formalisms, from the observations of GWs, we would find out the suitable formalism in $f(R)$ gravity. The action of the $f(R)$ model is given as

$$A = \frac{1}{16\pi G}\int d^4x f(R) + A_m \ (3)$$

where $f(R)$ is a general function of Ricci scalar.

The variation of the action (3) w.r.t. $g_{\mu\nu}$ gives

$$F(R)R_{\mu\nu} - \frac{1}{2}g_{\mu\nu}f(R) - \nabla_\mu \nabla_\nu\, F(R) + g_{\mu\nu}\,\Box F(R) = 8\pi G T_{\mu\nu} \quad (4)$$

Where $F(R) = \frac{\partial f(R)}{\partial R}$, $\nabla_\mu$ is the covariant derivative and $\Box$ is the D'Alembertian operator. The trace of the field equation (4) is given by

$$3\Box F(R) + F(R)R - 2f(R) = 8\pi G T \quad (5)$$

where $T = -\rho + 3p$. Here $\rho$ and $p$ are the energy density and pressure of the matter, respectively. In the form of Klein-Gordon equation, the potential of the scalar field depends upon the trace of the energy-momentum tensor. The mass of the scalar field particle becomes larger in the high density region of the non-relativistic matter.

We rewrite the action (3) in the form

$$A = \frac{1}{16\pi G}\int d^4x \left(\frac{F(R)R}{2\kappa^2} - U\right) + A_m \quad (6)$$

where $U = \frac{F(R)R - f(R)}{2\kappa^2}$. For the solution of dark matter problem we consider the Einstein frame. It is possible to derive an action in the Einstein frame under the conformal transformation

$\widetilde{g_{\mu\nu}} = \Omega^2\, g_{\mu\nu}$ (7)

where $\Omega^2$ is the conformal factor and a tilde denotes the quantities in the Einstein frame. Thus, the action (6) under the conformal transformation is transformed as

$$A = \frac{1}{16\pi G}\int d^4x\sqrt{-\tilde{g}}\left[\frac{1}{2\kappa^2}F(R)\Omega^{-2}\left(\tilde{R} + 6\widetilde{\Box}\omega - 6\widetilde{g_{\mu\nu}}\partial_\mu\omega\partial_\nu\omega\right) - \Omega^{-4}U\right] + A_m \quad (8)$$

where $\omega = ln\Omega;\ \partial_\mu\omega \equiv \frac{\partial\omega}{\partial\widetilde{x^\mu}}$

The action (8) becomes linear in $\tilde{R}$ by choosing

$\Omega^2 = F(R)$ (9)

We consider a new scalar field $\phi$ defined by

$\kappa\phi = \sqrt{\frac{3}{2}}\, lnF$ (10)

Using these relations the action in Einstein frame is given as

$$A = \frac{1}{16\pi G}\int d^4x\sqrt{-\tilde{g}}\left[\frac{1}{2\kappa^2}\tilde{R} - \frac{1}{2}\widetilde{g_{\mu\nu}}\partial_\mu\phi\partial_\nu\phi - V(\phi)\right] + A_m \quad (11)$$

where $V(\phi) = \frac{U}{F^2} = \frac{FR - f}{2\kappa^2 F^2}$.

## 4. Gravitational Waves in $f(R)$ gravity models:

To derive the equations of GWs, we take perturbations in the metric tensor $g_{\mu\nu}$ and scalar field $\phi$ given as

$g_{\mu\nu} = b_{\mu\nu} + h_{\mu\nu}$ (12)

$\phi = \phi_{min} + \varphi$ (13)

where $b_{\mu\nu}$ is the background metric and $h_{\mu\nu}$ is the small perturbation in the background metric. $\phi_{min}$ is the value of the scalar field at which the effective potential of the scalar field is minimum and $\varphi$ is the small perturbation.

Now taking the first order perturbation in field equation, we get the perturbed equation given as

$$(\nabla_\mu^b \nabla_\nu^b - b_{\mu\nu}\Box^b - R_{\mu\nu}^b)\varphi = \phi_{min}\,\delta R_{\mu\nu} - \frac{1}{2}\phi_{min}\delta R b_{\mu\nu} - \frac{1}{2}f(R^b)h_{\mu\nu}$$

$$-\tfrac{1}{2}b_{\mu\nu}\left(2\nabla_\alpha^b h_\rho^\alpha - \nabla_\rho^b h\right)\nabla_b^\rho\phi_{min} - b_{\mu\nu}h^{\alpha\beta}\nabla_\alpha^b\nabla_\beta^b\phi_{min}$$

$$+\tfrac{1}{2}(\nabla_\mu^b h_{\nu\rho} + \nabla_\nu^b h_{\mu\rho} - \nabla_\rho^b h_{\mu\nu})\nabla_b^\rho\phi_{min} \quad (14)$$

where the covariant derivatives are calculated in the background metric. Now taking the perturbations in the trace equation, we get

$$(\Box^b - m_\varphi^2)\varphi = -\tfrac{1}{3}\phi_{min}h_{\mu\nu}R_{\mu\nu}^b + \tfrac{1}{6}f(R^b)h + \tfrac{1}{2}\left(2\nabla_\mu^b h_\rho^\mu - \nabla_\rho^b h\right)\nabla_b^\rho\phi_{min} + \tfrac{4}{3}h^{\mu\nu}\nabla_\mu^b\nabla_\mu^b\phi_{min} \quad (15)$$

The mass of the scalar mode of the GWs ($m_\varphi$) is given as

$$m_\varphi^2 = \frac{1}{3}\left(\frac{f'(R^b)}{f''(R^b)} - R^b\right) \quad (16)$$

where $f'(R^b)$ and $f''(R^b)$ are first and second derivatives of $f(R)$ with respect to $R$ at the value of Ricci scalar for background metric. Since the mass of the scalar mode depends upon the form of $f(R)$ models, we would investigate the different cosmologically viable $f(R)$ model. Here, we have neglected the perturbation in the energy momentum tensor. But, if we do not take matter into account, chameleon mechanism will not work. We can consider the matter and see its effect on the GWs through chameleon mechanism. We have studied the dark matter as scalaron in $f(R) = \frac{R^{1+\delta}}{R_c^\delta}$ gravity model [54], in which the mass of the scalar field particle is environment dependent.

In modified gravity, the energy density of the non-relativistic matter in the environment plays an important role. In ΛCDM model, the mass of the scalar field becomes infinite and propagation of the scalar mode ceases. While in the $f(R)$ models, the mass of the scalar mode is finite but increases with the increase in the energy density of non-relativistic matter. Therefore, the detection of scalar modes is possible in $f(R)$ or modified gravity models. In the earth's environment, the mass of the scalar field particle becomes very high and the propagation of the scalar mode of GWs ends. Thus, the scalar mode of GWs is suppressed in the earth's atmosphere and we get only tensor modes of GWs. The results of the space based GWs detectors will be very useful for results of our proposed research.

The Indian Initiative in Gravitational-wave Observations (INDIGO) is actively involved in establishing the GW detectors in India [34-40]. The Institute of Plasma Research (IPR) in Bhat, the Inter-University Centre for Astronomy and Astrophysics (IUCAA) in Pune, and the Raja Ramanna Centre for Advanced Technology (RRCAT) in Indore are the three leading national institutes in the INDIGO partnership. INDIGO presently has over 100 scientists on board, with members hailing from a variety of countries. The group wants to use them to learn more about gravity's core physics and to advance the discipline of gravitational wave science as an astronomical discovery tool [41-48].

The hunt for general deviations in Einstein's GR theory is being fueled by future GW probes, which has become a very active topic in recent years [49-53].

## 5. Conclusions and future directions:

Our study will give us knowledge about a viable theory of gravity. So far we have a lot of research on the production of GWs in ΛCDM model. We do not know what new properties of GWs will arise in a modified gravitational theory. My proposed research will attempt to answer this question. It will crucially decide, which of the two theories-GR or the modified gravity represents the correct model for the evolution of the universe. In future observations, if we are able to find the scalar modes of polarization in GWs, it will favor the modified gravity. My research will make a significant contribution in answering these questions which are unknown at present. In the proposed research work, I will investigate the modified gravity models in dealing with dark energy and dark matter problems. The importance of the proposed study lies in the fact that it will attempt to answer the crucial questions about the evolution of the universe by resolving the conflict in the choice of the cosmological models. It is known that the Lambda Cold Dark Matter model has been quite successful in explaining the dynamics of the universe across the early to present epochs, but the puzzles of the dark matter, dark energy and the cosmological constant problem (why its present value as the dark energy is too small?) are unsolved in this model. The problem of dark matter mainly cropped up seriously after the galactic rotation profiles were found as flat, and this model could explain it only by assuming the existing of an exotic form of matter, known as dark matter. Similarly, the Supernovae type I observations in 1998 indicated an accelerated expansion of the universe, which this model explained by assuming as being driven by a cosmological constant, or by dynamical dark energy, in some of its variants. Neither dark matter nor dark energy has so far been detected in experiments.

The well known cosmological constant problem within this model further complicates the issue, which remains unsolved. Being motivated to avoid the need of dark matter and dark energy, the Principal Investigator and his group have already worked in the alternative modified versions of Einstein's gravity that would give rise to modified cosmological models. These models are based on very small modification in the geometric part of the Einstein-Hilbert action and produce their own scalar field that can be seen to be minimally coupled in Einstein's frame. Our past work has shown that this approach of understanding gravity can reproduce well the effects conventionally attributed to the hitherto unknown dark matter and dark energy as mentioned above. This was shown to be supported by the astrophysical observations of galactic rotation profiles and light deflection angles etc.

Of course, that is not enough and we need some strong physical perspective to prefer our model to the Lambda Cold Dark Matter model. Searching for this perspective, we soon realized that the gravitational waves, first discovered at the advanced LIGO and Virgo detectors in 2015 and subsequently for various objects including neutron star mergers etc., could provide a powerful tool for observational diagnostics leading to a viable cosmological model.

The present proposal is set to sail in this state of uncertainty and confusion, and therein stands the strong urge to distinguish among the cosmological models. We plan to study the gravitational waves, especially their polarization and various effects that the scalar fields produce in modified gravity. Of course, such effects would be absent in Lambda Cold Dark Matter model. Thus, the scalar modes in gravitational waves, if detected in future observations at India-LIGO or elsewhere, will clearly go in favour of modified gravity. On the other hand, if they are not detected at the earth-based detectors, we can further constrain the models with some kind of chameleon mechanism, that may act as a screening mechanism.

Our stuy provides us knowledge about a viable theory of gravity, may also save money in searches for candidates as dark matter and dark energy. At present, we have a lot of research on the production of GW's in ΛCDM model, but we do not know much which new properties of GW's will arise in a modified gravity.

Our research will also attempt to answer this important question. It will crucially decide, which of the two theories - GR or the modified gravity at cosmic scales represents the correct model for the evolution of the universe. The study will also open several questions to be settled by future experiments in gravitational waves leading to the concordance model. Our research will make a significant contribution by answering these questions which are unanswered at present.

**References:**

[1] A. G. Riess et al., (Supernova Search Team Collaboration), Astron. J. 116, 1009 (1998).

[2] B. Schmidt et al., Astrophys. J. 507, 46 (1998).

[3] S. Perlmutter et al., Astrophys. J. 517, 565 (1999).

[4] M. Kunz and D. Sapone, Phys. Rev. Lett. 98, 121301 (2007).

[5] L. Amendola, R. Gannouji, D. Polarski and S. Tsujikawa, Phys. Rev. D 75, 083504 (2007).

[6] V. Sahni and Y. Shtanov, JCAP 0311, 014 (2003).

[7] A. A. Starobinski, Phys. Lett. B 91, 99(1980).

[8] S. Nojiri and S. D. Odintsov, Phys. Rept. 505, 59 (2011).

[9] B. K. Yadav and M. M. Verma, Int. J. Mod. Phys. D 26, 1750183 (2017).

[10] V. C. Rubin, W. K. Ford and N. Thonnard, Astrophys. J. 238, 471 (1980).

[11] A. Borriello and P. Salucci, Mon. Not. R. Astron. Soc. 323, 285 (2001).

[12] G. Jungman, M. Kamionkowski and K. Griest, Phys. Rep. 267, 195 (1996).

[13] D. N. Spergel et al., Astrophys. J. Suppl. 148, 97 (2003).

[14] S. M. Carroll, Living Rev. Relativ. 4, 1 (2001).

[15] P. J. E. Peebles and Bharat Ratra, Rev. Mod. Phys. 75, 559 (2003).

[16] R. R. Caldwell, R. Dave, and P. J. Steinhardt, Phys. Rev. Lett. 80, 1582 (1998).

[17] S. Capozziello, Int. J. Mod. Phys. D 11, 483 (2002)

[18] T. Chiba, T. Okabe, and M. Yamaguchi, Phys. Rev. D 62, 023511 (2000).

[19] R. R. Caldwell, Phys. Lett. B 545, 23 (2002).

[20] C. G. Boehmer, T. Harko and F. S. N. Lobo, Astropart. Phys. 29, 386 (2008).

[21] T. Katsuragawa and S. Matsuzaki, Phys. Rev. D 95, 044040 (2017).

[22] R. Zaregonbadi, M. Farhoudi and N. Riazi, Phys. Rev. D 94, 0840052 (2016).

[23] S. Nojiri and S. D. Odintsov, Proceedings, 17th Workshop on General Relativity and Gravitation in Japan (JGRG17): Nagoya, Japan, December 3-7, 2007, 03, (2008).

[24] V. Sahni and L. Wang, Phys. Rev. D 62, 103517 (2000).

[25] S. S. Mishra, V. Sahni and Y. Shtanov 06, 045 (2017).

[26] M. S. Turner, Phys. Rev. D 28, 1243 (1983).

[27] M. M. Verma and B. K. Yadav, Int. J. Mod. Phys. D 27, 1850002 (2018).

[28] P. Creminelli and F. Vernizzi, Phys. Rev. Lett. 119, 251302 (2017).

[29] C. P. L. Berry and J. R. Gair, Phys. Rev. D 83, 104022 (2011).

[30] P. I. Dyadina, J. Exp. Theor. Phys. 135, 333 (2022).

[31] H. R. Kausar, L. Philippoz and P. Jetzer, Phys. Rev. D 93, 124071 (2016).

[32] T. Katsuragawa, T. Nakamura, T. Ikeda and S. Capozziello, Phys. Rev. D 99, 124050 (2019).

[33] B. P.Abbott *et al.* (Virgo and Ligo Scientific Collaborations),Phys. Rev. Lett. 119, 161101 (2017).

[34] S. Bose, A. Pai, and S. Dhurandhar, Int. J. Mod. Phys. D 9 (3), 325 (2013).

[35] C. Unnikrishnan, Int. J. Mod. Phys. D 22, 1341010 (2013).

[36] T. Souradeep, LIGO-India. Resonance 21 (3), 225-231 (2016).

[37] T. Souradeep, S. Raja, Z. Khan, C. S. Unnikrishnan, B. Iyer, Current Science, 672-677 (2017).

[38] S. V. Dhurandhar, and J. V. Narlikar, Class. Quant. Grav. 35(13), 135003 (2018).

[39] S. Bose, S. Dhurandhar, A. Gupta, and A. Lundgren, Phys. Rev. D 94 (12), 122004 (2016)

[40] A. Ghosh et al., Class. Quant. Grav. 35(1), 014002 (2017).

[41] T. Padmanabhan, Gravitation: Foundations and Frontiers, Cambridge University Press (2010).

[42] R. X. Adhikari et al., 36 (24), 245010 (2019).

[43] A. Ghosh, W. D. Pozzo, and P. Ajith, Phys. Rev. D 94(10), 104070 (2016).

[44] A. K. Mehta et al., Phys. Rev. D 100 (2), 024032 (2019).

[45] P. Ajith, B. R. Iyer, C. A. K. Robinson, B. S. Sathyaprakash, Phys. Rev. D 71 (4), 044029 (2005).

[46] A. Vijaykumar, S. J. Kapadia, and P. Ajith, Phys. Rev. Lett. 126 (14), 141104 (2021).

[47] S. Goyal, K. Haris, A. K. Mehta, and P. Ajith, Phys. Rev. D 103(2), 024038 (2021).

[48] M. Saleem et al., Class. Quant. Grav. 39(2), 025004 (2021).

[49] S. J. Kapadia, The Astrophysical Journal Letters 910 (1), L4 (2021).

[50] S. Jana, G. K. Chakravarty, and S. Mohanty, Phys. Rev. D 97, 084011 (2018).

[51] D. J. Gogoi, and U. D. Goswami, Eur. Phys. J. C 80, 1101 (2020).

[52] S. Jana, S. Mohanty, Phys. Rev. D 99, 044056 (2019).

[53] S. Bhattacharyya and S. Shankaranarayanan, Phys. Rev. D 96, 064044 (2017).

[54] B. K. Yadav and M. M. Verma, JCAP 10, 052, (2019)

# CHARACTERISTICS OF SMART MANUFACTURING

**Rimpy Chabra*[1], Sanjay Kumar Yadav[1], Vineet Singh[1] and Birendra Kumar Barik[2]**
[1]Mechanical Engineering Department,
IFTM, University Moradabad, Uttar Pradesh, India
[2]Production Engineering Department,
Veer Surendra Sai University of Technology Burla, Odisha, India
*Corresponding author E-mail: rimpy.chabra@iftmuniversity.ac.in

**Abstract:**

Smart Manufacturing attempts to maximize the capabilities of sustainable competitiveness considering the following parameters that are cost, quality, quantity, delivery, and flexibility. In this study the typical characteristics of smart manufacturing are discussed which includes collaboration and integration network, service-oriented manufacturing, knowledge-intensive innovation, customer oriented and other approaches. Smart manufacturing presents the following key characteristics contributing to shaping the future of manufacturing enterprises. SM realizes collaborative design, distributed manufacturing, collective innovation, virtualization of resources, customer and service oriented with environmental, economical, and social sustainability. Smart manufacturing based on an open platform, open architecture, and open marketplace which is flexible, affordable and accessible to all. Smart manufacturing provides standardized services over collaborative networks, no need to buy hardware and software but services.

**Keywords:** Smart Manufacturing System; Characteristic.

## 1. Introduction:

Smart Manufacturing Systems (SMS) attempt to maximize cost delivery flexibility and quality by using advanced technologies that promote rapid flow and widespread use of digital information within and between manufacturing systems. SMS use information and communication technologies along with intelligent software applications to optimize the use of labor, material, and energy to produce customized, high quality products for on time delivery with faster, more responsive and closer to customers and quickly respond to changes in market demands and supply chains. SMS is also characterized by distributed, decentralized, and networked compositions of autonomous systems [1]. Digitization of every manufacturing part for interoperability and enhanced productivity. The typical characteristics of factories of the future shown in Fig. 1.

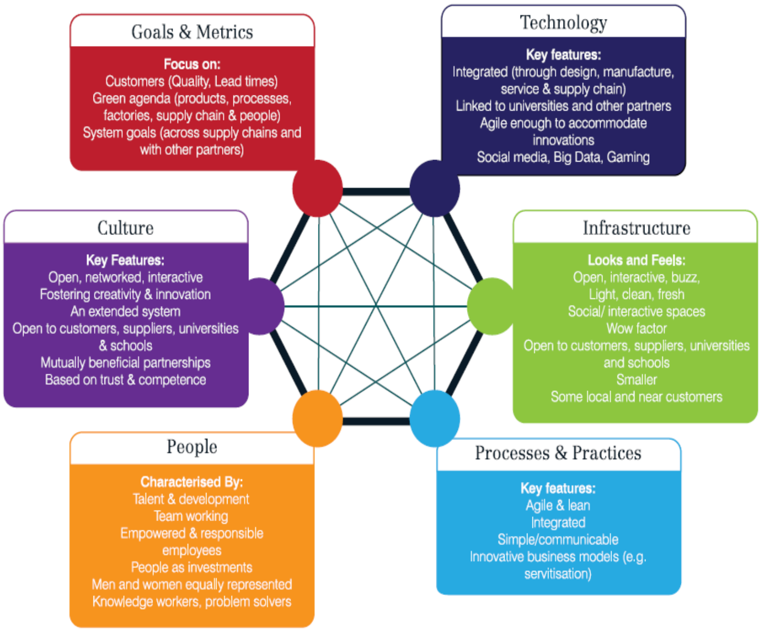

**Fig. 1: Characteristics of factories of the future [2]**

## 2. Collaboration and Integration Network:

Smart Manufacturing cloud based open access platform provide highly accessible, industry driven, and enabling infrastructure. The SM platform, architecture, and marketplace supports real time, high value applications for manufacturers to optimize production systems and value chains to radically improve sustainability, productivity, innovation, quality, and customer service. It presents a transformative business model, enabling companies of all sizes to gain easy, affordable, and timely access to an infrastructure and modeling, simulation and analytical technologies that can be tailored to meet cross industry business case requirements [3].

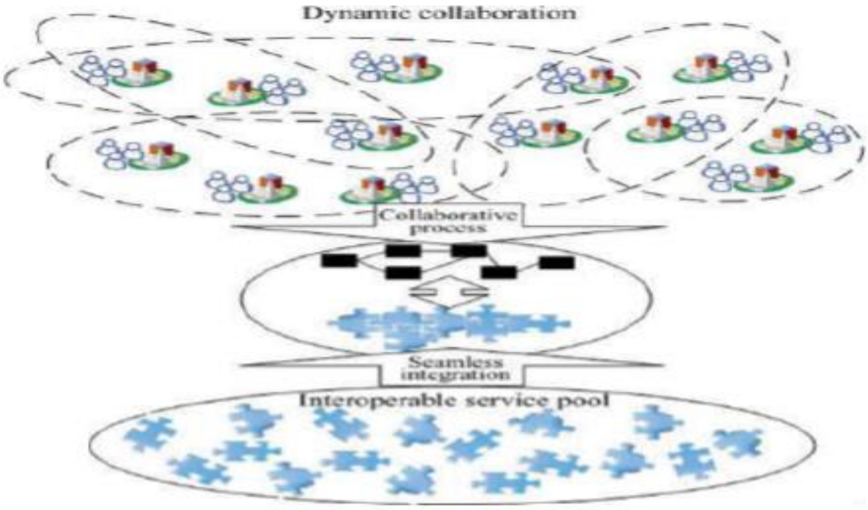

**Fig. 2: Collaboration and integration platform of SM [4]**

As shown in Fig. 2, distributed manufacturing resources are interconnected through a cyber infrastructure and providing a shared open platform to promote cooperation. Through interoperability data can be share by software and hardware on different machines from different vendors in network enterprises [5]. Cloud based SM platform create a cyber business environment, where any suppliers or prosumers can easily find cooperative partners meeting their requirements [6]. This can be achievable by the digitization and virtualization of manufacturing resources. SM system predicts, solves, improves, manages, and controls problems of production and link to actual one in virtual environment [7]. IoT based collaborative manufacturing can be realized using various networking technologies which enabled the collaboration and sharing of manufacturing resources for geographically or remote users. Different types of industries can converge in the SM open platform which can produce innovative products and services [8]. Distributed manufacturing resources can be interconnected to provide a shared platform for cooperation in humans-computers-things collaborative manufacturing environments [9]. Virtual pool of diverse manufacturing resources can be used through convenient and flexible pay as you go mode. Similarly, cloud system facilitates the management and sharing of manufacturing data and information in the SM environment [6].

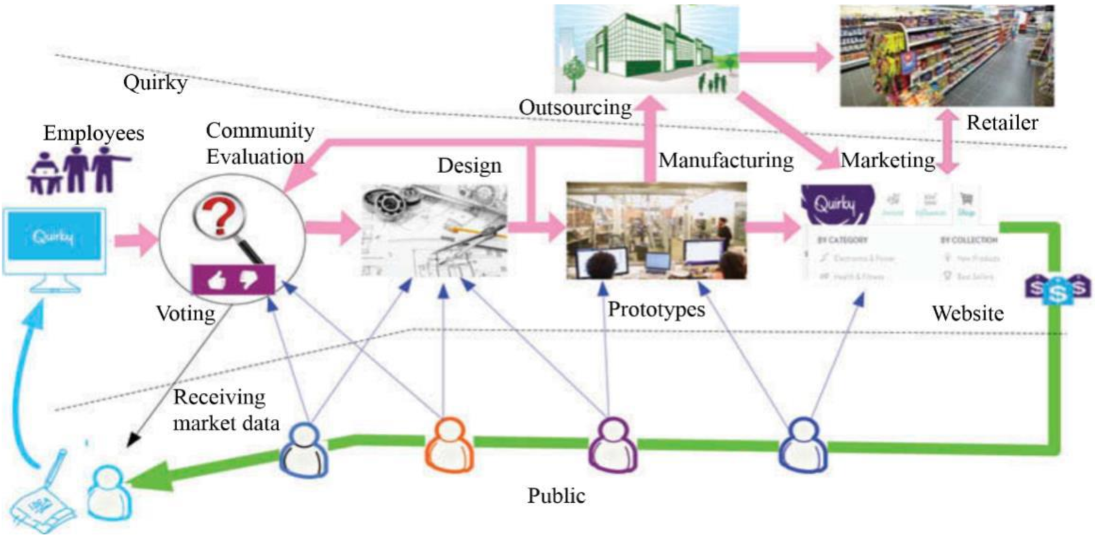

**Fig. 3: Quirky collaborative and integration business model [8]**

Social platform in enterprise environments enables through social networks and social media for social interaction and business collaboration. Integrating social media technology with customer relationship management makes easier and immediate collaboration, internally or externally in enterprises. One of the examples is open platform Quirky as shown in Fig.3, turns people’s ideas into products through interaction between online global communities and their expert product design staff with consumer to provide collaborative or open innovation in global context. Anyone can submit an idea and communities can vote the ideas and offers comments. If the idea passes through community evaluation, then design, prototype, outsourcing for manufacturing the product which can sold directly through Quirky website as well as through retail chains [8].

### 3. Service-oriented Manufacturing:

High quality services in manufacturing enterprises can be realized through cloud based smart manufacturing system [1]. Goods and services are becoming indistinguishable and are co-produced as servgoods in real time mass customization of SM environment where consuming customers are at the same time the co-producing producers. In addition SM is about integration of demand and supply chain or we can say supply chain becomes demand driven chain.Smart manufacturing services can be considered as ‘manufacturing as service’ [6] because it includes infrastructure as a service (IaaS), platform as a service (PaaS), software as a service (SaaS), workflow as a service, marketplace as a service, design as a service, production as a service, testing as a service, and logistic as a service as shown in Fig.4. SM environment provides almost all services through open platform with the help of cheaper and affordable emerging networks. It also provides standardized services over collaborative networks, no need to buy hardware and software but services. Virtual pool of diverse manufacturing resources can be used through convenient and flexible pay as you go mode. Similarly, cloud system facilitates the management and sharing of manufacturing data and information in the SM environment [6]. Open architecture of workflow as a service provides IT resources, cloud resources, enable enterprise modeling, and accessible infrastructure in heterogeneous manufacturing environment.

**Fig. 4: Manufacturing as a Service [6]**

Smart manufacturing opens up new ways of creating value and employment, for example through downstream services. In order to provide innovative services smart algorithms can be applied to the big data recorded by smart devices. There are particularly significant opportunities for SMEs and business to business (B2B) services for smart manufacturing. SM provides global services through global manufacturing [6]. The current workforce will get continuous improving training and also smart manufacturing is supporting next generation workforce to create flexible workforce environment, and also provides distributed capacity for skill formation in young people. Service oriented smart manufacturing adopted the idea of service oriented architecture (SoA) National institute of standards and technology is developing service oriented architecture for smart manufacturing to include cloud, on premise, and hybrid service oriented systems with scalable mechanisms of manufacturing resources in real time. And also performing composability analysis of software and physical manufacturing resources.

**4. Knowledge-intensive Innovation:**

Smart Manufacturing emphasizes the importance of knowledge that encourages knowledge reuse in innovative manufacturing, since innovation has become one of the most critical factors in manufacturing enterprises competitions [9]. Best use of knowledge helps to establish and achieve efficient and effective production of products and services in the SM environments. SM is the knowledge based intelligent manufacturing which helps in wisdom generation. In addition, intelligent processing and real-time decision making for wisdom generation is enabling by artificial intelligence (AI), for example evolutionary algorithm and neural networks. Wisdom is to establish and achieve goals using the knowledge. Wisdom manufacturing is featured by the best use of knowledge with blended intelligence [8].

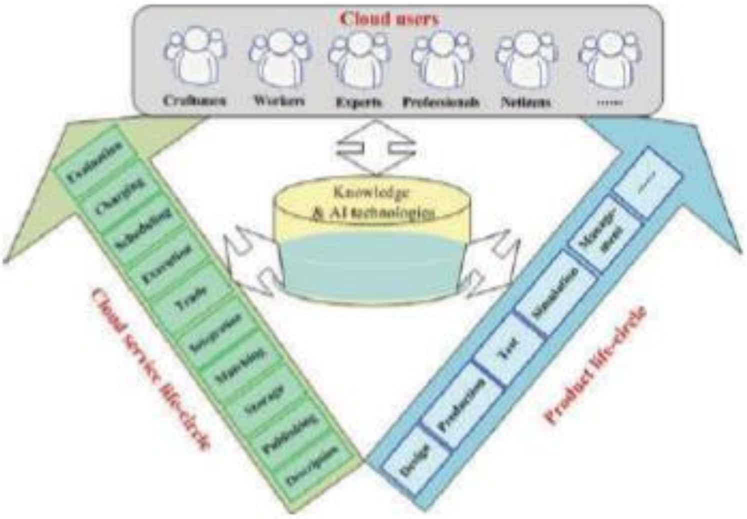

**Fig. 5: Cloud based knowledge intensive manufacturing [4]**

As shown in Fig. 5, knowledge and AI technologies are pervasive to providing support for product and service life cycle. It plays important role in promoting innovation and improving efficiency in all stages of product life cycle and also cloud services for whole life cycle. Knowledge may come from any cloud users ranging from craftsman to professionals. Manufacturing cloud provides a social platform for communicate and share ideas through which collective innovation or social innovation can be achieved [1].

## 5. Customer Oriented and other Approach:

Smart manufacturing is connecting and integrating customers in a new ways. Data and information gathered through intelligent products and services can enable manufacturers to better understand their customers and provides improve the aftermarket experience and Market and sell products and services more intelligently. More transparent interaction of object and customer to produce personalized tailor made products and services [10][8]. Customer can know the status of their product in the manufacturing plant. Other characteristics includes plug and produce, which is similar to plug and play computing concept, scalability of manufacturing resources and services through model based manufacturing, modularity where smart factory are assembled from flexible production modules connected to standardized infrastructure to meet changing requirements and capacity needs [7], multimodal interaction in augmented reality manufacturing environment, safety, security and more confidence manufacturing [6].

## 6. Conclusions

Major concluding remarks on characteristics of smart manufacturing are given below:

- Dynamic collaboration and seamless integration with efficient interoperability can be achievable in smart manufacturing environments.
- Through open, affordable, and accessible SM platform to marketplace transforming the manufacturing industry from a product oriented to service-oriented manufacturing.
- Manufacturing cloud act as a knowledge cloud in which multidisciplinary knowledge is polled that will promote knowledge intensive collaborative innovation in smart manufacturing environment

## References:

[1] H. S. PARK and N. H. TRAN, “Development of a cloud based smart manufacturing system,” *J. Adv. Mech. Des. Syst. Manuf.*, vol. 9, no. 3, pp. 1–24, 2015.

[2] K. Ridgway, “The factory of the future,” *Foresight*, 2013.

[3] M. P. Papazoglou and J. Van Den Heuvel, “Architecture and Knowledge- Based Structures for Smart Manufacturing Networks,” *IEEE Softw.*, pp. 61–69, 2015.

[4] L. Ren, L. Zhang, L. Wang, F. Tao, and X. Chai, “Cloud manufacturing: key characteristics and applications,” *Int. J. Comput. Integr. Manuf.*, vol. 3052, pp. 1–15, February 2014.

[5] KangH. S., Lee J. Y., ChoiS., KimH., ParkJ. H., SonJ. Y., KimB. H., Noh D.: Smart manufacturing: Past research, present findings, and future directions. Int. J. Precis. Eng. Manuf. Technol 3(1),111–128, (2016).

[6] G. Adamson, L. Wang, M. Holm, and P. Moore, “Cloud manufacturing – a critical review of recent development and future trends,” *Int. J. Comput. Integr. Manuf.*, vol. 3052, pp. 1–34, February 2015.

[7] D. Wu, D. W. Rosen, L. Wang, and D. Schaefer, “Cloud-based design and manufacturing: A new paradigm in digital manufacturing and design innovation,” *CAD Comput. Aided Des.*, vol. 59, pp. 1–14, 2015.

[8] X. Yao, H. Jin, and J. Zhang, “Towards a wisdom manufacturing vision,” *Int. J. Comput. Integr. Manuf.*, vol. 3052, pp. 1–22, March 2014.

[9] X. F. Yao, Z. T. Lian, Y. Yang, Y. Zhang, and H. Jin, “Wisdom manufacturing: new humans-computers-things collaborative manufacturing model,” *Comput. Integr. Manuf. Syst. CIMS*, vol. 20, no. 6, pp. 1490–1498, 2014.

[10] X. Yao and Y. Lin, “Emerging manufacturing paradigm shifts for the incoming industrial revolution,” *Int. J. Adv. Manuf. Technol.*, Nov. 2015.

[11] Smart Manufacturing Leadership Coalition, “SMLC Forum: Priorities, Infrastructure, and Collaboration for Implementation of Smart Manufacturing,” pp. 1–27, October 2012

[12] N. Sasaki, “The Leading Program for Innovation of Manufacturing in Japan,” Ger. Econ. Forum Hann. Messe, 2015

[13] X. Li, D. Li, J. Wan, A. V. Vasilakos, C.-F. Lai, and S. Wang, “A review of industrial wireless networks in the context of Industry 4.0,” Wirel. Networks, pp. 1–19, Nov. 2015.

[14] P. Jiang, K. Ding, and J. Leng, “Towards a cyber-physical-social-connected and service-oriented manufacturing paradigm: Social Manufacturing,” Manuf. Lett., vol. 7, pp. 15–21, 2016

[15] J. Davis, T. Edgar, J. Porter, J. Bernaden, and M. Sarli, “Smart manufacturing, manufacturing intelligence and demand-dynamic performance,” Comput. Chem. Eng., vol. 47, pp. 145–156, Dec. 2012

# PEROVSKITE SOLAR CELLS: FUNDAMENTALS, ADVANCEMENTS, AND FUTURE PROSPECTS

**Manish Kumar*[1], Ajeet Singh[1], Narender Singh[1], Priya Paneru[1], Jitendra Pal Singh[1], Atanu Nag[1], Bal Krishna Yadav[1], Richa Saxena[2] and Vidhi Goyal[1]**
[1]Department of Physics,
School of Sciences, IFTM University Moradabad-244102, Uttar Pradesh (India)
[2]Department of Physics,
Shri Guru Ram Rai University, Dehradun, Uttarakhand, India
*Corresponding author E-mail: mk82819@gmail.com

## Abstract:

One innovative photovoltaic technology that has cheap production costs, excellent power conversion efficiency, and ease of manufacturing is perovskite solar cells (PSCs). The construction of cells uses metal halide perovskite materials because of their remarkable optoelectronic properties, which include an adjustable bandgap characteristic, high absorption capacity, and extended carrier diffusion lengths. With rapid advancements over the last decade, PSCs now have power conversion efficiency comparable to that of actual silicon solar cells. Before PSCs can be widely used, they must solve the issues of lead pollution's effects on the environment, system scalability needs, and durability limits. The principles of perovskite solar cells are thoroughly covered in this chapter, along with updates on new materials and devices and methods to extend their lifetime and operational power. This discussion also focuses on future opportunities for PSC deployment with tandem devices, different compositions, and scalable deposition methods. Recent technological developments and existing constraint solutions promise that perovskite solar cells will transform the future of renewable energy generation.

**Keywords:** Perovskite Solar Cells (PSCs), Photovoltaics, Stability and Degradation, Fabrication Techniques, Perovskite Absorber Layer.

## 1. Introduction:

Renewable energy is still important for two primary reasons: it contributes to better living conditions in local economies, enhances national power networks, and regulates climate trends [1]. As the world's energy consumption rises and its finite resources diminish, the shift to renewable energy is essential for sustainable development. This shift reduces adverse environmental impacts, promotes technological advancements, and generates job possibilities [2]. Renewable energy sources, such as solar, wind, and hydropower, are essential for reducing greenhouse gas emissions because they effectively lower the risks associated with climate change [3]. The global carbon footprint is reduced when these renewable energy sources are used more widely because they lessen a country's reliance on fossil fuels for energy [4]. The implementation of renewable energy improves energy security by diversifying energy sources and reducing reliance on imported fuels. Due to the substantial rise spurred by the growing interest in renewable energy investments, 86% of global power output increased in 2023 [5]. In addition to improving social development and lowering poverty rates nationwide, the renewable energy industry is a major employer. Green technology evaluations spur economic growth, which in turn supports creative industries and increased market competitiveness [5]. Despite its well-established benefits, renewable energy confronts a number of obstacles, including high upfront costs, the need to build infrastructure, and limited market accessibility. The successful resolution of persistent operational issues is necessary for the full realization of sustainability through renewable sources [6]. In order to generate sustainable energy from solar energy, which has enormous potential as a renewable power source, photovoltaic technology is crucial [7]. The evolution of solar cells advanced significantly with the creation of perovskite solar cells (PSCs) [8].These cells are the subject of scientific research due to their excellent functioning, low-cost manufacturing processes, and tunable optoelectronic properties. Perovskite materials are defined by the $AMX_3$ crystal structure as a collection of chemicals that are present in this structure [9]. Methylammonium (MA), formamidinium (FA), and cesium (Cs) are among the organic or inorganic cations that make up the "A" ingredient of perovskite under this structure. The "X" element denotes a halide anion composed of iodide ($I^-$), bromide ($Br^-$), or chloride ($Cl^-$), while the "M" component represents a metal cation, such as lead (Pb) or tin (Sn) [10]. Perovskite's unique raw material combination enables the materials to efficiently absorb light energy and transfer charges in the direction of solar energy conversion. PSCs were first presented in 2009 by research by Kojima et al., which yielded an initial efficiency of 3.8% [11]. Since 2009, the research field has advanced astronomically, leading to PSC efficiency above 26% [12]. This significant increase in efficiency puts perovskite solar cells on par with conventional silicon solar cells, suggesting that solar technology approaches will likely be replaced in the future [13]. Researchers have demonstrated ongoing PSC progress, demonstrating their significance in creating cost-effective, efficient renewable energy solutions. Researchers who examine the scalability and stability of perovskite solar systems can help expand the use of solar energy, improving environmental sustainability worldwide [14]. This chapter explores the basic ideas, current developments, and prospective future applications of PSCs, providing information on their potential for broad commercialization.

## 2. The Role of Solar Cells in Clean Energy Solutions:

The role of solar cells in clean energy solutions is pivotal, as they harness sunlight to generate electricity, contributing significantly to sustainable energy systems. Recent advancements in solar technology, including developmentof various types of solar cells, have enhanced their efficiency and economic viability.

### *2.1 Types of Solar Cells*

- **First-generation Solar Cells:**The first-generation solar cell in PV technology is a single-junction cell made of wafers composed of single crystals or polycrystals[15]. Silicon-based solar cells are currently leading the PV market due to their "reasonable" processing cost and efficiency of 26% or higher[16]. Nevertheless, the drawback of silicon-based solar cells is their high cost and rigorous preparation requirements.
- **Second-generation solar Cells:** The amorphous silicon CIGS and CdTe, as well as thin-film photovoltaic devices, constitute the foundation of second-generation solar cells. Conversely, thin-film methods based on III-V semiconductors demonstrated high efficiency[17]. Consequently, this technology is less expensive; yet, the drawback of thin-film technology is that its power conversion efficiency (PCE) is comparatively lower than that of traditional crystalline silicon technology.
- **Third-generation Solar Cells:** Dye-sensitized solar cells (DSSCs), organic, quantum dot cells, polymer, and perovskite solar devices are all included in third-generation PV technology[18]. Perovskite materials' benefits, including their low raw material costs, superior PV performance, and simple production conditions, are driving study. The current study is predicated on perovskite solar cells.

### *2.2. Crystal Structure and Material Properties*

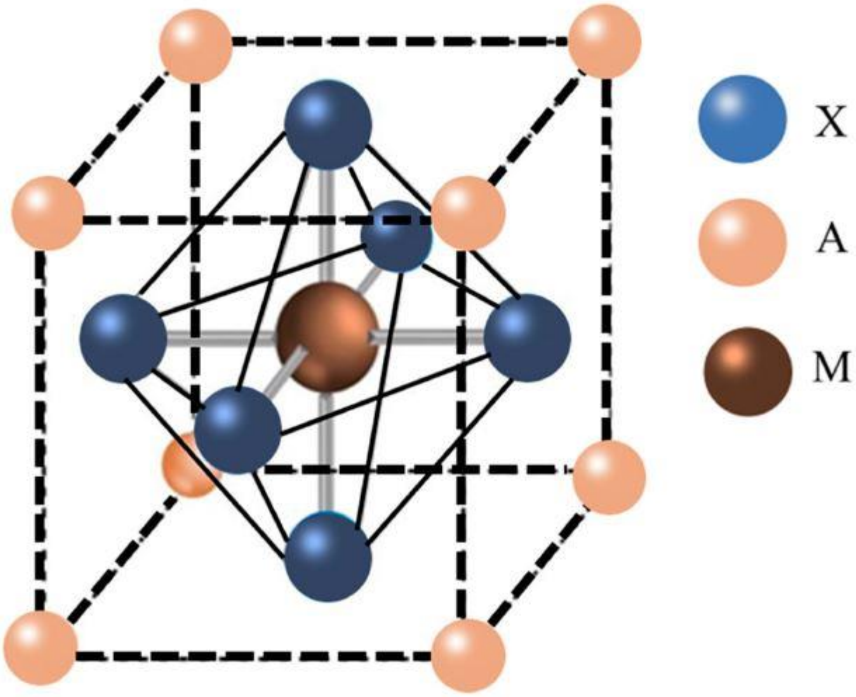

**Fig. 1:Shows the crystal structure of perovskite materials [19].**

A mineral having the chemical formula $CaTiO_3$ (calcium titanium oxide) is referred to as having a perovskite crystal structure. This mineral was named after Russian mineralogist L. A. Perovski by Gustav Rose, who discovered it in the Ural Mountains of Russia in 1839. This identical crystal structure can be found in materials with the general chemical formula $AMX_3$, where X is an anion and M and A are cations with varying ionic radii, with "M" being smaller than the "A" atoms. The perfect perovskite structure ($AMX_3$) is made up of a cubic cell with the M cation in the octahedral form 6-fold coordinated by X anions and the A octahedrally coordinated at the cubic cell's corners via 12-fold cuboctahedral coordination (Fig. 1) [20][21]. Chlorine (Cl), bromine (Br), or iodine (I) can be the X anion for the halide-based perovskite. The M cations are Sn ($Sn^{2+}$), Germanium ($Ge^{2+}$), or lead ($Pb^{2+}$). EA (ethylammonium, $CH_3CH_2NH^{3+}$), Rubidium ($Rb^+$), $MA^+$ (methylammonium, $CH_3NH_3^+$), FA (formamidinium $NH_2CH = NH_3^+$), and Cesium ($Cs^+$) are examples of M cations [22]. The stability of the crystal structure in the perovskite cubic structure is greatly dependent on the relative ion size.

Perovskite solar cells (PSCs), which are distinguished by their distinct optoelectronic characteristics and promise for high efficiency at low production costs, represent a substantial breakthrough in photovoltaic technology. Due to the worldwide interest in this discovery, significant advancements in stability, efficiency, and marketing tactics have been made. The salient features of this development are delineated in the subsequent sections.

## 3 Unique Properties and Efficiency

Perovskite materials exhibit high light absorption coefficients and long carrier diffusion lengths, enabling impressive power conversion efficiencies [23]. Recent advancements have seen efficiencies surpassing traditional silicon cells, particularly in tandem configurations [24].

### *3.1 Integration and Stability Challenges*

The integration of PSCs with energy storage systems has been challenging due to electrical mismatches and stability concerns.Innovations such as solid-state electrolytes have been developed to enhance stability and efficiency in integrated systems [25].

### *3.2 Commercialization Efforts*

The transition from laboratory to commercial production faces hurdles, including scalability and reproducibility of manufacturing processes.Automation and machine learning are being leveraged to optimize material combinations and streamline production [24].

At present, perovskites are being actively investigated wherein the power conversion efficiency has surpassed 25% (Fig.2). The fact that the power conversion efficiency has advanced so quickly in such a short time that it is starting to catch up to other technologies (silicon (Si) and thin film) is even more remarkable. It was even more impressive to see these results. Research on novel materials that exhibit PV effects and low-cost device architectures that allow for exceptional efficiency has been ongoing for several years. It has demonstrated exceptional performance in solar cell applications, according to reports. Accordingly, there are a few explanations for the tremendous efficiency of perovskite solar cells and their widespread appeal. They have been used as active materials due to their long charge carrier lifetime, high optical absorption (~$10^5$ $cm^{-1}$), low exciton binding energy (~10 meV), long carrier diffusion lengths (>1 μm), high open-circuit voltage, adjustable band gap (1.2 to 3.0 eV) (mixed halide (X= Cl, Br, I) perovskites), charge carrier mobility (~10 $cm^2$ $V^{-1}$ $s^{-1}$), and low fabrication costs.[27][28][29].Despite the encouraging developments in PSC technology, issues like long-term stability and large-scale production continue to be major obstacles to its broad use. Realizing perovskite solar cells' full potential in the field of renewable energy will require resolving these problems.

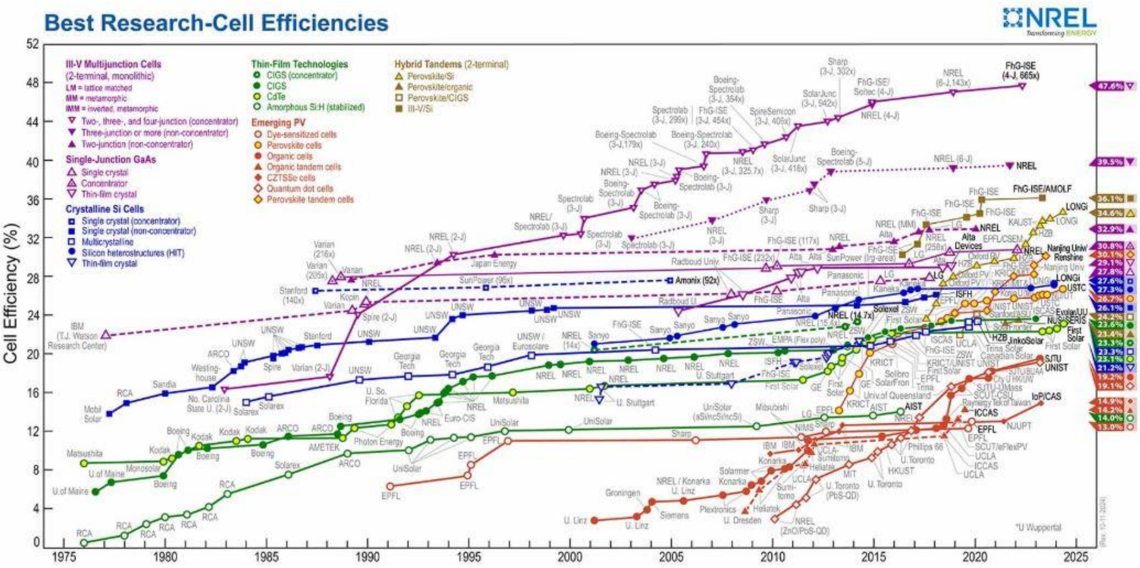

**Fig. 2: Power conversion efficiency trend with different technologies from NREL map [26].**

## 4. Principles of Perovskite Solar Cell Operation:

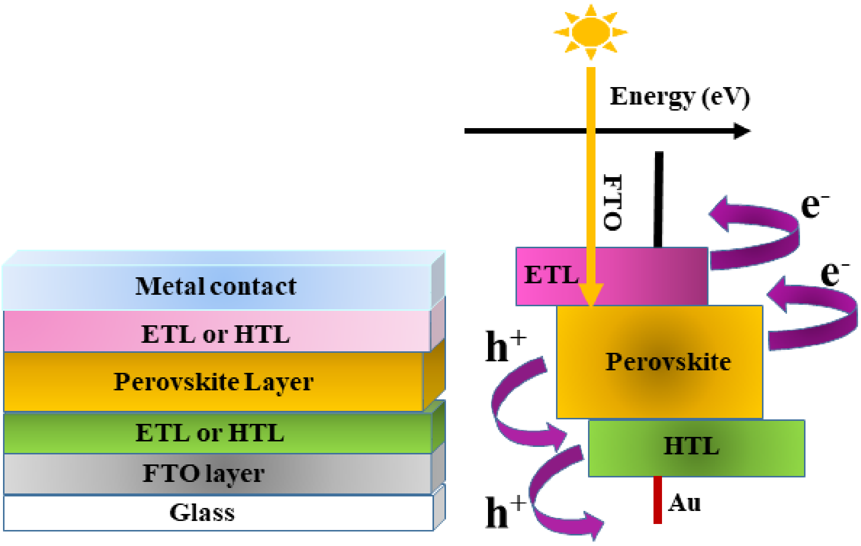

**Fig. 3: Shows an architect of a Perovskite solar cell.**

PSCs use perovskite-structured materials as light absorbers and work on the basis of the photovoltaic effect; their distinctive optoelectronic characteristics, like high light absorption and tunable band gaps, contribute to their high efficiency and low cost of production. The basic idea is that sunlight is absorbed, creating electron-hole pairs that are subsequently separated and transported to the appropriate electrodes; the quality of the perovskite layer and the interfaces with transport layers affect this process.

- **Light Absorption**: Because of their high absorption coefficient, perovskite materials are effective at absorbing sunlight[30].
- **Charge Generation**: Excitons, or electron-hole pairs, are produced when light is absorbed and need to separate into free carriers[31].
- **Charge Transport**: The electron transport layer (ETL) and hole transport layer (HTL) are used to move the produced electrons and holes, respectively. For efficiency, the dynamics of this transfer are essential[32].

### *4.1 Efficiency Factors*

- **Material Quality**: The lifetime and mobility of charge carriers are influenced by the crystal quality of perovskite films, and interface imperfections provide a major obstacle[33].
- **Interface Engineering**: Recombination losses can be decreased and charge extraction improved by optimizing the interfaces between the transport and perovskite layers [34].

## 5. Fabrication Techniques

The focus has been on perovskite solar cells (PSCs) due to their economical manufacturing approach as well as their efficient operation. The enhancement of manufacturing technology for PSCs includes techniques developed for manual and automated methods of production. Important approaches for making PSCs are discussed in detail throughout the following sections.

### *5.1 Low-Temperature Fabrication*

The focus of recent developments is on low-temperature synthesis for superior perovskite thin films, which are essential for enhancing charge carrier transport layers[35]. By eliminating the requirement for high-temperature treatments, methods like solution processing make it possible to create functional layers that improve performance and stability.

### *5.2 Manual Deposition Methods*

Researchers may conduct experiments without costly equipment thanks to the accessibility and affordability of manual procedures including drop casting, blade coating, and spray coating. [36].These techniques form the basis for creating automated procedures that can subsequently improve accuracy and scalability.

### *5.3 Printing Techniques*

The possibility of several printing techniques, including as inkjet, screen, and slot die printing, in large-scale production has been investigated [37][38].

These methods provide benefits in terms of controlling film formation and material utilization, both of which are critical for economic viability.

### *5.4 Innovative Material Integration*

It has been demonstrated that using new materials, including reduced graphene oxide and formamidinium lead iodide, increases productivity and lowers costs in the production of PSCs[39].This integration tackles issues with solar technology performance and sustainability.

Even while PSC manufacturing technology developments are encouraging, issues like material stability and repeatability still need to be thoroughly studied. For perovskite solar technology to be widely used, these problems must be resolved.

## 6. Future Directions and Innovations:

### *6.1 Lead-free and hybrid perovskite solar cells*

Perovskite solar cells (PSCs) with hybrid and lead-free designs have a bright future because to advancements meant to improve stability and efficiency while tackling environmental issues. Alternative materials and architectures that potentially perform better than conventional lead-based PSCs are the subject of increased research. The main developments and possible paths for this technology are described in the parts that follow.

**Multi-Absorber Structures:**$MASnI_3/CsGeI_3$ and other multi-absorber heterojunctions have shown great potential with a power conversion efficiency (PCE) of 16.15% under optimal conditions[40]. This strategy optimizes solar spectrum utilization, which is essential for enhancing the performance of lead-free PSCs.

**Alternative Materials:**Perovskites based on cesium-bismuth, such as $CsBiSCl_2$, have shown an impressive stability with a PCE of 10.38%, losing just 3% of their efficiency after 150 days in air[40].It is crucial to investigate elements like Sn, Ge, and Bi since they have qualities comparable to lead but are less hazardous [41][42].

**Inorganic Components:**All-inorganic lead-free perovskites are becoming more popular; materials such as $RbSnCl_3$ have PCEs of over 33.61% when paired with effective electron transport layers [43].This shift towards inorganic materials aims to enhance environmental stability and reduce degradation in humid conditions[42].

The development of lead-free PSCs is encouraging, but there are still obstacles in the way of reaching efficiencies on par with those of their lead-based counterparts. For this technology to reach its full potential and overcome these obstacles, more research is necessary.

### *6.2 Integration with Other Solar Technologies (Tandem Cells)*

The integration of tandem solar cells with other solar technologies presents significant opportunities for enhancing efficiency and reducing costs in photovoltaic systems. Future innovations are likely to focus on optimizing material compatibility, improving manufacturing processes, and expanding application versatility. The following sections outline key directions for this integration.

- **Advances in Material Compatibility**

**Hybrid Structures:**Studies on hybrid tandem arrangements, such organic/CIGS and perovskite/silicon, show promise for complementing absorption spectra, which might result in increased power conversion efficiency [44][45].

**Interconnection Layers:**By reducing energy loss at interfaces—a critical component in attaining high efficiency—new connectivity layers can improve hybrid tandem performance[46].

- **Manufacturing Innovations**

**Scalable Production:**Scalable processing approaches, including solution-based procedures for perovskite layers, are necessary to assure cost-effectiveness when moving from laboratory to industrial-scale manufacturing[44].

**Reliability Testing:**Commercial viability requires the establishment of strong testing procedures for performance and durability under real-world circumstances[44].

- **Expanding Applications**

**Photoelectrochemical Water Splitting:**Tandem cells' adaptability is being demonstrated by its exploration for uses outside the production of electricity, such as photoelectrochemical water splitting for the creation of hydrogen[47].

Although integrating tandem technologies has potential, there are still obstacles to overcome in order to guarantee long-term stability and cost competitiveness with more established solar technology. For tandem solar cells to be widely used, these problems must be resolved.

## 7. Future Directions:

**Tandem Configurations:** In tandem configurations, PSCs and silicon cells may improve overall performance and competitiveness in the market [48].

**Cost Reduction:** Continued research into low-cost materials and processes is crucial for making PSCs commercially viable[48].

Although PSC technology is showing promise, issues like long-term stability and environmental concerns about material toxicity are still major obstacles that must be overcome before it can be widely used.

## 8. Conclusion:

Perovskite solar cells, a revolutionary technology because of its remarkable efficiency, affordability, and tunable features, have completely changed the landscape of photovoltaic energy. These materials have demonstrated unparalleled potential, spanning the gap between research and real-world applications, from their fundamental principles of operation to their cutting-edge advancements. Despite the rapid developments, stability, scalability, and long-term durability remain important topics of focus. However, perovskite solar cells are slowly entering the market because of continuous improvements in material engineering, deposition techniques, and device architecture. Combining perovskites with tandem solar cells and cutting-edge fabrication methods further opens the door for next-generation energy solutions.

**References:**

[1] B. K. Sovacool, "The importance of comprehensiveness in renewable electricity and energy-efficiency policy," *Energy Policy*, vol. 37, no. 4, pp. 1529–1541, 2009.

[2] I. Dincer, "Renewable energy and sustainable development: a crucial review," *Renew. Sustain. energy Rev.*, vol. 4, no. 2, pp. 157–175, 2000.

[3] N. Y. Amponsah, M. Troldborg, B. Kington, I. Aalders, and R. L. Hough, "Greenhouse gas emissions from renewable energy sources: A review of lifecycle considerations," *Renew. Sustain. Energy Rev.*, vol. 39, pp. 461–475, 2014.

[4] S. Shafiee and E. Topal, "A long-term view of worldwide fossil fuel prices," *Appl. Energy*, vol. 87, no. 3, pp. 988–1000, 2010.

[5] L. C. A. Gutiérrez-Negrín, "Evolution of worldwide geothermal power 2020–2023," *Geotherm. Energy*, vol. 12, no. 1, p. 14, 2024.

[6] J. R. Aguero, E. Takayesu, D. Novosel, and R. Masiello, "Modernizing the grid: Challenges and opportunities for a sustainable future," *IEEE Power Energy Mag.*, vol. 15, no. 3, pp. 74–83, 2017.

[7] R. A. Marques Lameirinhas, J. P. N. Torres, and J. P. de Melo Cunha, "A photovoltaic technology review: History, fundamentals and applications," *Energies*, vol. 15, no. 5, p. 1823, 2022.

[8] S. A. Olaleru, J. K. Kirui, D. Wamwangi, K. T. Roro, and B. Mwakikunga, "Perovskite solar cells: The new epoch in photovoltaics," *Sol. Energy*, vol. 196, pp. 295–309, 2020.

[9] I. A. Apon, M. Ratul Hasan, and M. Islam, "First-principles investigation of structural, mechanical, and electronic properties of AMgX3 (A= Ga, In, Tl, and X= Cl, Br, I) perovskites for optoelectronic applications," *Phys. Scr.*, vol. 100, no. 1, p. 15931, 2024.

[10] J. M. Frost and A. Walsh, "What is moving in hybrid halide perovskite solar cells?," *Acc. Chem. Res.*, vol. 49, no. 3, pp. 528–535, 2016.

[11] S. Nair, S. B. Patel, and J. V Gohel, "Recent trends in efficiency-stability improvement in perovskite solar cells," *Mater. Today Energy*, vol. 17, p. 100449, 2020.

[12] S. Yun *et al.*, "New-generation integrated devices based on dye-sensitized and perovskite solar cells," *Energy Environ. Sci.*, vol. 11, no. 3, pp. 476–526, 2018.

[13] M. H. Futscher and B. Ehrler, “Efficiency limit of perovskite/Si tandem solar cells,” *ACS Energy Lett.*, vol. 1, no. 4, pp. 863–868, 2016.

[14] X. Tian, S. D. Stranks, J. Huang, V. M. Fthenakis, Y. Yang, and F. You, “Perspectives for sustainability analysis of scalable perovskite photovoltaics,” *Energy Environ. Sci.*, vol. 18, no. 1, pp. 194–213, 2025.

[15] M. V Dambhare, B. Butey, and S. V Moharil, “Solar photovoltaic technology: A review of different types of solar cells and its future trends,” in *Journal of Physics: Conference Series*, IOP Publishing, 2021, p. 12053.

[16] M. A. Fazal and S. Rubaiee, “Progress of PV cell technology: Feasibility of building materials, cost, performance, and stability,” *Sol. Energy*, vol. 258, pp. 203–219, 2023.

[17] Q. Li *et al.*, “Comparative study of GaAs and CdTe solar cell performance under low-intensity light irradiance,” *Sol. Energy*, vol. 157, pp. 216–226, 2017.

[18] A. Zdyb, *Third generation solar cells*. Routledge, 2023.

[19] M. S. Hasan *et al.*, “Recent Criterion on Stability Enhancement of Perovskite Solar Cells,” *Processes*, vol. 10, no. 7, 2022, doi: 10.3390/pr10071408.

[20] N. S. Kumar and K. C. B. Naidu, “A review on perovskite solar cells (PSCs), materials and applications,” *J. Mater.*, 2021.

[21] Z. Shi and A. H. Jayatissa, “Perovskites-based solar cells: a review of recent progress, materials and processing methods,” *Materials (Basel).*, vol. 11, no. 5, p. 729, 2018.

[22] M. Roknuzzaman, K. K. Ostrikov, H. Wang, A. Du, and T. Tesfamichael, “Towards lead-free perovskite photovoltaics and optoelectronics by ab-initio simulations,” *Sci. Rep.*, vol. 7, no. 1, pp. 1–8, 2017.

[23] Y. Li, “The Principle and Research Progress of Perovskite Solar Cells,” *Highlights Sci. Eng. Technol.*, vol. 106, pp. 347–352, 2024.

[24] Z. Xu *et al.*, “Advancing perovskite solar cell commercialization: Bridging materials, vacuum deposition, and AI-assisted automation,” *Next Mater.*, vol. 3, p. 100103, 2024.

[25] J. Bi *et al.*, “Highly Integrated Perovskite Solar Cells-Based Photorechargeable System with Excellent Photoelectric Conversion and Energy Storage Ability,” *Energy Environ. Mater.*, p. e12728, 2024.

[26] “Best Research-Cell Efficiencies,” *Nrel*, p. 2025, 2025, [Online].

[27] W. Guo *et al.*, “The Dion–Jacobson perovskite CsSbCl 4: a promising Pb-free solar-cell absorber with optimal bandgap∼ 1.4 eV, strong optical absorption∼ 10 5 cm− 1, and large power-conversion efficiency above 20%,” *J. Mater. Chem. A*, vol. 9, no. 30, pp. 16436–16446, 2021.

[28] Y. Chen *et al.*, “Extended carrier lifetimes and diffusion in hybrid perovskites revealed by Hall effect and photoconductivity measurements,” *Nat. Commun.*, vol. 7, pp. 1–9, 2016.

[29] M. Hu *et al.*, “Sub-1.4 eV bandgap inorganic perovskite solar cells with long-term stability,” *Nat. Commun.*, vol. 11, no. 1, pp. 1–10, 2020.

[30] Y. Li, H. Xie, E. L. Lim, A. Hagfeldt, and D. Bi, “Recent progress of critical interface engineering for highly efficient and stable perovskite solar cells,” *Adv. Energy Mater.*, vol. 12, no. 5, p. 2102730, 2022.

[31] Y. Yuan, T. Li, Q. Wang, J. Xing, A. Gruverman, and J. Huang, “Anomalous photovoltaic effect in organic-inorganic hybrid perovskite solar cells,” *Sci. Adv.*, vol. 3, no. 3, p. e1602164, 2017.

[32] C. Jiang *et al.*, “Revealing the hole and electron transport dynamics in the working devices for efficient semitransparent perovskite solar cells,” *Adv. Energy Mater.*, vol. 14, no. 17, p. 2304093, 2024.

[33] C. Fu *et al.*, “From structural design to functional construction: amine molecules in high-performance formamidinium-based perovskite solar cells,” *Angew. Chemie Int. Ed.*, vol. 61, no. 19, p. e202117067, 2022.

[34] Q. Hu, Y. Xiong, and Z. Xu, “Perovskite photovoltaic effect and its application on solar cell,” *Appl. Comput. Eng.*, vol. 60, pp. 63–68, 2024.

[35] S. H. Reddy, F. Di Giacomo, and A. Di Carlo, “Low-temperature-processed stable perovskite solar cells and modules: a comprehensive review,” *Adv. Energy Mater.*, vol. 12, no. 13, p. 2103534, 2022.

[36] N. Zarabinia and T. M. Brown, “Fabrication of Perovskite Solar Cells: A Focused Review on Manual Deposition Methods,” *Adv. Mater. Technol.*, p. 2400831.

[37] S. Soltani and D. Li, “Advancements in Manufacturing of High-Performance Perovskite Solar Cells and Modules Using Printing Technologies,” *Energies*, vol. 17, no. 24, p. 6344, 2024.

[38] M. A. Alharbi, S. Bhandari, and T. Mallick, “Review of Progress on Printing Techniques Towards Commercialization of Perovskite Solar Cells,” *Energies*, vol. 18, no. 1, p. 6, 2024.

[39] K. S. Velu, S. Mohandoss, M. Aslam, A. Manimekalai, N. Ahmad, and S. Sun, “Formamidinium Lead Iodide-Based Perovskite Solar Cell Fabrication With an Electrospun-Reduced Graphene Oxide Back Electrode: A Novel Approach,” *ChemistrySelect*, vol. 9, no. 42, p. e202404550, 2024.

[40] X. Huang, A. Yang, J. Li, L. Jiang, L. Lin, and Y. Qiu, “Improved Performance of Lead-Free Perovskite Solar Cells Based on Multi-Absorber MASnI3/CsGeI3 Heterojunction by Device Simulation,” *Adv. Theory Simulations*, vol. 7, no. 4, p. 2300790, 2024.

[41] S. Ahmed, M. A. Gondal, A. S. Alzahrani, M. Parvaz, A. Ahmed, and S. Hussain, “Recent

Trends and Challenges in Lead-Free Perovskite Solar Cells: A Critical Review," *ACS Appl. Energy Mater.*, vol. 7, no. 4, pp. 1382–1397, 2024.

[42] A. Kumar, S. K. Tripathi, M. Shkir, A. Alqahtani, and S. AlFaify, "Prospective and challenges for lead-free pure inorganic perovskite semiconductor materials in photovoltaic application: A comprehensive review," *Appl. Surf. Sci. Adv.*, vol. 18, p. 100495, 2023.

[43] M. S. Reza *et al.*, "Rubidium based new lead free high performance perovskite solar cells with SnS2 as an electron transport layer," *Mater. Today Commun.*, vol. 39, p. 108714, 2024.

[44] E. Aydin *et al.*, "Pathways toward commercial perovskite/silicon tandem photovoltaics," *Science (80-.).*, vol. 383, no. 6679, p. eadh3849, 2024.

[45] W. Zein, T. I. Alanazi, A. Saeed, M. M. Salah, and M. Mousa, "Proposal and design of organic/CIGS tandem solar cell: Unveiling optoelectronic approaches for enhanced photovoltaic performance," *Optik (Stuttg).*, vol. 302, p. 171719, 2024.

[46] Y. Ko, H. Park, C. Lee, Y. Kang, and Y. Jun, "Recent progress in interconnection layer for hybrid photovoltaic tandems," *Adv. Mater.*, vol. 32, no. 51, p. 2002196, 2020.

[47] B. Liu *et al.*, "Tandem cells for unbiased photoelectrochemical water splitting," *Chem. Soc. Rev.*, 2023.

[48] G. Murugadoss, "Perovskite Solar Cells: Current Strategy and Future Perspective," *Mater. Res. Found.*, vol. 163, 2024.

# RECENT ADVANCES AND TRENDS IN DEVICES AND SENSORS

**Priyanka*[1], Anil Kumar[1] and Manoj Kumar[2]**

[1]Department of Electrical Engineering,
School of Engineering and Technology, IFTM University, Moradabad-244102, India
[2]School of Engineering and Technology, IFTM University, Moradabad-244102, India
*Corresponding author E-mail: pri21image@gmail.com

**Abstract:**

Sensor devices have transformed human daily lives through applications in almost every field. Sensor is a device that detect changes in the source or surrounding area and collect signals and accordingly, the further process is interpreted. The sources of sensors used are light, temperature, movements, pressure etc. There is a wide range of application of innovative sensor technology in lifestyle, healthcare, fitness, manufacturing, and daily life span. In the medical field, the difficulty to taking medications is relaxed by a sensor by a drug dispenser. It reminds you to take medication using a signal and deliver the necessary medicine at the specific time. Sensor technology is extremely useful for health care ofseniors, athletes, and risk patients. This chapter discuss the recent advances and industrial trends.

**Keywords:** Technology, Everyday Life, Sensors

## 1. Introduction:

### *1.1 Introduction to Devices and Sensors*

Devices and sensors are essential components of modern technology and are the basis for a wide range of applications from home appliances to industrial systems, medical devices, and environmental monitoring. These devices can interact with the physical world, collect data that can be processed and analyzed to derive useful information. A Device is a physical unit that perform a task or set of tasks based on inputs and outputs.

There are two type of sensing Devices:

**a) Sensor**

Sensors are devices that recognize and measure physical phenomena such as temperature, motion, light, and sound, and convert them into east to read data signals.

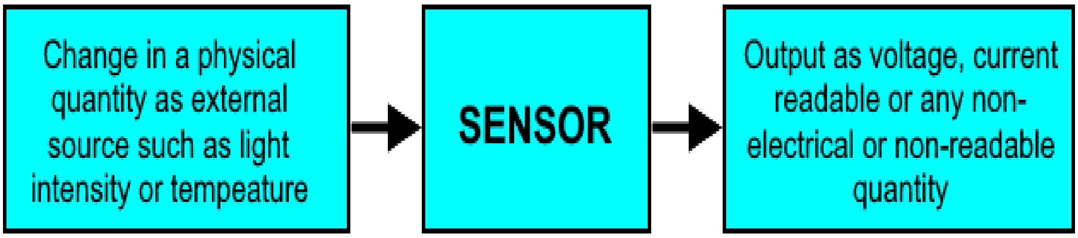

**Fig. 1: Electrical Sensor**

An example of a sensor is a temperature sensor.

These sensors detect temperature changes in the area and convert the physical temperature into an electricalsignal that can be read by a microcontroller or other device. A commonly used temperature sensor is the thermistor, which varies its resistance depending on temperature, or the thermocouple, which produces a voltage based on temperature differences.

### b) Transducer

A transducer is a device that converts one form of energy into another. It is often used to convert physical quantities such as pressure, temperature and light into electrical signals, or vice versa. These devices are extremely important in variety of systems such as measuring instruments, audio devices, and sensors.

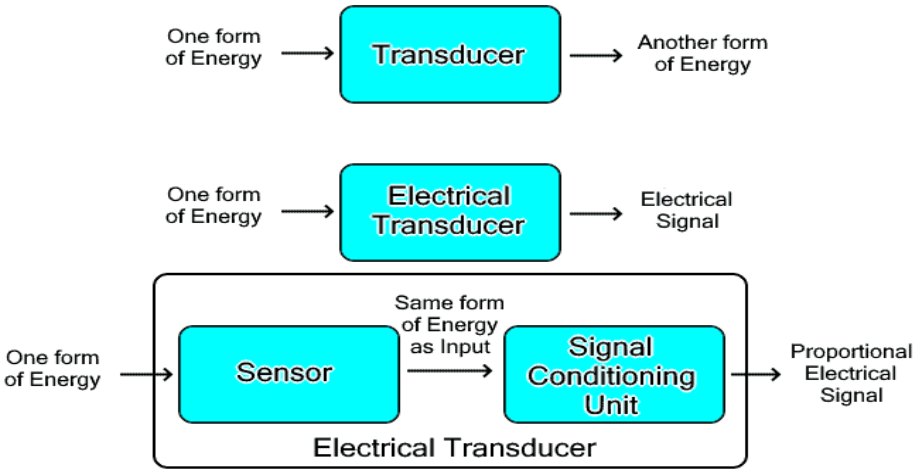

**Fig. 2: Electrical Transducer**

A transducer consistsof two parts; sensorand signal conditioning unit. The sensor recognizes changes in the physical environment and generates a non-electrical signal. The signal conditioning unit converts the signal into electrical form and also amplifies, attenuate or process it into an east to read electrical signal.

One example of a transducer is a microphone that converts acoustic energy intoelectrical energy. The microphone's diaphragm vibrates when it hits by sound waves, and these vibrations are converted by coil or capacitorinto corresponding electrical signals, which can be amplified or recorded.

### *1.2 Classification of Sensors*

Various specialists and researchers classify sensors in a variety of ways.

### 1) Based on Power Requirement

- **Active Sensors:** These Sensors require an external excitation signal or power source to work.
- **Passive Sensors**: These Sensors do not require any external power source and it can directly generate the output response.

### 2) Based on Means of Detection

The Sensors can be according to detection method they use such as electrical, biological, chemical, or radioactive detection.

### 3) Based on the Conversion Phenomenon

This classification is based on the input and output conversion

- **Photoelectric**: Light changes into electrical signals.
- **Thermoelectric:** Temperature difference changesinto electrical voltage.
- **Electrochemical**: Chemical reactions change into electrical signals.
- **Electromagnetic**: Magnetic fields changeinto electrical signals.

### 4) Based on Output Type

- **Analog Sensors:** This type of sensor produces an output signal which is usually in the form of voltage, current, or resistance, proportional to the measured quantity.
- **Digital Sensors**: this type of sensor provides discrete or digital data as output.

## 2. Types and Application of Sensor:

Sensors are used in a variety of fields, which are very essential in modern society:

Devices and sensors research is a vast field that include a wide range of industries such as healthcare, automotive, environmental monitoring, and consumer electronics. Below you will find some important areas of current research in this field:

### *2.1 Wearable Sensors*

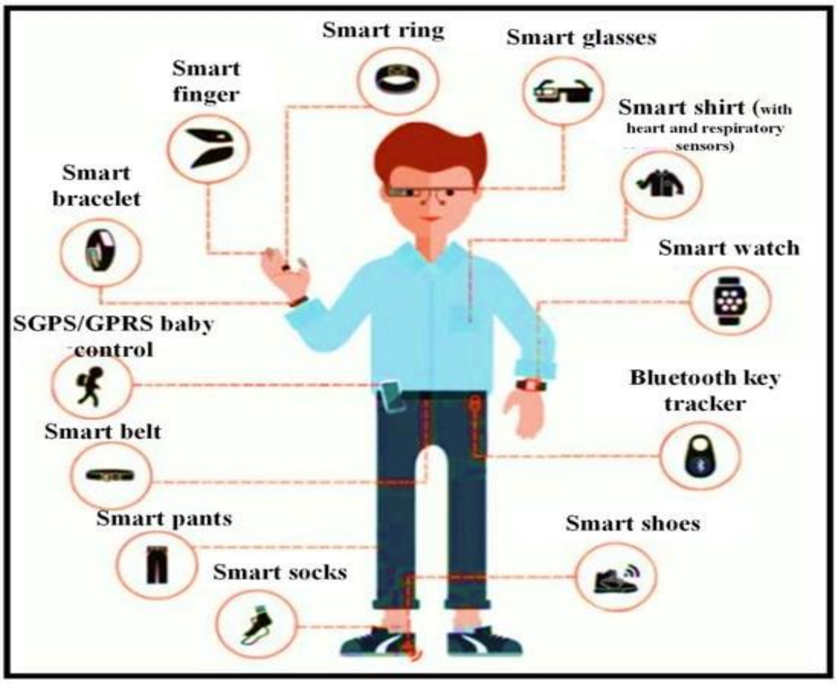

**Fig. 3: Wearable Sensors**

- **Health Monitoring**: Wearable sensors are developed to monitor vital signs, such as heart rate, blood pressure, glucose levels, and oxygen saturation. Such sensors are designed for continuous detection and can provide real-time data to users or healthcare providers.

- **Smart Clothing**: Textiles embedded in the sensor can measure variety of physiological parameters. These sensors can be integrated directly into the fabric and areexamined for sports performance tracking, injury prevention, and elderly care. Wearable sensors and biosensors convertbio-signals into electrical or optical signals, *e.g.*, physiological signals such as body temperature, heart rate, and motion that can be monitored and quantified in real-time. Wearable sensors are classified based on their monitoring mechanism such as pressure, strain, electrochemical, temperature, and optoelectrical sensors.

### *2.2 Environmental Sensors*

- **Air Quality Monitoring**: Sensors are increasingly being developed to monitor contaminants in the air, such as particulate matter (PM), nitrogen dioxide (NO2), carbon dioxide (CO2), and ozone (O3). These sensors can help to track air pollution levels in urban environments and can affect public health and policy decisions.
- **Water Quality Sensors**: Research is also going on portable sensors for water quality monitoring, detecting pollutants like heavy metals, pesticides, and bacteria.

### *2.3 Biological Sensors (Biosensors)*

- **Disease Detection**: Biosensors areused to detect specific biomarkers in connection with diseases such as cancer, diabetes, and infections. Some biosensors are designed to detect genetic material, proteins, or other molecules that indicate the presence of a disease.
- **Point-of-Care Testing**: There's a push for portable, easy-to-use biosensors for quick diagnostics in clinics, remote locations, or even at home, reducing the reliance on laboratory testing. These devices are applicable in the medical, food industry, the marine sector as they offer good sensitivity & stability as compared with the usual techniques. In recent years, these sensors have become extremely popular, and can be used in variety of areas mentioned below.

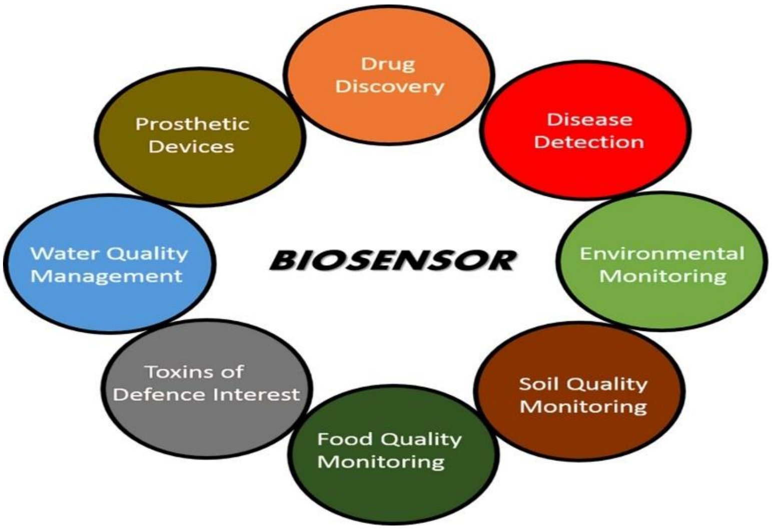

**Fig. 4: Application of Biosensors**

### *2.4 Energy Harvesting Sensors*

- **Powering Sensors**: Energy harvest research focuses on creating sensor which can power themselves with small, sustainable energy sources, such as solar, vibrations, or thermal gradients. This is especially important for remote or difficult to access applications where changing batteries would be unrealistic.

### *2.5 Advanced Detection Materials*

- **Nanomaterials**: Using nanomaterials such as graphene and carbon nanotubes improves the sensitivity, selectivity, and performance of the sensor. These materials can be ideal for applications that recognize very small changes in the environment and require higher accuracy.
- **Molecular Sensors**: Molecular sensors can be used for chemical detection and can record specific molecules in gases or liquids. This is especially useful forfood industry, drug, and environmental surveillance applications.

### *2.6 Paper Based Sensor*

Paper is a versatile, flexible, porous, and environmentally friendly substrate used in the production of inexpensive devices and biosensors for rapid detection of analytes. Paper-based sensors provide affordable platformfor food quality, environment, sunlight radiation, and pathogen detection as well as simple, accurate, and rapid detection of diseases. Paper-based devices provide cost effective technology for producing simple, portable diagnostic systems that are very useful in resource-limited environment such as in developing countries, where fully-equipped facilities and highly trained medical staff are absent.

## 3. Recent Advances in Sensor Technology:

### 1) Smart lighting sensor solution for smart cities

These intelligent lighting sensors measures ambient light (luminosity) with a new set of directed sensor probes. These intelligent Lighting devices can also monitor conditions within tunnels, building, outside in the streets and also temperature and humidity.

### 2) E-HealthSensorShield

The E-Health Sensor Shield users use nine different sensors to perform biometric and medical applications that require physical monitoring. These sensors are pulse, oxygen in blood (SPO2), airflow (breathing), body temperature, electrocardiogram (ECG), glucometer, galvanicskinresponse (GSR-sweating), blood pressure (sphygmomanometer) and patient position (accelerometer).

### 3) EncryptionLibraries–AES/RSACryptography for Sensor Network

Encryption Libraries sensor platforms in order to ensure the authentication, confidentiality (data protection) and integrity of the information collected by the sensors.

### 4) 3G connectivity to ZigBee, Wi-Fi, and Bluetooth sensors

The new multiprotocol router for wireless sensor networks with Wi-Fi, Bluetooth and ZigBee sensors connected to the Internet via 3G connections. These allow you to simultaneously send the information collected by hundreds of sensor nodes. This technology is 10 times faster than traditional GPRS gateways.

### 5) iPhone and Android Devices Detected by Smart Sensors

The sensors can also be used in detecting smartphones. Any Smartphone (iPhone, Android) in the nearby area can be detected by smart sensor technology by measuring Wifi and Bluetoothactivity.

### 6) AI-Powered Sensor Networks

The fusion of AI and sensor technology leads to an intelligent sensor network. These networks can make autonomous decisions, optimize data collection, analyze and respond without human intervention. These sensors are often made of flexible, biocompatible materials and are designed to interact with biological tissues withoutcausing symptoms or side effects. These sensors capable of autonomous decision-making, optimizing data collection, analysis, and response without human intervention.

### 7) Advanced Biocompatible Sensors

Biocompatible sensors become more demanding and seamlessly integrate into the human body for continuous health monitoring. These sensors, often made of flexible and biocompatible materials, are designed to interact with biological tissues without causing side effects.

### 8) Integration with Quantum Technology

Quantum technology is on the horizon as a transformative power for sensor technology and quantum sensors are expected to provide unprecedented accuracy and sensitivity. These sensors use quantum mechanics principles such as superposition and entanglementto measure physical quantities with superior levels of precision beyond the classical sensors. This ability provides special value for fields requiring high-precision measurements such as navigation, medical imaging, and environmental monitoring, as quantum sensors can recognize and quantify phenomena at the quantum level, provide knowledge that is previously beyond the scope.

### 9) Enhanced Accuracy and Sensitivity

Accuracy and sensitivity are game-changers for sensor technology. Through advances in materialscience, particularly nanotechnology, sensors allow us to recognize the most subtle changes in environmental or biological conditions. Nanoscale materials, known for their unique properties, improve the sensor'sability to identify small variations, leading to previous and more accurate diagnosis in healthcare.

## 4. Challenges and Considerations:

Sensors provide amazing skills, but some challenges are related to their use.

- **Accuracy and Calibration:**
    - Sensors provide accurate and reliable readings but it requires regular calibration and maintenance.
- **Power Consumption:**
    - Many sensors, especially portable or remote devices, require energy-efficiency to ensure longer use or battery life.
- **Data Security and Privacy:**
    - As sensors collect personal or sensitive information (such as location and health data) to ensure that secure transmission and storage is important to protect our privacy.
- **Environmental Factors:**
    - Sensors must be robust enough to manage a variety of ambient conditions including extremes temperatures, humidity, or exposure to hard chemicals.

## 5. Future Trends in Sensors:

The advances in technologyare the main opportunity for sensors, including:

- **Miniaturization: Microsystem Technology**

Miniaturization is very important part of modern technologies. Because a reduction of characteristic dimensions of a system usually results in shorter response times so that higher speed is achievable in signal generation and processing of that system. In most of the cases, Miniaturization reduces costs because of the high integration rate, low power consumption, and high reliability. Miniaturization is gaining importance in every field of applications such as semiconductor, automobile, aerospace, bio-medical industries. Micromachining in this technology ensures creation of micro parts without compromising the functionality.

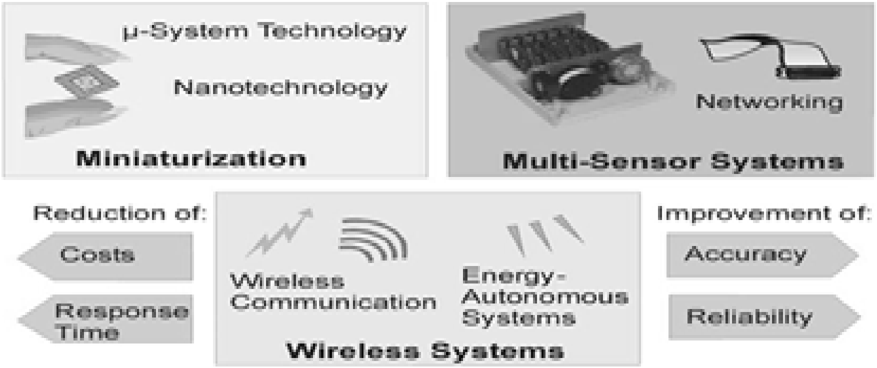

**Fig. 5: Future Trends in Sensor Technology**

- **Use of Multisensors**

The use of multi-sensor systems is becoming more important for wide range of applications, from monitoring and automation from manufacturing processes to robotics, automative applications, smart home process control, environmental engineering, biotechnology, and biological sciences. Multi-sensor systems offer the advantage of being able to achieve high levels of accuracy and reliability using economic sensors. This allows the system to manage a large amount of available information using highly developed signal processing techniques to ensure better performance.

- **Wireless Systems**

The large number of components are essential for achieving the required functions. The electric wiring of distributed systems is complex and creates problem in the system's handling process. Using wireless systems means better convenience and leads to significant cost savingsWireless sensor systems have the advantage that they can be located anywhere.

## 6. Conclusion:

Devices and sensors bridge the physical world in the digital world, enabling intelligent technologies and applications that improve efficiency, security, and convenience. Therefore, further development in technology in sensors will offer new opportunitiesfor new innovation across several industries.

## References:

[1] Jacob Fraden (2010), *Handbook of Modern Sensors Physics, Design and Application*.

[2] PranavK V R, Sarma K J. *An Overview of Various Sensors and Their Uses*.International Journal for Multidisciplinary Research (IJFMR) E-ISSN: 2582-2160.Volume 4, Issue 5, September-October 2022.

[3] Amalraj J. Jegathesh, Banumathi S., John J. Jereena.*IOT Sensors And Applications: A Survey*, International Journal of Scientific & Technology Research Volume 8, Issue 08, August 2019.

[4] Olfa Kanounand Hans-Rolf Tränkler, *Sensor Technology Advances and Future Trends*, IEEE Transactions on Instrumentation and Measurement, Vol.53, No.6, December2004.

[5] Amrita Tribhuwan Singh, Darlin Lantigua, *Paper-Based Sensors: Emerging Themes and Applications*

[6] Chaudhari, Manali & Dharavath, Srinu. *Study of Smart Sensors and their Applications*.International Journal of Advanced Research in Computer and Communication Engineering Vol. 3, Issue 1, January 2014.

# ELECTRON RANGES FOR VARIOUS HUMAN BODY SECTIONS USING THE CONTINUOUS SLOWING DOWN APPROXIMATION (CSDA): ANALYSIS

**Sandeep Gupta**
Department of Physics,
Punjabi University College, Ghudda (Bathinda) Punjab.
Corresponding author E-mail: sandeep.gupta253@gmail.com

## Abstract:

This paper presents continuous slowing down approximation ranges (CSDA) for electrons of human body parts like the brain and bone in the energy region of 30-1000 keV using an empirical formula. CSDA is important for applications like radiation biology, electron beam lithography, and chemical analyses of surface regions of a solid. The formula for the (CSDA) range is dependent on factors such as the effective atomic number, density, and total energy of the various human body parts. For electrons with energies between 30 and 1000 keV, the computed CSDA range findings are found to be reasonably consistent with the values provided by the ESTAR [1] program.

**Keywords:** CSDA Range, Effective Atomic Number, ESTAR Program.

## 1. Introduction:

Osman and associates [2] in various water equivalent polymer gel dosimeters, the stopping power, CSDA range, and radiation yield calculations of electrons and positrons spanning the 20 eV–1 GeV energy range were carried out. Sugiyama's effective charge notion was taken into consideration for electron and positron collision stopping power estimates. Here, the target material's effective charge (Z*) and effective mean excitation energy (I*) were computed in addition to the effective charge of incident electrons and positrons (z*). The Fano model was chosen to adjust for the density effect. An analytical model based on the ratio of the collision to the radiative stopping power, as defined by Attix, was taken into consideration for the radiative stopping power. The continuous slowing down approximation (CSDA) was taken into consideration for the CSDA range and radiation yield, and numerical integral methods were used for the computations. The target material was chosen to be MAGIC and MAGAS polymer gels due to their water equivalent and 3D dosage distribution characteristics. All of the equations discussed in this paper were programmed as computational codes in order to carry out the computations. The ESTAR program and PENELOPE Monte Carlo modeling were used to compare the stopping power, range, and radiation yield data. There were several differences between the calculated and reference data in the low and high energy regions. Nonetheless, there is a striking resemblance between the reference and calculated data. For energies >1 keV, a good agreement between the calculated and reference data was found for the collision stopping power and CSDA range. However, for energies more than 100 keV, a good agreement was found for the radiative stopping power.

Based on structure feature analysis of the existing optical energy loss functions for certain organic compounds, Tan *et al.* [3] conducted an empirical method to produce optical energy loss functions that are provided for a large number of organic compounds for which optical data are not accessible. This approach yields optical energy loss functions that correspond well with the experimental results. In a variety of domains, including the structure study of solid and plasma-first wall interactions in nuclear-fusion reactors and the implantation of impurity atoms in the production of semiconductor devices, the stopping power, or the average energy loss per unit path length, is crucial.

The Bethe theory for the energy loss of fast charged particles colliding with atomic targets is expanded to explicitly include the situation where the projectile possesses bound electrons, according to research by Trujillo *et al.* [4]. The theory is distinguished by considering the ionizations and excitations of the projectile and target (but not the exchange of charges). The electronic stopping cross section Se is divided into contributions originating from the electronic structure of the projectile and the target as a result of the Coulombic nature of the interaction between the two. The electronic structure of the projectile contributes significantly to Se in the lower portion of the velocity area where this theory is valid, by an order of 10–20%. However, this contribution diminishes at high projectile velocities, leaving only the conventional Bethe term. The adiabatic Bohr criteria along with the Thomas-Fermi model of the atom is used to determine the number of electrons bonded to the projectile, N1, as a function of the projectile's velocity. Using the Bethe approximation, we derive an analytical equation for the total stopping cross section and compare the experimental and computational results of He, Li, and B ions on C and Al targets.

The electron range is defined by T. E. Everhart *et al.* [5] as a measurement of the electrons' straight-line penetration distance in a material. When traveling through a solid, electrons with energy in the kilo-electron volt range collide with the material's electrons and scatter inelastically. The literature contains successful contributions that are based on research of the CSDA range and stopping power of electrons in various absorber types. [6] Tahir *et al.* Dielectric models have been used to calculate the stopping power (SP) and inelastic mean free path (IMFP) of three polymers: polymethyl methacrylate (PMMA), polyethylene (PE), and polyvinyl chloride (PVC) with electron energies ranging from 200 eV to 50 keV.

The primary input used to calculate the SP and IMFP for the dielectric models is the energy loss function (ELF). In this study, ELF was calculated using a quantitative analysis of reflection electron energy loss spectroscopy (REELS) spectra that had already been published.

With rising electron energies up to 50 keV, the IMFP rises and the SP of PMMA, PE, and PVC falls. SP is reduced by 10–15% in this study, according to comparative data from the National Institute of Standards and Technology (NIST) database for electron energies between 10 and 50 keV. Complete tables with CSDA ranges for numerous samples ranging from 10 KeV to 103 MeV were published by Berger and Seltzer [7]. For several applications in radiation dosimetry, surface layer analysis, and nuclear spectroscopy, the basic formula for the stopping power of electrons in various absorbers is frequently required.

Positron stopping power (SP) values for a few human body tissues were presented by Hasan Gumus {8}. These values were applicable for low and intermediate positron energies. Furthermore, the range from the stopping power of the continuous slowing down approximation (CSDA) is calculated. Adipose tissue, skeletal muscle, skin, and soft tissue have all had their CSDA ranges calculated for incident positron energy in the 20 eV to 10 MeV range. Using a modified Rohrlich and Carlson calculation of stopping power, the range of positron has been computed within the continuous slowing down approximation. For some materials, including adipose tissue, skeletal muscle, skin, and soft tissue, the computed results of the SP and CSDA range values for positrons in the energy range of 20 eV to 100 MeV are found to be in good agreement with the Penelop 2014 code findings above 0.4 keV energies. It produces more significant results for energies below 0.4 keV than Penhole 2014. A model for calculating the SP and CSDA ranges for incident positrons on certain human body tissues is proposed in this work. For intermediate energies, straightforward analytical formulae for the effective number of positrons, effective mean excitation energy (EMEE), and positron SP have been developed. The findings of this investigation into the ability of specific human body tissues to halt low energy positrons should be helpful for nuclear radiation therapy, PET, and diagnostics.

D. Emfietzoglou *et al.* [9] extended the MC code [10,11] to the transport of electrons in liquid water over a broad range of impact energies down to roughly a few eVs and investigated the computations of inelastic mean-free-paths and collision stopping-powers for low energy electrons less than 10 keV in liquid water. Tufan *et al.* [12] used the continuous slowing down approximation (CSDA) to determine the route length of incident particles in the target after calculating stopping power for electrons and positrons in a few biological compounds spanning the energy range of 100 eV to 1 GeV. Sugiyama's model was extended to low and high energy areas by Hasan Gumus *et al.* [13] in order to calculate the stopping powers for non-relativistic heavy ions in different target materials.

A second order polynomial approximation with two parameters was used by Agrawal *et al.* [14] to fit a relation for continuous slowing down approximation (CSDA) ranges for electrons and positrons of carbon, aluminium, and copper in terms of energy from 700 keV to 50000 keV. The absorber's atomic weight (A) and atomic number (Z) determine these characteristics. The polynomial potential function has been determined to provide a superior fit to the available experimental data.

A novel computation of the stopping powers (SP) and inelastic mean free pathways (IMFP) for electrons in toluene at energies lower than 10 keV was published by Tan *et al.* [15]. The dielectric model and an empirical assessment method of the optical energy loss function (OELF) serve as the foundation for the computation. Numerous hydrocarbons assessed OELFs have had their dependability thoroughly examined using accessible experimental optical data. The computed SP at 10 keV is also compared with the Bethe−Bloch prediction, and the evaluated mean ionization potential for toluene is compared with that provided by Bragg's rule using the empirical OELF. For ten elemental solids (Al, Si, Cr, Ni, Cu, Ge, Pd, Ag, Pt, and Au), S. Tanuma *et al.* [16] computed electron stopping power in the energy range of 100 eV to 30 keV. Their results were found to be satisfactory in comparison to the results produced by the non-relativistic Bethe SP equation and Joy and Luo's empirical modification of the Bethe equation. The stopping power and inelastic mean free pathways for 20 eV to 20 keV electrons in a group of ten significant scintillators were recently calculated systematically by Zhenyu Tan *et al.* [17]. The dielectric model, which incorporates the Born-Ochkur exchange correction and optical energy loss functions (OELFs), serves as the foundation for the computations. A relation for continuous slowing down approximation (CSDA) ranges for electrons of materials like water, fat, muscles, and bones in terms of energy from 30 keV to 1000 keV was published by Hemlata Singh *et al.* [18].

The stopping powers and ranges for electrons produced by the ESTAR Program [1] are identical to those compiled for 72 materials at a standard grid of 81 kinetic energies between 10 keV and 106 keV in International Commission on Radiation Units and Measurements (ICRU) Report 37 [19]. Similar tables can be computed using ESTAR for any other element, compound, or mixture. Additionally, determine stopping powers for any kinetic energy range from 1 keV to 10 GeV. In this study, we describe a technique for determining the CSDA ranges for electrons in the brain and bones at energies between 30 and 1000 keV. Results obtained by this method are compared with CSDA range values obtained through ESTAR program and are found to be in close agreement.

## 2. Theory and Computational method:

The study by Parcerisa [20] A highly conformal dose can be delivered to the tumor using particle treatment, an advanced kind of cancer radiation that significantly spares healthy tissue. The goal of this effort is to increase the precision of ion chamber dosimetry for carbon ion beam particle therapy. Numerous correction factors, some of which are only partially understood, influence the readout of air-filled ionization chambers. The stopping power ratio between water and air, or sw, is one of the beam quality correction parameters that is the subject of this study. In order to ascertain the water-to-air stopping power ratio in monoenergetic carbon ion beams, we first designed and executed experimental investigations. The findings of those measurements were then extended to realistic treatment beams using the Monte Carlo code FLUKA, and a model was created to determine sw,air for any given position in a treatment field. In order to investigate its potential use in absolute dosimetry and patient plan verification, we lastly tested the generated model in patient situations. The acquired results are encouraging and can lower the uncertainty margins in the calculation of the absorbed dose for carbon ion beam radiation if they are included in the suggested dosimetry protocols.

Ghossain [21] investigated the interaction between electrons and matter; using the Bethe-Bloch formula theory as provided in the reference, determined the stopping power (in MeV $cm^2/g$), and the range will be computed. This has been done for a variety of target materials, including water, bone, muscle, and tissue, as well as various electron energies. The results of these calculations, which were completed using the programs STAR and Matlab, will be displayed for stopping power versus energy and range versus energy. The stopping power of electrons in a few biological substances was determined over the energy range of $10^{-2}$ MeV to $10^3$ MeV. The target materials' electronic (collisional) and radiative stopping powers were added up to determine the total stopping power. The path length (Range) was then determined using the continuous slowing down approximation (CSDA). Bethe calculated the electron's energy loss per unit length, which can be expressed as follows:

$$(dE/dx)_r = (e^2/4\pi\epsilon_o)2\ [N_oZ^2\rho\ (T + mc^2)/137\ m^2c^4A]\ [4\ln 2(T + mc^2)/mc^2 – 1.33]$$

Where T is kinetic energy of electron and ρ is density of the material.

For low atomic number targets and biological molecules, Akar *et al.* [22] provided an inelastic mean free path formula, an energy straggling parameter formula, and a continuous slowing down approximation-range (CSDA-range) derived from the stopping power. However, it holds true for both high and low electron energies. Andnet Nigussie Habte [23] provides an empirical relationship for the alpha particle's stopping power.

$$\left(\frac{-dE}{\rho dx}\right) = \frac{\gamma^2 Z^2}{A} aE^{-b} Z^{C\log E+d} \text{ ---------- (1)}$$

Where a=918, b=0.82, c = 0.145 and d = 0.635. Also, ρ denotes density, A as atomic weight and Z as atomic number of the stopping material, while E is the kinetic energy of the α particle in MeV/amu and $\gamma^2$ =1 give good result for elements like Al, Cu, Ge, Ag, Cd, and Te from alpha particle energies 4 MeV - 15 MeV.

The indistinguishability of incident and atomic electrons was noted by Mozumder *et al.* [24]. Conventionally, the more energetic of the two emergent electrons is referred to as the primary when discussing an ionization brought on by an incident electron. Therefore, half of the incident energy is the maximum energy loss (ignoring atomic binding). The stopping number of an electron, when this effect is taken into account, is determined by a complex formula that uses a different configuration of the parameters found in the stopping number of heavy charged particles;

$B_e = [\ln mc^2\beta^2E/2I^2(1 - \beta^2) - (2(1 - \beta^2)^{0.5} - 1 + \beta^2]$

$\mathrm{Ln}2 + (1 - \beta^2) + 0.125(1 - ((1 - \beta^2)^{0.5})^{0.5} - 2\,C/Z - \delta]$

Hasan Gumus *et al.* [25] introduced a new algorithm for the stopping power calculation in the case of incoming positrons for low and intermediate energy positrons below 10 keV for certain materials, such as silicon, copper, aluminium, and liquid water. They also modified the Rohrlich and Carlson [26] stopping power formula. An empirical formula for the CSDA range was published by Gupta *et al.* [27], and an empirical equation has been constructed utilizing the empirical relation for the total stopping power of electrons for the CSDA range of monoenergetic electrons in the energy region 0.2- to 10-MeV. For the CSDA range, the equivalent empirical equation is

$$R(T_0) = \frac{mc^2}{SZ + 1.3230}\left[\frac{\gamma^{az+b-1}}{az+b-1} + \frac{1}{\gamma}\right]_{1.1957}^{\gamma} \quad \text{------ (2)}$$

This formula is valid only for stopping materials of atomic numbers from 1 to 92 but it is not valid in low energy region.

Hemlata Singh *et al.* [18] *et al.* presented a simple empirical relation for CSDA ranges of electrons in the energy regions 30 to 1000 keV for substances such as bones, muscles, fat and water is R = A + B X, where A and B are constants. The value of $X = \left(\frac{D}{Z}\right)E^{1.5}$ which depends on density (D), effective atomic number (Z) and energy (E). They demonstrated an inaccuracy of up to 16.38% between the predicted values for the CSDA range of electrons and the standard values provided by Berger and Seltzer [7].

According to Habeb *et al.* [28], the Bethe theory is combined with the mass collision stopping power for heavy charged particles in soft and hard collisions, such as electrons and positrons. For a light charged particle with mass m and velocity v, the collision stopping power is determined by:

$S = k[\ \ln(\tau^2(\tau+2)/2(I/m_oc^2)^2) + F^+(\tau) - \delta\text{-}2c/z]$,

Where F+ is a dimensionless function, Z is projectile charge in units of electric charge, I is mean excitation energy τ is kinetic energy in terms of rest mass and C/Z is the shell correction.

Tan *et al.* [29] have presented a simple empirical relation for CSDA ranges for electrons with energies between 25 to 200 keV by the following relation,

$$R_0 = 1.90 \times 10^{-6}\left(\frac{A}{Z}\right)^{2.5} E^{1.6}\,\mathrm{gm/cm^2}$$

The CSDA Range data of Berger and Seltzer [30] served as the basis for the aforementioned relationship. where the symbols for atomic weight, atomic number, and energy are A, Z, and E, respectively. However, for $70 < Z < 92$, the errors are within 2% to 5%, and for $30 < Z < 70$, they are within 10%. The relation's drawback is that it only applies to a relatively narrow range of energies and provides no guidance for atoms with lower atomic numbers. In this study, we provide an empirical formula to determine the electron's CSDA range.

$$R = 333\times10^{-8}X - 488\times10^{-14}X^2 - 48\times10^{-5} \text{ --------- (3)}$$

Where $X = \left(\frac{Z}{A}\right)^{-1.75} E^{1.6}$ which depends upon Effective atomic number (Z), Mass number (A) and Energy (E).

Recently he Continuous Slowing Down Approximation Ranges (CSDA) of electrons in human body parts, such as blood and the eye lens, in the energy range of 30 1000 keV were recently determined empirically by Sandeep Gupta [31]. Applications such as radiation biology, electron beam lithography, and chemical studies of a solid's surface regions depend on continuous slowing down approximation ranges (CSDA). The overall energy, density, and effective atomic number of the different body sections are some of the variables that affect the formula for the (CSDA) range. It is found that the numbers given by the ESTAR [1] program coincide accurately with the CSDA range calculations for electrons in the 30-1000 keV energy range. A visual depiction of the CSDA range in relation to energy values has also been included.

## 3. Results and Discussion:

Using equation (3), we determine the electrons' CSDA range values. Table 1 displays the assessed values and CSDA range values for energy levels ranging from 30 keV to 1000 keV that were acquired using the ESTAR program for human body parts such as the brain and bones. We can see from this table that the two numbers are rather close to one another. According to table 1, the maximum percentage error between our computed CSDA range values and the ESTAR program's CSDA range values in the brain and bone is 4.245152 and 3.036649, respectively and for Table 2 logarithm analysis is 0.394222 and 0.4447. The ESTAR program's provided data closely matches the values of the CSDA ranges assessed using our empirical connection.

Figure 1-2 shows that the CSDA range consistently rises with electron energy and that our computed values and the ESTAR program's CSDA range values accord well. Additionally, fig. 3 illustrates how the percentage error varies with electron energy.

**Table 1: Values of CSDA ranges for electrons of Brain and Bone**

| Energy (KeV) | ESTAR Values of Brain | Our Calculated Value of Brain | % error (Brain) | ESTAR Values of Bone | Our Calculated Value of Bone | % error (Bone) |
|---|---|---|---|---|---|---|
| 30 | 0.001752 | 0.001678 | 4.245152 | 0.00191 | 0.001852 | 3.036649 |
| 40 | 0.002912 | 0.002937 | -0.85619 | 0.003167 | 0.003213 | -1.45248 |
| 50 | 0.00431 | 0.0044 | -2.08593 | 0.004681 | 0.004794 | -2.41401 |
| 60 | 0.005927 | 0.006048 | -2.04244 | 0.006431 | 0.006575 | -2.23915 |
| 70 | 0.007746 | 0.007867 | -1.56634 | 0.008397 | 0.00854 | -1.70299 |
| 80 | 0.009754 | 0.009846 | -0.94797 | 0.01056 | 0.010678 | -1.11742 |
| 90 | 0.01194 | 0.011976 | -0.30243 | 0.01292 | 0.012979 | -0.45666 |
| 100 | 0.01428 | 0.014248 | 0.222087 | 0.01545 | 0.015432 | 0.116505 |
| 150 | 0.02812 | 0.027528 | 2.104347 | 0.03037 | 0.029765 | 1.992097 |
| 200 | 0.04481 | 0.043572 | 2.76235 | 0.04831 | 0.047061 | 2.585386 |
| 250 | 0.06363 | 0.061929 | 2.673247 | 0.06855 | 0.066823 | 2.519329 |
| 300 | 0.08409 | 0.082245 | 2.19393 | 0.09052 | 0.088659 | 2.055899 |
| 350 | 0.1058 | 0.10422 | 1.492956 | 0.1139 | 0.112232 | 1.464442 |
| 400 | 0.1286 | 0.127588 | 0.78714 | 0.1384 | 0.137242 | 0.836705 |
| 450 | 0.1522 | 0.152101 | 0.064849 | 0.1637 | 0.163413 | 0.175321 |
| 500 | 0.1764 | 0.17753 | -0.64079 | 0.1898 | 0.190484 | -0.36038 |
| 1000 | 0.4368 | 0.436422 | 0.086637 | 0.4711 | 0.45838 | 2.700064 |

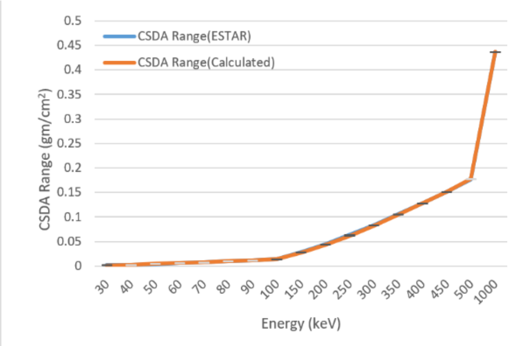

**Fig. 1: Variation of CSDA Range with electron energy (keV) for Brain**

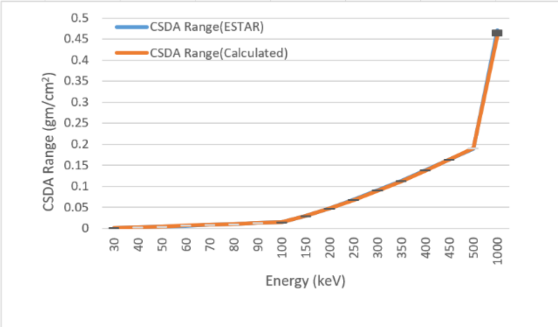

**Fig. 2: Variation of CSDA Range with with electron energy (keV) for Bone**

**Table-2 Values of CSDA ranges for electrons of Brain and Bone in logarithm scale**

| Energy (KeV) | ESTAR Values of Brain in log | Our Calculated Value of Brain in log | % error (Brain) | ESTAR Values of Bone in log | Our Calculated Value of Bone in log | % error (Bone) |
|---|---|---|---|---|---|---|
| 30 | -2.75647 | -2.77521 | -0.67986 | -2.71897 | -2.73236 | -0.49247 |
| 40 | -2.53581 | -2.5321 | 0.146304 | -2.49935 | -2.49309 | 0.250465 |
| 50 | -2.36552 | -2.35655 | 0.379198 | -2.32966 | -2.3193 | 0.4447 |
| 60 | -2.22717 | -2.21839 | 0.394222 | -2.19172 | -2.1821 | 0.438925 |
| 70 | -2.11092 | -2.10419 | 0.318818 | -2.07588 | -2.06854 | 0.353585 |
| 80 | -2.01082 | -2.00674 | 0.202902 | 1.97634 | -1.97151 | 0.244391 |
| 90 | -1.923 | -1.92169 | 0.068123 | -1.88874 | -1.88676 | 0.104832 |
| 100 | -1.84527 | -1.84625 | -0.05311 | -1.81107 | -1.81158 | -0.02816 |
| 150 | -1.55098 | -1.56023 | -0.5964 | -1.51756 | -1.52629 | -0.57527 |
| 200 | -1.34863 | -1.36079 | -0.90166 | -1.31596 | -1.32734 | -0.86477 |
| 250 | -1.19634 | -1.20811 | -0.98383 | -1.16399 | -1.17507 | -0.9519 |
| 300 | -1.07526 | -1.08489 | -0.8956 | -1.04326 | -1.05228 | -0.8646 |
| 350 | -0.97551 | -0.98205 | -0.67042 | -0.94348 | -0.94988 | -0.67834 |
| 400 | -0.89076 | -0.89419 | -0.38506 | -0.85886 | -0.86251 | -0.42498 |
| 450 | -0.81759 | -0.81787 | -0.03425 | -0.78595 | -0.78671 | -0.0967 |
| 500 | -0.7535 | -0.75073 | 0.367618 | -0.7217 | -0.72014 | 0.216156 |
| 1000 | -0.35972 | -0.36009 | -0.10286 | -0.32689 | -0.33877 | -3.63425 |

Figure 4-5 shows that the CSDA range in logarithm scale consistently rises with electron energy and that our computed values and the ESTAR program's CSDA range values accord well. Additionally, fig. 6 illustrates how the percentage error in logarithm scale varies with electron energy.

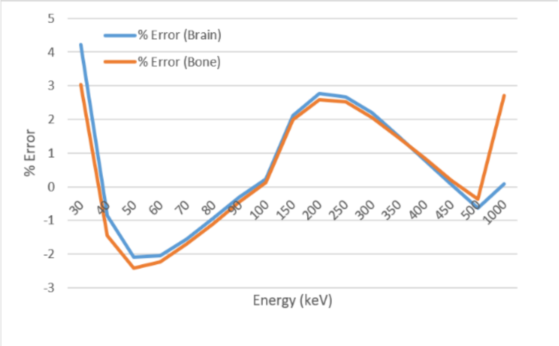

**Fig. 3: Variation of % error of CSDA Range with electron energy (keV)**

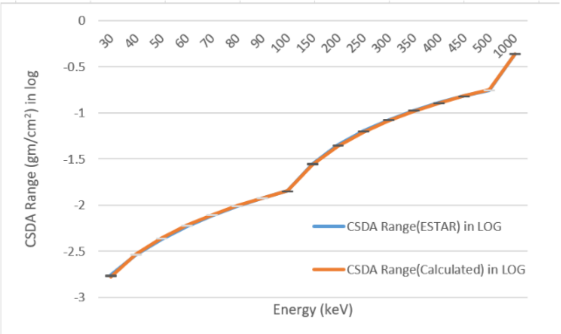

**Fig. 4: Variation of CSDA Range with electron energy (keV) for Brain on logarithmic scale**

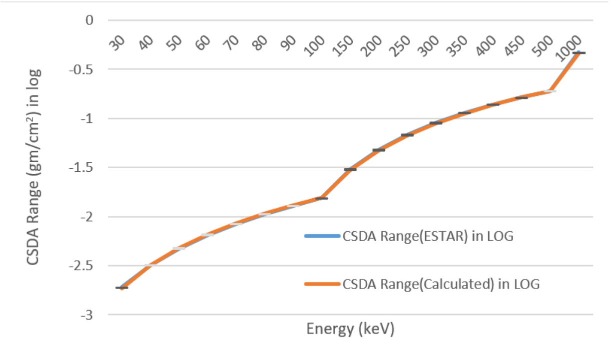

**Fig. 5: Variation of CSDA Range with electron energy (keV) for Bone on logarithmic scale**

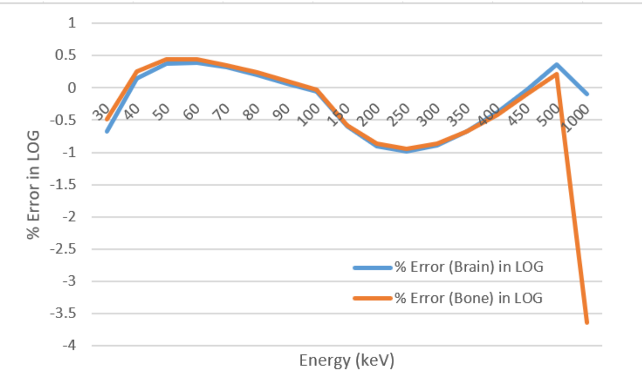

**Fig. 6: Variation of % error of CSDA Range with electron energy (keV) on logarithmic scale**

## 4. Conclusion:

It is clear from the current study that the CSDA ranges of materials may be stated in terms of the material's mass number, atomic number, and electron incident energy. Notably, the suggested empirical relationship is more straightforward, broadly applicable, and the results produced are more consistent with the information found in the literature.

## References:

[1] M. J. Berger, J. S. Coursey, M. A. Zucker and J. Chang, *Available online as:* 2005 http://physics.nist.gov/Star, NIST, Gaithersburg, MD.

[2] Osman H. and Gumus H." Stopping power and CSDA range calculations of electrons and positrons over the 20 eV–1 GeV energy range in some water equivalent polymer gel dosimeters," Applied radiation and Isotopes, Vol. 179, January 2022.

[3] Tan P., Xia Y., Zhao M., Liu X. Li F., Huang B. and Ji Y., 2004 "Electron stopping power and mean free path in organic compounds over the energy range of 20–10,000 eV," Nuclear Instruments and Methods in physics research section B: Beam Interaction with Materials and Atoms, vol. 222, Issue 1-2, Pages 27-43.

[4] Trujillo C.R., Cruz A.S., Oddershede J. and Sabin R.J." Bethe theory of stopping incorporating electronic excitations of partially stripped projectiles," Phys. Rev.A, Vol. 59, 4850, 1999. DOI: https://doi.org/10.1103/PhysRevA.55.2864.

[5] T. E. Everhart and P. H. Hoff, 1971"Determination of Kilovolt Electron Energy Dissipation vs Penetration Distance in Solid Materials," J. Appl. Phys. 42, 5837.

[6] Tahir D., Suarga, Sari N.H. and Yulianti, 2015" Stopping powers and inelastic mean free path of 200 eV–50 keV electrons in polymer PMMA, PE, and PVC," Applied Radiation and Isotopes, Vol. 95, Pages 59-62. https://doi.org/10.1016/j.apradiso.2014.10.001Get rights and content.

[7] Berger M. J. and Seltzer S. M., 1982 "Tables of energy losses and ranges of electron and positron, NASA SP-3012.

[8] Gumus H.," Positron CSDA range and stopping power calculations in some human body tissues by using Lenz Jensen atomic screening function," radiation Physics and Chemistry, Vol. 196, July 2022, https://doi.org/10.1016/j.radphyschem.2022.110092Get rights and content

[9] D. Emfietzoglou, and M. Moscovitch, 2002"Inelastic collision characteristics of electrons in liquid water," NIMB. 193, 71–78.

[10] D. Emfietzoglou, G. Papamichael, M. Moscovitch, J. Phys.D 33 (2000) 932.

[11] D. Emfietzoglou, G. Papamichael, K. Kostarelos, M. Moscovitch, Phys. Med. Biol. 45 (2000) 3171.

[12] Mustafa cagatay Tufan, Tuba namdar, and hasan Gumus, 2013" Stopping power and CSDA range calculations for incident electrons and positrons in breast and brain tissues," Radiation and Environmental Biophysics. 52, issue 2, pp 245-253.

[13] Hasan Gumus and Fevzi Koksal, 2002" Effective Stopping charges and stopping Power calculations for heavy Ions," Radiation Effects & Defects in Solids. Vol. 157, pp. 445–458.

[14] Agrawal P., Rathi K.S. and Verma A.S.," Continuous Slowing Down Approximation (CS and DA) Ranges of Electrons and Positrons for Carbon, Aluminum and Copper," www.isca.in 3rd April 2012.

[15] Tan Z., Xia Y., Liu X., Zhao M. and Zhang L., 2009" A new calculation on the stopping power and mean free path for low energy electrons in toluene over energy range of 20–10 000 eV," Applied Radiation and Isotopes, Vol. 67, issue 4, Pages 625-628, https://doi.org/10.1016/j.apradiso.2008.11.013Get rights and content.

[16] S. Tanuma, C.J. Powell and D.R. Penn, 2005 "Calculations of stopping powers of 100 eV to 30 keV electrons in 10 elemental solids," Surface and Interface Analysis. vol. 37, issue 11, pp. 978 – 988.

[17] Zhenyu Tan and Yueyuan Xia, 2012" Stopping power and mean free path for low-energy electrons in ten scintillators over energy range of 20–20,000 eV," Applied Radiation and Isotopes. Vol. 70, Issue 1, pp. 296-300.

[18] Hemlata Singh, S. K Rathi and A.S.Verma, 2013" Ranges of Electrons for Human Body Substances," Research Journal of chemical science, Vol. 3, issue 3, pp. 4-8.

[19] International Commission on radiation Units and Measurements (ICRU), "Stopping powers for electrons and Positrons, Report No. 37, Bethesda, MD (1984).

[20] New Parcerisa S.D." Experimental and computational investigations on the water-to-air stopping power ratio for ion chamber dosimetry in carbon ion radiotherapy," https://www.researchgate.net/publication/277731637, 22 June 2015.

[21] El-Ghossain M.O., 2017" Calculations of Stopping Power, And Range Of Electrons Interaction With Different Material And Human Body Parts," International Journal of Scientific & Technology Research Vol. 6, Issue 01, ISSN 2277-8616, pp. 114-118.

[22] Akar, Aysegul, Gumus, Hasan, Okumusoglu and T. Nazmi, 2006" Electron inelastic mean free path formula and CSDA-range calculation in biological compounds for low and intermediate energies," Applied Radiation and Isotopes. Vol. 64, Issue 5, pp. 543-550.

[23] Andnet Nigussie Habte, 2011" Thesis of Calculations of stopping power and range of α-particles of several energies in different materials. ADDIS ABABA University, Ethiopia. Page 18.

[24] Mozumder A. and Tobias C.A., 1999 "Stopping power Inradiation in Fundamental Processes involved in the interaction of radiation with matter, Science Physics Matter & Energy. The Editors of Encyclopaedia Britannica.

[25] Hasan Gumus, Onder Kabaday and M.C.Agatay Tufan, 2006" Calculation of the Stopping Power for Intermediate Energy Positrons. Chinese Journal of Physics. Vol. 44, No. 4.

[26] F. Rohrlich and B. C. Carlson, Phys. Rev. 93, 38 (1954).

[27] S.K.Gupta and D.K.Gupta, 1980"An Empirical Equation for the (CSDA) Range Difference of 0.2- to 10-MeV Electrons. Japanese J. Applied Physics, 19, 1-3.

[28] Habeb S.J., and Allah S.M.A., 2016" Estimation of the total energy loss and CSDA of positron in Carbon and silver" Tikrit Journal of Pure Science Vol. 21, ISSN: 1813-1662 (Print), E-ISSN: 2415-1726 (online).

[29] Tan D. and Heaton B., 1994" Simple empirical relations for electron CSDA range and electron energy loss", Applied Radiation and Isotopes, 45, 527-28.

[30] Berger J. and Seltzer S. M., 1964" Tables of energy-losses and ranges of electrons and positrons," In Studies in Penetration of Charged Particles in Matter, pp. 205-268. NAS-NRC Pub. 1133, Washington, DC.

[31] Gupta S.," Calculation of continuous slowing down approximation (CSDA) range of electrons interaction with parts of human body," www.ijcrt.org © 2024 IJCRT | Volume 12, Issue 4 April 2024 | ISSN: 2320-2882.

# AN OVERVIEW OF SOME SYNTHESIS METHODS FOR MATERIALS

**L. Anandaraj[1], R. Sakunthaladevi*[2] and Jitendra Pal Singh[3]**

[1]PG and Research Department of Physics,

Sacred Heart College (Autonomous), Tirupattur-635601, India.

[2]Department of Physics, Trinity College for Women, Namakkal-637002, India.

[3]Department of Physics, School of Sciences, IFTM university, Moradabad-244102, India

*Corresponding author E-mail: sakunthaladevi92@gmail.com

## Abstract:

In material science the synthesis process is very important. The material properties like crystal structure, unit cell parameters were determined by using X-ray diffraction mainly depends of the purity of the sample. In the same way the size of the material depends on the types of methods used for synthesis and growth process in the field of crystal growth. The selection of the synthesis method based of the type of elements used initially and the application of the final product. Apart from that some methods need sophisticated instruments and lab facilities but some them done in every lab easily. In proposed work discuss some commonly used synthesis methods. The process of mixing components or compounds to create new materials is known as materials synthesis. It uses both physical and chemical techniques and can produce materials with special qualities.

## 1. Introduction:

In science, matters in the universe can be broadly divided into solid, liquid and gas based on their physical nature. Solids further classified into crystalline (arrangement of atoms is periodically repeating pattern) and non-crystalline solids (irregular arrangement of atoms). On the other hand, crystalline solids can be either single or many crystals. Where the entire crystal lattice is continuous with unbroken boundary are called single crystals, or the crystal lattice discontinuous with boundaries are called poly crystals [1].

Crystals are the undervalued supports of the world of recent technology. For years, natural specimens were the only source of large, well-formed crystals. Today almost all naturally occurring crystals of interest have been synthesized and grown successfully in the research laboratory by using various techniques [2]. The field of crystal growth from the synthesised compound was an interdisciplinary area including physics, chemistry, metallurgy, electrical engineering, etc. Crystal growth was extremely wanted in the view of its recent developments in the fields of semiconductors, ultrasonic’s, polarizer’s, transducers, infrared ray (or) radiation detectors, ferrites, magnetic garnets, nonlinear optics, piezoelectric, solid state lasers, acousto-optic, photosensitive materials and crystalline thin films [3-7]. In this chapter we have done an overview of some methods to use for synthesis of different types of materials.

## 2. Synthesis of samples:

Synthesis of a pure sample is a most important footstep in materials science and solid-state chemistry research. The samples may be prepared as a single crystal, poly crystals, nano materials or a thin film. To obtain single crystals with sufficient dimension depends on the chemical composition of the solution, crystal formation from the solution, physical parameters such as temperature, pressure and environmental impacts. The most implemented methods of synthesis of single crystals are,

1. Solid-stated method
2. Hydrothermal method
3. Flux method
4. Magnetic stirrer method
5. Condensation method

Each method is controlled by several controllable and/or uncontrollable restrictions [8]. These limitations encourage the formation of single crystals in terms of phase, shape, and size.

### 2.1. Solid state method

Solid-state reaction route is the most implemented method to formulate single crystals or polycrystalline materials. The essential steps are [9]:

1. The solid reagents mixture placed in a crucible like porcelain, alumina, or platinum crucible before e mixing and grinding well.
2. A first heat treatment at 573–673 K for a few hours to remove the volatile compounds like $NH_3$, $H_2O$, $CO_2$, etc. called calcinations.
3. After the calcinations grinding one more time to the remaining mixture to regiment and diminish the size of the particles which will rise the contact area between the grains.
4. Second heat treatment by gradually increasing the temperature of remaining mixture for a few days and then slowly lower it to room temperature called pasty state.

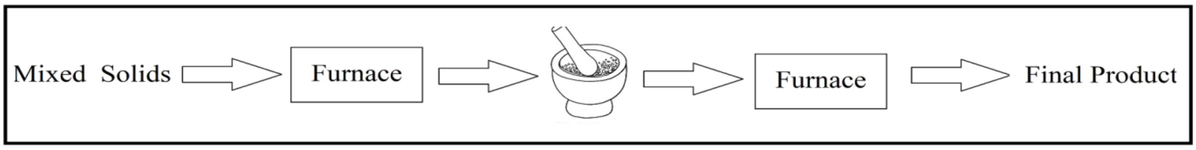

**Fig. 1: Schematic diagram of Solid State Method**

The disadvantages of this method are the reaction occurs at high temperatures (500–2000°C) for several hours to several days. The heating at these temperatures may not possible to some compounds.

### 2.2. Hydrothermal method

Hydrothermal synthesis method can be considered as a special case of chemical transport reactions and used in inorganic synthesis. In this method consists of preparing an aqueous solution containing the reagents dissolved totally or partially. The aqueous solution is transferred into a Teflon autoclave, both enclosed in metal autoclave. The preparation in the autoclave is brought to a temperature between 373-573 K continued up-to a few days. The maximum temperature is imposed by the resistance of the material instituting the Teflon[10].

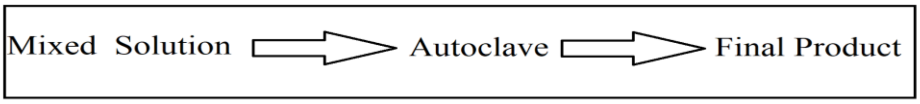

**Fig. 2. Schematic diagram of Hydrothermal Method**

The syntheses of low-temperature phases and metastable compounds can be conducted quite simply in glass or quartz glass ampoules in this method. For laboratory investigations of the hydrothermal synthesis of bulk crystal growth, plays an important role to this day.

### *2.3. Flux method*

In flux method grow materials as a single crystal and to decrease the crystallization temperature. In this growth method, the basic ingredients are reduced to a liquid form in a proper flow and the growth process starts when the solution ranges critical super saturation. The resultant super-saturation and crystal growth are reached by flow evaporation, solution cooling, or a transport process in which the solute is produced to flow from the hottest region to the coldest region [11].

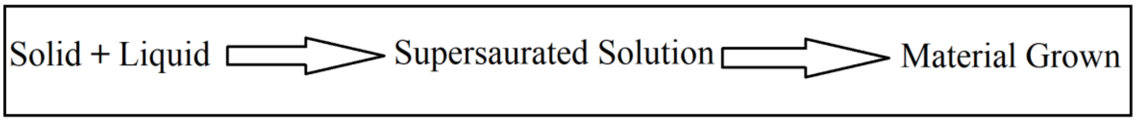

**Fig. 3: Schematic diagram of Flux Method**

In this method the solvent/solute may be a single element/ compound but the melting point of solute is generally higher than that of the solvent. One benefit of this process is that it can grow high melting phosphate crystals, arsenates, oxides, minerals, and ceramic crystals, all of which are not possible with the conventional solid-state method. If the bar magnet is placed on a revolving magnetic plate and in a beaker with the prepared solution.

### *2.4. Magnetic stirrer method*

Magnetic stirrer method keeps compensations to the reduction in organic solvents consumption, improvement in extraction efficiency during a rotating magnetic field. It is designed such that there is a separate small bar magnet and stand or plate containing the rotating magnet. If the bar magnet is placed on a revolving magnetic plate and in a beaker with the prepared solution. It creates a rotating magnetic field within the beaker and continues the process for 1 hour to 1 day up to we get a saturated solution.

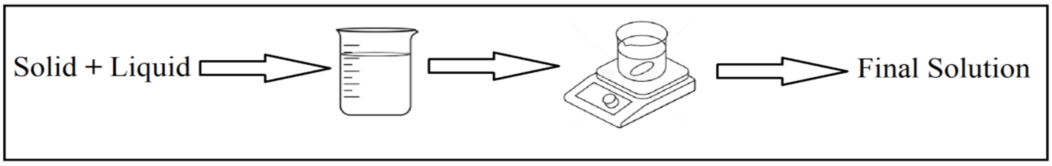

**Fig. 4: Schematic diagram of Magnetic Stirrer Method**

There are several types of magnetic stirrer available and it all depends on your selection of size, application and configuration [12]. The main use of this method simple for use and now a day's organic, inorganic and semi organic crystals are synthesized by this method.

### *2.5. Condensation method*

Liquid-Vapour mixing is of special interest in condensation method. Direct contact condensation of steam on cold water is a very efficient heat removal mechanism which often takes place at very rapid heat and mass transfer rates and may be reduced if non-condensable gases [12].There are two types, if two functional groups of the same molecule react to eliminate a simple molecule called intra-molecular condensation and two molecules of the same or different compounds called intermolecular condensation[13].

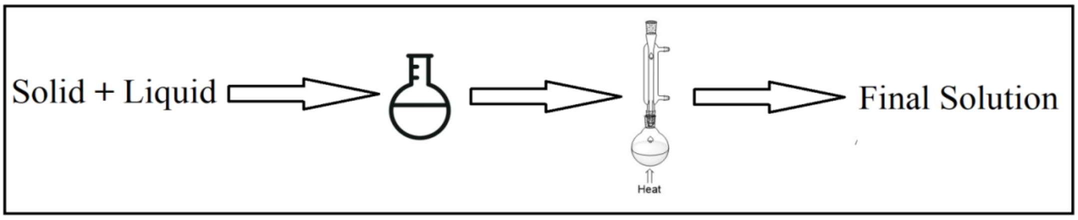

**Fig. 5: Schematic diagram of Condensation Method**

A verity of instruments is used for condensation process. Here we discuss the simplest method it contains a double walled glass tube and it have two opens for bottom and top due to water circulation. In the top part the water is entered, absorbed the heat produced during the process and leave for top open. A heating mantel is used to heat the prepared solution from $0^{O}C$ to $100^{O}C$. The advantage of this method is to synthesis an aromatic compound with simple manner [14].

### 3. Conclusion:

In materials science, synthesis is the process of mixing various components or compounds to create a new material. It is the process by which new materials are created and new methods for producing materials are developed. It is the primary source from which new solid-state chemical and physical phenomena are discovered. This often entails taking a simple molecule and turning it into something more complex through a variety of synthesis reactions. Synthesis reactions were used to create the medications you take.

### References:

[1] S. O Pillai, Solid state physics, New age international publications, London. 2018 87-147

[2] R. Ramamoorthy, V. Kanagasabai, R. Kausalya, Impact of celebrities' image on brand, International Journal of Pure and Applied Mathematics, 116, (251-253), 2017.

[3] R. N. Singh, Madhu, R. Awasthi, S. K. Tiwari, Int. J. Hydrogen energy. 34, 4693 (2009).

[4] S. D. M. Jacques, O. Leynaud, D. Strusevich, A. M. Beale, G. Sankar, C. M. Martin, P. Barnes, Angew. Chem. Int. Ed. 45, 445 (2006).

[5] W. X. Kuang, Y. N. Fan, Y. Chen, Langmuir, 16, 5205 (2000).

[6] W. Sleight, B. L. Chamberland, Inorg. Chem. 7, 1672 (1968).

[7] U. Kersen, L. Holappa, Appl. Phys. A: Mater. Sci. Process. 85, 431 (2006)

[8] Albrecht Rabenau, The Role of Hydrothermal Synthesis in Preparative Chemistry, Angewandte Chemie International Edition, England, 24, 1026-1040, (1985).

[9] Riadh Marzouki, Mahmoud A. Sayed, Mohsen Graia and Mohamed FaouziZid, Synthesis Methods and Crystallization of Cobalt Phosphates and Applications, Intechopen, (2019).

[10] Gharouel S., Smida Y.B., Ferhi M., Marin J.I., Romo L.A., Pablo K.H., Synthesis, structural, electrical and optical properties of $LiPr(PO_3)_4$, Journal of Solid State Chemistry, 289, 121459, (2020).

[11] S. Gharouel, Y.B. Smida, M. Ferhi, J.I. Marin, LA,. Romo, Synthesis, structural, electrical and optical properties of LiPr(PO3)4. Journal of Solid State Chemistry, 290, 121459 (2020).

[12] HingmireYashashri, Javalgikar Akshay, Mane Laxmi, Kale Sagar, Chikodi Prmod, Application of Magnetic Stirrer for Influencing Extraction Method on Tectona grandis as Analgesic Activity, International Journal of Pharmaceutical and Clinical Research 9(9), 634-637, (2017).

[13] L. Jothi, R. Ramesh Babu, K. Ramamurthi, Synthesis, Growth and Characterization of Organic Nonlinear Optical Single Crystals of 4-Bromo-4'-Methyl Benzylidene Aniline, Journal of Minerals and Materals Characterisation and Engineering, 2, 308-318, (2014).

[14] N. Ramya, P. Jagadeeswari, Proper coloring of regular graphs, Journal of Pure Applied Mathematics, 116, 531-533, (2017).

# SYNTHESIS, GROWTH, OPTICAL, ELECTRICAL AND MECHANICAL STUDIES OF THIRD ORDER NONLINEAR OPTICAL CRYSTAL: POTASSIUM PARA NITRO PHENOL (KPNP) SINGLE CRYSTAL

**L. Anandaraj[1], K. Venkatesan*[2], L. Jothi[3] and Jitendra Pal Singh[4]**
[1]PG and Research Department of Physics,
Sacred Heart College (Autonomous), Tirupattur-635601, India
[2]Department of Physics,
Sri Vidya Mandir Arts and Science College, Uthangarai - 636902, India
[3]Department of Physics,
NKR Government Arts College for Women, Namakkal - 637001, India
[4]Department of Physics, School of Sciences, IFTM university, Moradabad-244102, India
*Corresponding author E-mail: kvphy6@gmail.com

**Abstract:**

A potential, second order NLO optical material Potassium Para Nitro Phenol (KPNP) single crystal was grown by the slow evaporation technique. The grown semi organic NLO crystals were subjected to various studies such as single crystal XRD, UV–Visible spectrum, Fourier transform infrared spectra, photoluminescence, Second Harmonic Generation, laser damage threshold (LDT) studies, Microhardness, Z-scan and dielectric studies. The KPNP crystal belongs to triclinic system with volume 737 Å. The optical cut off wavelength of the grown crystal was found to be at 208 nm which represents the grown sample as potential material for device fabrication. The various functional group present in KPNP growm crystal was confirmed by FT-IR spectroscopic. The optical properties of grown crystal was measured by Laser Damage threshold (LDT) of Q- switched pulsed Nd:YAG laser having the wavelength 1064 nm, pulse width 6 ns and repetition rate 10 HZ system with pulse energy range 1.5 mJ. The powder second harmonic generation (SHG) analysis was carried out for powder KPNP sample using the modified Kurtz and Perry Powder technique. The SHG efficiency of KPNP crystal was found to be 5.1 times that of KDP crystal. The mechanical strength of title compound was measured by vikers microhardness method. The third order NLO properties of the material were calculated by Z-scan study. The dielectric studies were performed at different temperatures and frequencies to analyze the electrical properties. Photoconductivity results exhibit that the negative photoconductive nature of the crystal.

**Keywords:** Crystal Growth, Single and Powder Crystal XRD, UV-Vis, FT-IR, Mechanical Studies, Photoconductivity, Dielectric Measurements

## 1. Introduction:

Now-a-days researches mainly focused on NLO material with good nonlinearity due to the various extensive applications like laser technology, optoelectronic switching, telecommunication, optical computing and data storage devices. The semi organic materials having high mechanical and thermal properties but also have modest optical properties [1-5]. The molecular hyperpolarizability of semiorganic nonlinear optical crystal is used in optical switching, and electro-optic applications. Phenolic compound have zwitterionic nature which gives an improvement in nonlinear polarization. Para - nitrophenol ($C_6H_5NO_3$) is a well known zwitterionic nature containing molecular structure and promising non-linear optical material.

The s-block elements have different electronic configuration and the studies show that these elements change the property of the material by doping a small amount in the parent material. An efficient NLO material demands a specific molecular alignment of the crystal and facilitating nonlinearity in the presence of a dopant. Potassium hydroxide (KOH) doping mainly occupies the interstitial position of the Potassium Para-nitrophenol (KPNP) crystal resulting in structural grain boundaries. The NLO activity of Para - nitrophenol was increased by increasing the $K^+$ doping. In this work report the growth and analyzes of pure, 1 mol% and 2 mol% potassium hydroxide (KOH) doped Para - nitro phenol (C6H5NO3) crystal [6-8]. The main aim of this work is to analyze the influence of $K^+$ ion on the Para - nitrophenol crystal, further, the growth, structural, optical, mechanical, photoconductivity and third order nonlinear optical properties of crystals were also reported in detail.

Initially, we have tried 1 mol%, 2 mol%, 3 mol% and 4 mol% KOH doping in Para-nitrophenol; the KOH was introduced in the prepared solution. The solutions were kept for evaporation. After 18 days good quality crystals were harvested. In the case of 3 mol% and 4 mol %, the quality of the crystal was decreased. This crystal cannot be used for further physical processes [9]. 1 mol%, 2 mol % KOH doped Potassium Para-nitrophenol (KPNP) crystal have improved the NLO and physical properties. Hence, in the present experiment 1 mol%, 2 mol % KOH was chosen as dopant. For crystal growth, two separate 100 ml of 1 mol %, 2 mol % KOH doped solution were prepared and prepared solutions kept for evaporation [10]. After 18 days good quality, well structured and high transparency yellow color crystals of 1 mol% and 2 mol% KOH doped Potassium Para-nitrophenol (KPNP) crystals were harvested and the photograph of grown crystals was shown in Fig. 1.

## 2. Experimental procedure:

The crystal growth of Potassium Para-nitrophenol (KPNP) has been effort by adopting ethanol ($C_2H_50H$) as a solvent. The analytical grade Para-nitrophenol ($C_6H_5NO_3$) and potassium hydroxide (KOH) were taken in stoichiometric ratio of 2:1 and dissolved in 100 ml ethanol. The solution was completely stirred about 8 hours by using magnetic stirrer to obtain a homogenous solution after which it was filtered by using Whatmann filter paper. The resulting yellow color solution was subjected to slow evaporation and extreme care was taken while crystallization [11].

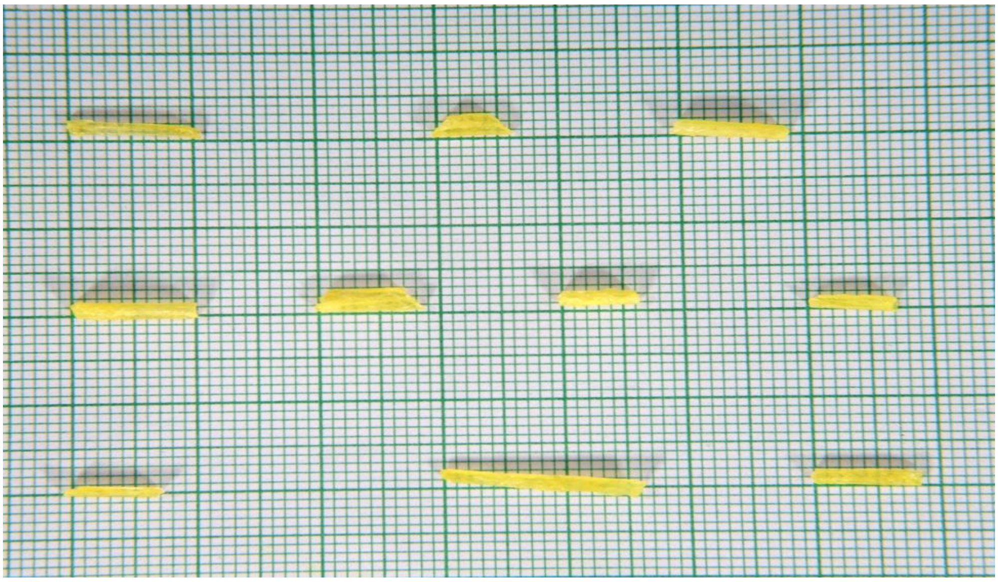

**Fig. 1: Photograph of KPNP crystal**

The purity of the synthesized crystal was further increased by successive recrystallization process. The yellow colour crystal of dimension 15 × 2 × 2 $mm^3$ was obtained after a period of 18 days.

### 3. Characterization technique:

The crystal structure of KPNP was confirmed by single crystal XRD analysis using ENRAF–NONIUS CAD4-F diffractometer. Powder XRD data were collected using RICH SIEFERT X-ray powder diffractometer using CuKα ($\lambda$ = 1.5405 Å) radiation. The optical transmittance spectra of the grown crystals were taken using Lambda 35 UV winlab spectrophotometer in the wavelength range 200 nm-1100 nm. FT-IR spectra of the samples (KBr pellets) were recorded on a SHIMADZU IRAFFINITY spectrometer. Laser Damage threshold are the salient method for quantifying withstanding capable of an optical material towards the electromagnetic radiation [12-15]. A Q- switched pulsed Nd:YAG laser having the wavelength 1064 nm, pulse width 6 ns and repetition rate 10 HZ system with pulse energy range 1.5 mJ was used to irradiate on the polished sample surface with a 15 cm focal length lens. Among the various NLO effect, the frequency doubling or second harmonic generation ability of a material can be analyzed by using the Kurtz Perry powder method. In this method the crystal has been powdered with the uniform particle size and tightly packed in a microcapillary tube of a uniform bore. The tube was mounted in the path of the Q-switched Nd: YAG laser beam emitting a wavelength of 1064 nm, with a power of 1.2 mJ. The output was collected in a monochromator with an IR blocking filter. A photomultiplier was used to detect the out coming green light and the optical signal was converted into voltage output at the cathode ray oscilloscope. The emission spectrum of a title crystal was measured at ambient temperatureby the using VARIAN

CARY ECLIPSE fluorescence spectrophotometer [16]. The emission spectrum of KPNP crystal was recorded by exciting the sample at 280 nm with xenon lamp and the emitted radiation were recorded as a function of wavelength. The mechanical strength was carried out by the microhardness test with the help of HM-2TV model tester. The third order NLO parameter was carried out by Z-scan techanique using a solid state laser of wavelength of 6328 Å. Dielectric studies for the grown crystals were carried out using an LCR meter (HIOKI 3532-50). Studies have been carried out at various frequency ranges (50Hz to 5MHz) and also at different temperatures [17].

## 4. Result and Discussion:

### *4.1 Solubility studies*

The solubility of KPNP crystal was ascertained for five different temperatures namely 30, 35, 40, 45 and 50 °C. The constant volume of saturated solution was used in this experiment. The measurement was performed dissolving KPNP crystal in ethanol and taken in airtight container and maintained at constant temperature with continuous stirring. The solution was constantly stirred for 1 hour using magnetic stirrer. The solubility of KPNP crystal as shown in Fig. 2. From the solubility studies, it could be observed that, solubility of the compound in ethanol solvent increases linearly with increases in temperature [18]. The positive solubility of the title compound shows the possibility of growing large size crystal by slow evaporation technique.

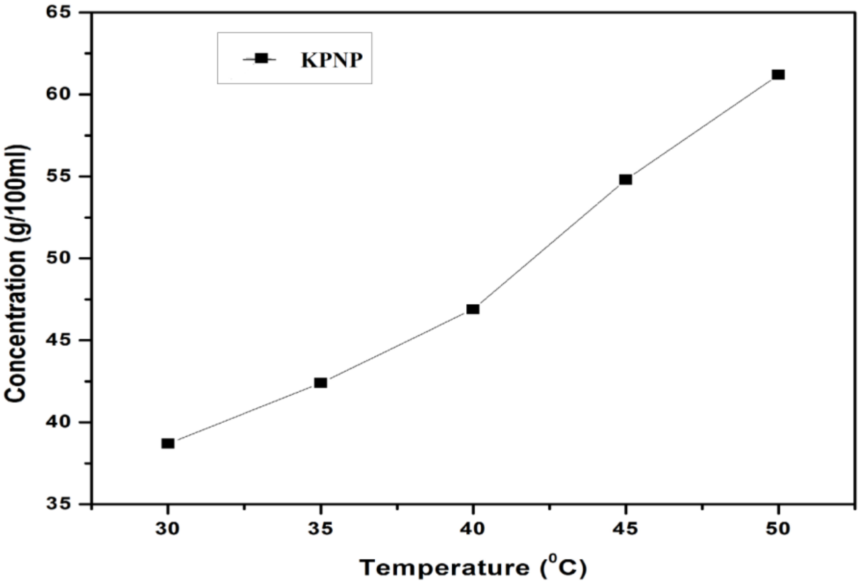

**Fig. 2: Solubility curve of KPNP crystal**

### *4.2 X-ray diffraction studies*

The powder KPNP sample was subjected to powder XRD analysis, the recorded pattern of KOH doped KPNP crystalis shown in Fig. 3. The sharp peak presence in the XRD pattern shows that the grown title crystal have good crystalline nature. The lattice parameter of KPNP crystal were estimated by single crystal X-ray diffraction [19].

Single crystal x-ray diffraction study was carried out to find the grown crystal and to determine the cell parameters and crystal structures. The single crystal data of the KPNP crystal XRD was carried out using Enraf Nonius CAD4 diffractometer with an incident Mo-Kα radiation ($\lambda$=0.71073 Å). The single crystal X-ray diffraction analysis for the grown crystal was confirmed that KPNP crystal belongs to Triclinic-P crystal system. The lattice parameters of KPNP are a = 6.44 Å, b = 9.34 Å, c =12.25 Å, α = 89.86˚, β = 76.57˚, γ = 90.60˚and the volume V = 716 Å$^3$. Table 1 shows the measured values of lattice parameters of KPNP crystal with comparisons [20-23].

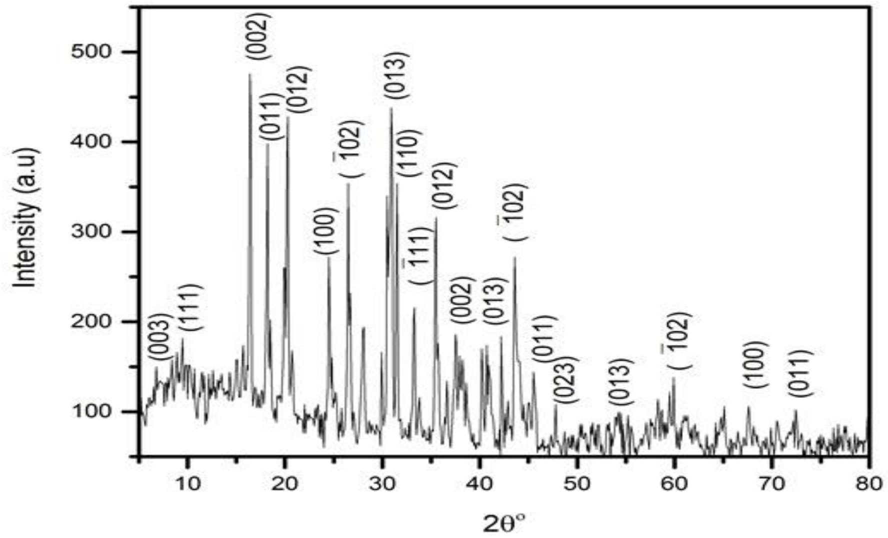

**Fig. 3: Powder crystal X-ray diffraction pattern of KPNP crystal**

**Table 1: Comparison of KOH doped KPNP crystal**

| Reference | Crystal system | Unit cell & Dimension | Cell Volume |
|---|---|---|---|
| P- nitro phenol urea **(34)** | Triclinic | a = 3.759 Å, b = 10.214 Å, c =11.788 Å, α = 98.97˚, β = 92.16˚, γ = 99.44˚ | V=440.2 Å$^3$ |
| Sodium P-nitrophenalate Para-nitrophenol Dehydrate **(35)** | Monoclinic | a = 21.171 Å, b = 8.666 Å, c =30.92 Å, α = 90˚, β = 117.79˚, γ = 90˚ | V = 714.16 Å$^3$ |
| L-Lysine 4-nitrophenolate Monohydrate **(36)** | Orthorhombic | a = 5.438 Å, b = 8.502 Å, c =12.25 Å, α = 90˚, β = 90˚, γ = 90˚ | V = 1429.67 Å$^3$ |
| Potassium Para nitrophenol (KPNP) | Triclinic | a = 6.44 Å, b = 9.34 Å, c =12.25 Å, α = 89.86˚, β = 76.57˚, γ = 90.60˚ | V = 716 Å$^3$ |

### *4.3 UV-Visible analysis*

The UV-Vis spectrum furnishes limited guidance about the structure of the ions because the absorption of UV and visible lights involve electronic transition in the σ and π orbital from the ground state to higher level energy states [24]. The optical transmittance take part an key role in clarify the potential of the NLO materials. The optical absorption spectrum of grown KPNP crystal as shown in Fig. 4 (a).

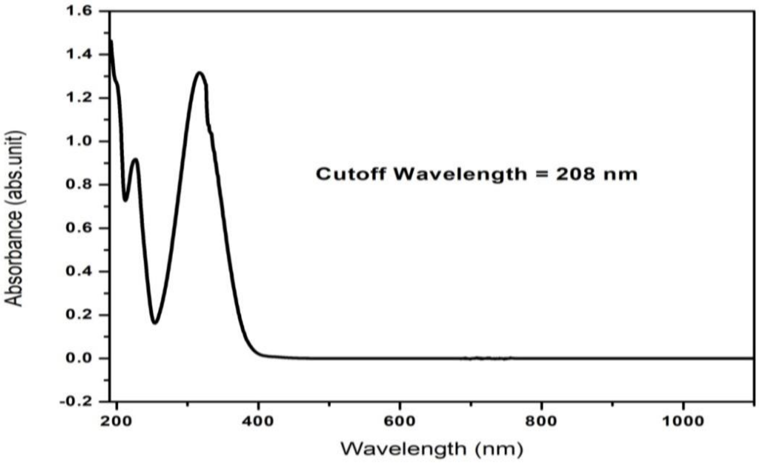

**Fig. 4 (a): UV – Vis Spectrum of grown KPNP crystal**

The UV – Visible absorption studies of grown crystal was recorded from 200 nm to 1100 nm using Lambda 35 UV winlab spectrometer. The optical cut off wavelength of the grown crystal was found to be at 208 nm which represents the grown sample as potential material for device fabrication. The spectrum reveals strong absorption band assign to $\pi$ - $\pi^*$and weak band of n - $\pi^*$ transition occurring the grown KPNP crystal [25-26]. The strong and acute absorption bands at 208 nm and 225 nm are allocate to the $\pi$ - $\pi^*$transition. The weak absorption band at 260 nm is allot to the symmetry forbidden n - $\pi^*$transition. Optical band gap was determined by plotting a graph between $(\alpha h\nu)^2$ versus energy of photon ($h\nu$) as shown in fig.4 (b). The band gap energy of the material is estimated as 3.20 eV using Tauc's plot and its reveals that the grown KPNP crystal as in the category of insulating material [27].

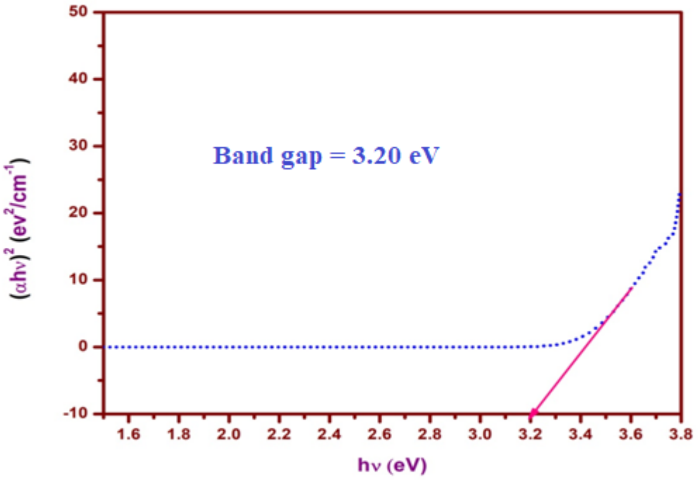

**Fig. 4 (b): $(\alpha h\nu)^2$ versus Energy of Photon ($h\nu$) of KPNP crystal**

The optical absorption coefficient ($\alpha$) was calculated by using the transmittance (T) and thickness (d) values of the crystal using the following relation,

$$\alpha = \frac{2.303}{d}\log\left(\frac{1}{T}\right)$$

Owing to the direct band gap of the KPNP crystal, absorption coefficient (α) obeying the relation for high photon energies (hυ) is given by

$(\alpha h\nu)^n$= A $(E_g - h\nu)$

Where $E_g$ is optical band gap of the crystal and A is a constant. By extrapolating the linear portion of the curve near the start of absorption edge, the optical band gap energy of the crystal was found to be 3.20eV [28]. As a consequence of this wide band gap, the grown KPNP crystal is expected to have high damage threshold and large transmittance in the visible region.

### *4.4 FTIR Analysis*

The Infrared spectroscopy is powerful tool to recognise the proton transfer activity and conform the various functional group present in organic and inorganic compounds. The FT-IR spectrum of KPNP grown crystal is illustrated in Fig. 5. The FTIR spectrum of KPNP crystal was recorded in the region of 4000 $cm^{-1}$ to 400 $cm^{-1}$ by using KBr sampling method. The FTIR spectrum is cleaved into two parts. The first part represents in the range between 4000 V $cm^{-1}$ t0 1500 $cm^{-1}$ which represents the functional group region and another part is in the region between 1500 $cm^{-1}$ to 500 $cm^{-1}$ which represents the finger print region [29-31].

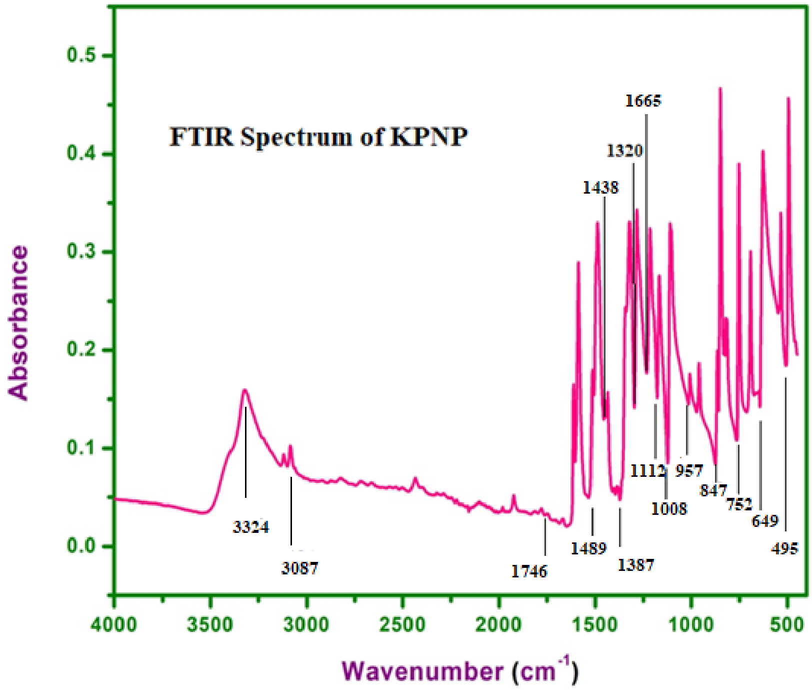

**Fig. 5: FTIR spectrum of KPNP crystal**

The band observed at 3324 $cm^{-1}$ is due to the OH stretching vibration. The vibration at 3087 $cm^{-1}$ represents to C-H vibration. The absorption band at 1746 $cm^{-1}$corresponds to C=O asymmetric stretching vibration of COOH group. The band come into view 1489 $cm^{-1}$ represents N-H stretching of vibration. The band 1437 $cm^{-1}$ deputed C-C stretching vibration. The band noticed at 1387 $cm^{-1}$ shows $COO^-$ symmetric stretching vibration COO- symmetric stretching vibration. The band discovered at 1320 $cm^{-1}$ shows that OH in plane of vibration. The band observed at 1165 $cm^{-1}$ shows HOC bending vibration, 1112 $cm^{-1}$ is CH in plane bending vibration, 1008 $cm^{-1}$ is out of plane bending vibration, 957 $cm^{-1}$ represents the OH out of plane bending vibration. 847 $cm^{-1}$ is CH vibration, 752 $cm^{-1}$ shows the $COO^{-}$ -in plane bending vibration, 649 $cm^{-1}$ is the CC in plane bending vibration and the band 495 $cm^{-1}$ shows C=O vibration.

### *4.5 Laser damage threshold analysis*

For the mechanical application point of view, Laser Damage threshold are the salient method for quantifying withstanding capable of an optical material towards the electromagnetic radiation [32]. A Q- switched pulsed Nd:YAG laser having the wavelength 1064 nm, pulse width 6 ns and repetition rate 10 HZ system with pulse energy range 1.5 mJ was used to calculate the laser damage threshold of KPNP grown NLO single crystal. The sample was placed at the focus of a biconvex lens of focal length 15 cm.

The surfaces laser damage threshold of the crystal was calculated using the formula,

$P_d = E/Ꚍ\pi r^2$

Where, E is the input energy (mJ), Ꚍ is the pulse width (ns), and r is the radius of the spot (mm). The laser beam with variety of energy was discharge on the crystal surface, the damage was observed on the crystal surface at the energy 126 mJ. The measured laser damage threshold value is 1.68 $GW/cm^3$. From the calculation of laser damage threshold studies, it is achieved that the KPNP grown crystal is best acceptable for optical and electronic application [33].

### *4.6 Powder SHG studies*

The second harmonic generations (SHG) of KPNP crystals was investigated through the modified Kurtz and Perry Powder technique. This powder SHG method acts a vital role for fast preliminary screening of noncentrosymmetric structures. For the purpose of nonlinear optics, this technique also gives qualitative measure of the second harmonic efficiency [34-37].

Nonlinear polarisation of light in a homogeneous field, moderate electric field generates a material's nonlinear optical properties. In this way, the amount of bonds in a solid-state material, specifically hydrogen bonding, can have a significant impact on NLO properties [38]. When intense light interacts with non-absorbing substances, several NLO events can occur, resulting in the production of new beams with dissimilar wavelengths. The SHG can only be detected in noncentrosymmetric crystalline structure, as confirmed by the emission of green light. A Q-Switched Nd:YAG laser beam of wave length 1064 nm with an input energy of 0.7015 Joules and pulse width of 6 ns with a repetition rate of 10 Hz was made to fall on the KPNP crystal [39]. The output from the sample was passed over a monochrometer, which separates 532 nm (SHG) signal from 1064 nm. The SHG is confirmed by the emission of green radiation from the sample. The output power was measured to be 45.6 mJ. For the same input, potassium dihydrogen orthophosphate (KDP) emitted the green light with the output energy of 8.91 mJ.

The SHG efficiency of KPNP crystal was found to be 5.1 times that of KDP crystal [40-43]. The SHG efficiency are compared with P- nitro phenol urea, Sodium P-nitrophenalate Para-nitrophenol dehydrate and L-Lysine 4-nitrophenolate monohydrate are given in Table 2.

**Table 2: Compression of SHG efficiency with reference**

| Parameter | SHG efficiency (Reference with KDP) | Reference |
|---|---|---|
| P- nitro phenol urea | 3.5 times | (34) |
| SodiumP-nitrophenalate<br>Para-nitrophenol dehydrate | 5 times | (35) |
| L-Lysine<br>4-nitrophenolate monohydrate | 4.45 times | (36) |
| Potassium Para nitrophenol (KPNP) | 5.1 times | Present work |

### *4.7 Photoluminescence studies*

Photoluminescence study is a non – destructive instrument to find the luminescence behaviour of the crystalline sample. The ions with multiple conjugated double bonds having maximum of degree of resonance steadfastness shows the fluorescence effect. The photoluminescence analysis of the grown crystals of KPNP was carried out at room temperature using a Perkin Elmerls 45 Luminescence Spectrofluorimeter between the ranges from 450 nm to 600 nm. The PL spectrum of KPNP grown crystal is shown in Fig. 6. The broad peak at 531 nm was observational in the emission spectrum [44]. This shows that KPNP crystal have a green emission under the excitation. The charge transformation and protonation of charge is extremely eloquent with second order NLO activity, where the crystal discharge green light for the photon absorption. This emission designates there may be the presence of intrinsic defects in the forbidden region. This PL emission of KPNP crystal may be the existence of electron contributing group NH and electron withdrawing group KOH, which can create the mobility of σ electrons [45].

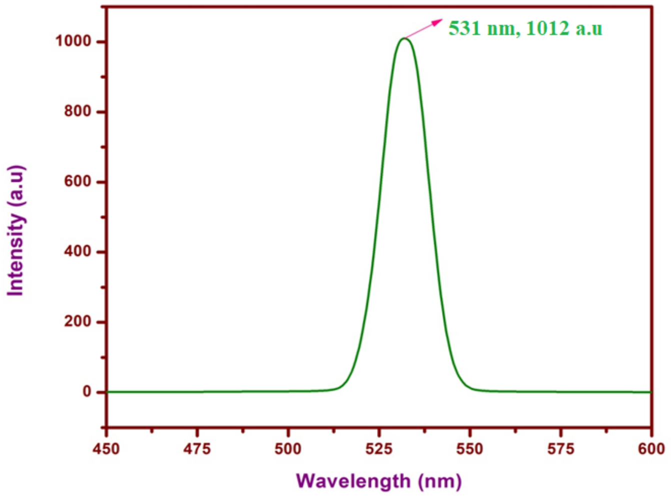

**Fig. 6: Photoluminescence spectrum of KPNP crystal**

The analysis of spectrum gives a strong emission peak of 531 nm with the corresponding intensity 1012 a.u which confirms that the grown crystal emits green radiation. The Emission of ion lies in green region that corresponds to $\sigma - \sigma^{*}$transition.

### *4.8 Mechanical studies*

In a crystalline material all the mechanical behaviour is highly influenced by its chemical composition and structure. Since, mechanical properties of a material played major role in device fabrication, properties of materials like fracture behaviour, brittleness index, yield strength and temperature of cracking can be determined by micro hardness testing method. In general, hardness is a measure of resistance offered by the material to local deformation [46].

Among different types of hardness test methods available, Vicker's hardness technique is the most suitable method employed for testing hardness property of electroplated thin layers and brittle materials having tendency for fracture, proportional to volume of loaded material [47]. Hardness is one of the mechanical properties to determine the plastic nature, fracture behaviour, molecular bindings and yield strength of the material. The hardness of KPNP was measured by LEITZ WETZLAR instrument attached with Vicker's hardness pyramidal indenter to an incident light microscope [48].

The Vicker's hardness number ($H_v$) of grown crystal was calculated using the following relation

$$H_v = 1.8554\left(\frac{P}{d^2}\right)(\mathrm{kg/mm^2})$$

Where $H_v$ is the Vicker's hardness number in $\mathrm{Kg/mm^2}$, P is the applied load in Kg, and d is the average diagonal length of the indented impression in mm. Vikers microhardness tester used to access the mechanical quality of the grown crystal for various applied loads. Fig. 7 shows the variation of $H_v$ as the function of load varying from 10 g to 100 g on the KPNP grown crystal [49].

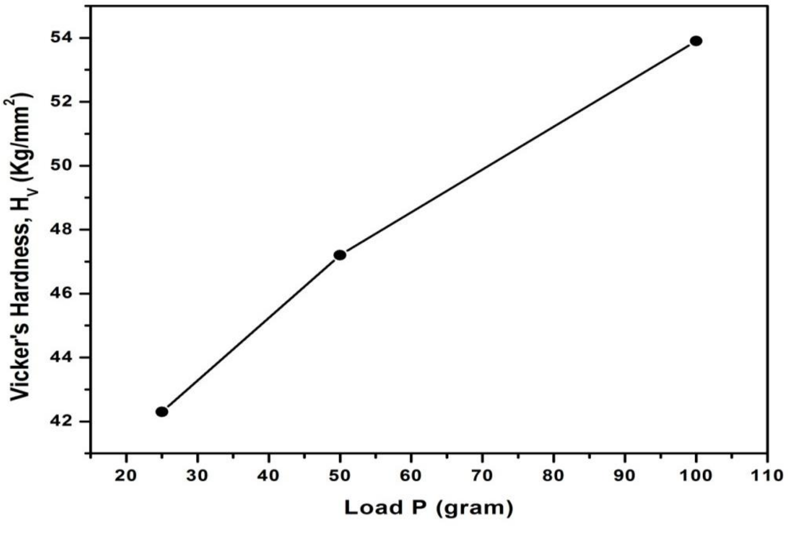

**Fig. 7: Plot of Vickers's Hardness Number versus load P of KPNP crystal**

A more suitable graph is being plotted between hardness number ($H_v$) and applied load (P) in fig. 7. It is very clear from the figure that $H_\upsilon$ increase with the increase of load. The relation between the load and size of the indentation is given by Meyer's law, P= ad$^n$. Where, 'n' is the Meyer index or Work hardening coefficient and 'a' is the constant for a given material [50].

The plot of log d against log P shown in Fig. 8 is a straight line which is in good supported with Mayer's law. The slope of the graph gives 'n' and it is determined to be 1.89. According to Onitsch and Hanneman 'n' should lie between 1.0 and 1.6 for hard material and above 1.6 for soft one. Hence KPNP crystal categorized to the soft material [51].

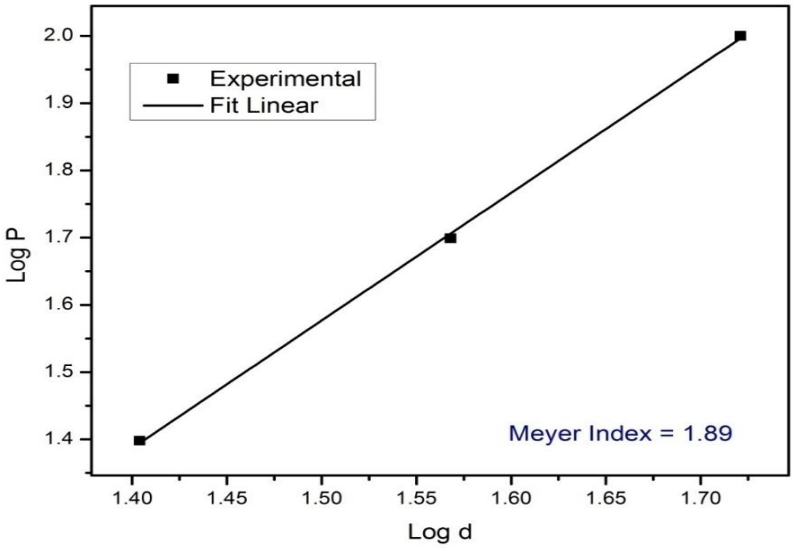

**Fig. 8: Plot of log P versus log d of KPNP crystal**

***4.9 Z-scan studies***

To enumerate the nonlinear refractive index ($n_2$), nonlinear absorption coefficient (β), and nonlinear susceptibility (χ3) for grown KPNP single crystals, Z scan technique was used. The analysis of NLO behaviour in bulk materials, the Z-scan experiment were carry out using continuous wave Nd: YAG laser beam (λ= 1064 nm) as an excitation source and it was focalized using a lens with focal length of about 34.3 mm. A photo-detector through aperture possessed focused laser beam transmitted through the sample and measured its intensity with the help of a digital power meter [52].

The plot of closed aperture setup and open aperture set up of KPNP as shown inFig. 9 (a) and Fig. 9 (b). The measurable quantity $\Delta T_{p-v}$, is the difference between the peak transmittance and valley transmittance values, $T_p$-$T_v$and is a function of $|\Delta\phi|$ is given by

$$\Delta T_{p-v=0.406\ (1-S)^{0.25}\ |\Delta\phi|}$$

Where Δφ is the on-axis phase shift and S is the linear aperture transmittance and it is given by

$$S = 1 - exp[\frac{-2r_a^2}{\omega_a^2}]$$

Where $r_a$ is the radius of aperture and $\omega_a$ is the beam radius at the aperture. The on axis phase shift ($\Delta\phi$) is related to the third order nonlinear refractive index ($n_2$),

$$n_2 = \frac{\Delta\phi}{kI_0L_{eff}}$$

Where $k = 2\pi/\lambda$, $\lambda$ is the wavelength of laser beam used,

$\alpha$ is the linear absorption coefficient,

L is the thickness of the specimen,

$I_0$ is the on-axis irradiance at focus (4.38 $KW/cm^2$)

$L_{eff} = [1 - \exp(-\alpha L)]/\alpha$, is the effective thickness of the specimen,

$$L_{eff} = \frac{1 - e^{(-\alpha L)}}{\alpha}$$

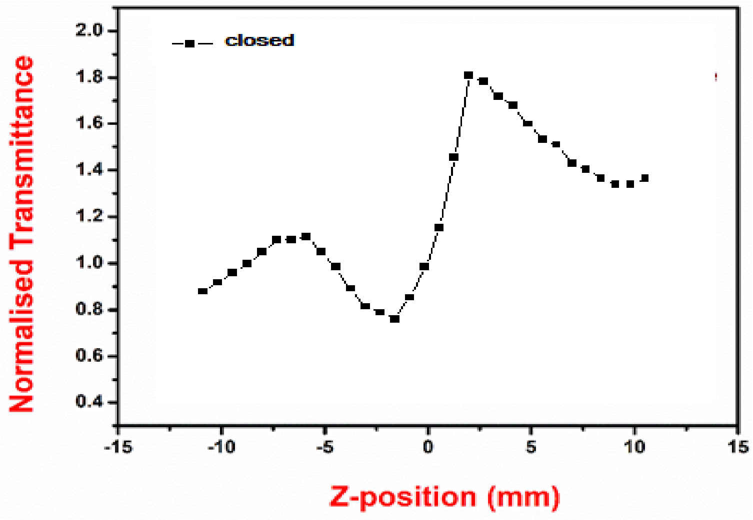

**Fig. 9 (a): Closed aperture Z-scan plot of KPNP crystal.**

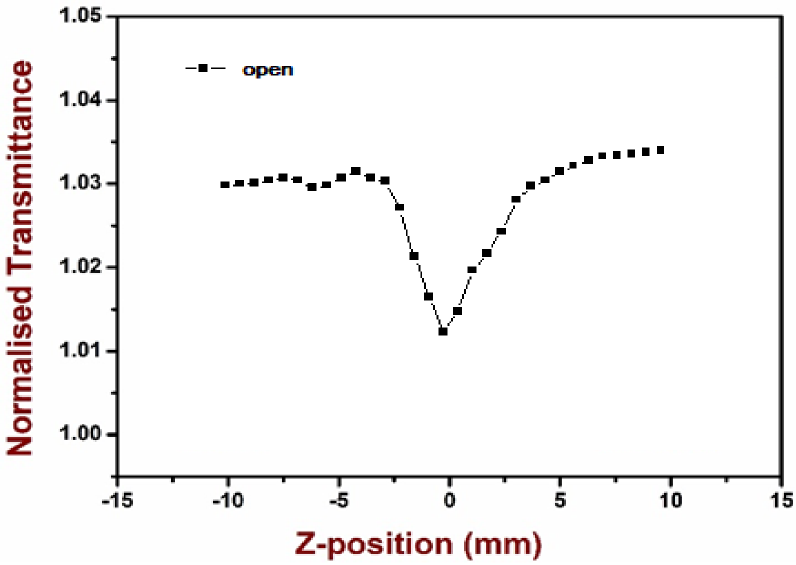

**Fig. 9 (b): Open aperture Z-scan plot of KPNP crystal.**

Fig. 9 (b), shows the Z-scan data related to open aperture arrangement (S=1) of the crystalline sample. The higher transmittance value at focus exhibited the saturated behaviour of absorption at higher values of intensity [53]. In closed aperture Z-scan arrangement, due to the saturation behaviour of the sample, the peak increased and the valley decreased, as a result symmetry nature of Z-scan curve got changed around Z=0 [54].

From Open aperture Z-scan set up, the nonlinear absorption coefficient can be determined as,

$$\beta = \frac{2\sqrt{2}\,\Delta T}{I_0 L_{eff}} \text{ cm/W}^{-1}$$

Herein $\Delta T$ is one valley value at the open aperture Z-scan plot. The real and imaginary parts of the third order nonlinear optical susceptibility could be determined from the experimental calculation of $n_2$ and β according to the following relations,

$$Re\chi^{(3)}(esu) = 10^{-4}\,\frac{(\varepsilon_o C^2 n_o^2 n^2)}{\pi}\left(\frac{cm}{W}\right)$$

$$Im\chi^{(3)}(esu) = 10^{-2}\,\frac{(\varepsilon_o C^2 n_o^2 \lambda\beta)}{4\pi^2}\left(\frac{cm}{W}\right)$$

The absolute value of $\chi^{(3)}$ was calculated from the following relation.

$$\left|\chi^{(3)}\right| = [(Re\chi^{(3)})^2 + (Im\chi^{(3)})^2]^{\frac{1}{2}}$$

**Table 3: Third order nonlinear properties of KPNP crystal**

Laser beam wavelength (λ) = 632 nm

Laser power output (P) = 34.3 mw

Lens focal length (f) = 3.5 cm

Optical path distance (Z) = 70 cm

Beam waist ($\omega_o$) = 15.35 µm

Radius of the laser beam ($\omega_L$) = 0.16 mm

Spot size diameter in front of the aperture ($\omega_a$) =15 mm

Aperture radius ( $r_a$) = 2 mm

Effective thickness ($L_{eff}$) =0.56 mm

Diffraction length (Zo) =1.48 mm

Incident intensity at the focus (Z=0) = 4.38 KW/cm$^2$

Nonlinear refractive index ($n_2$) = 1.320x10$^{-4}$*cm$^2$/W*

Nonlinear absorption coefficient (β) = 0.1400x10$^{-4}$*cm/ W*

Third-order nonlinear susceptibility (χ(3)) = 1.62x10$^{-12}$*esu*

The calculated nonlinear refractive index ($n_2$), nonlinear absorption coefficient (β) and third order susceptibility ($\chi^{(3)}$) values of KPNP single crystal are 1.320x10$^{-4}$*cm$^2$/W* and 0.1400x10$^{-4}$*cm/ W* and 1.62x10$^{-12}$ esu respectively. The value of the nonlinear refractive index indicates the self-defocusing nature of the compound which clearly shows the title compound exhibit negative nonlinear optical properties. The nonlinear absorption exhibited by the specimen could be attributed to its saturation absorption process and this could make the title compound useful for optical limiting applications [55]. The third order nonlinear properties of KPNP crystal are provided in the Table. 3.

### *4.10 Dielectric studies*

The dielectric attributes of the material are basic to know the cross section elements and transport marvels in the crystal. It additionally gives the data about the polarization component, nature of ions, particles and bonding in the material. The dielectric estimations at various frequencies are called scattering [56]. The dielectric scattering of the example was estimated for the applied frequency that shifts from 20 Hz to 1 MHz at various temperatures (313, 333, 353 and 373 K). Fig. 10 (a) and (b) shows the plot of dielectric scattering, dielectric LOSS (tan δ) versus applied frequency for various temperatures of KPNP crystal. It is seen that the scattering and tan δ values are found to diminish with the expansion in frequency at all temperatures. The high dispersion at low frequency might be because of event of all polarizations and its low worth at advantaged frequencies might be because of the critical loss of all polarizations [57]. The second-rate value of dielectric scattering is a suitable boundary for the increase of SHG efficiency. The variety of scattering with temperature is accredited to the electronic and ionic polarizations, presence of pollutions and the crystal imperfections. The experiential lower values of dielectric loss at higher frequencies for the KPNP crystal suggest the developed crystal contains more modest measure of deformities with high optical greatness [58].

The ac conditioner conductivity ($\sigma_{ac}$) has been pondered for the LARP crystal from the following formula $\sigma_{ac} = \varepsilon_0 \varepsilon_r \omega \tan \delta$ where $\varepsilon_0$ is the vacuum dielectric consistent ($8.85 \times 10^{-2}$ F/m), $\varepsilon_r$ is the general dielectric consistent and ω is the precise recurrence ($\omega = 2\pi\upsilon$) of the applied field. Fig. 10 (c) shows the variety of ac conductivity with various frequencies and temperatures. It is shows that the value of ac conductivity increases with expansion in frequency [59-61]. The electronic commute of the quantity of particles in the crystal gives nearby displacement of electrons toward the applied field, which in turn brings about polarization. The slope of the plot of ac conductivity versus temperature (Fig. 10 (d)) gives the initiation energy obligatory for the conduction process of the charge transporters. The value is found to be 0.5 eV and the inferior value of activation energy inaugurates that the crystal contains fewer amount of defects. Therefore, the grown crystal is useful for various microelectronic and related second order nonlinear optical applications.

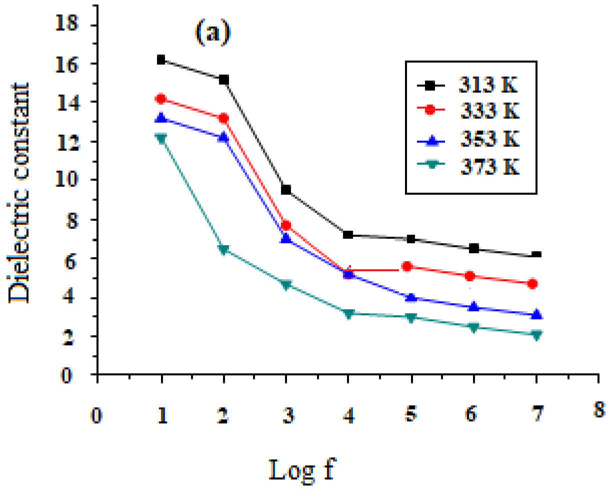

Fig. 10. (a): Variation of dielectric dispersion at various temperature

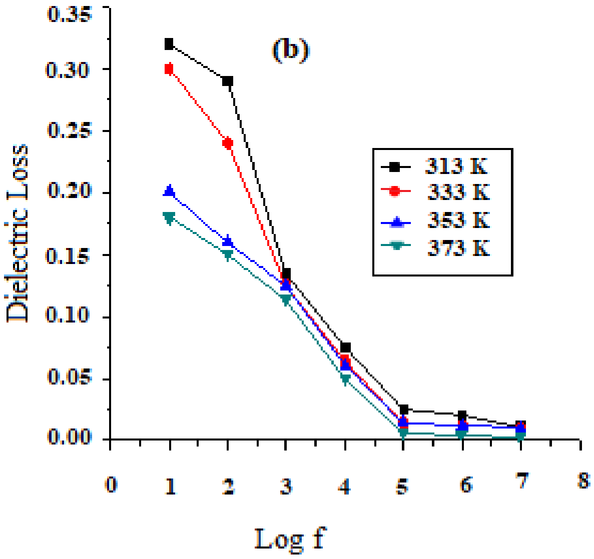

Fig. 10 (b): Variation of dielectric loss with frequency at various temperatures

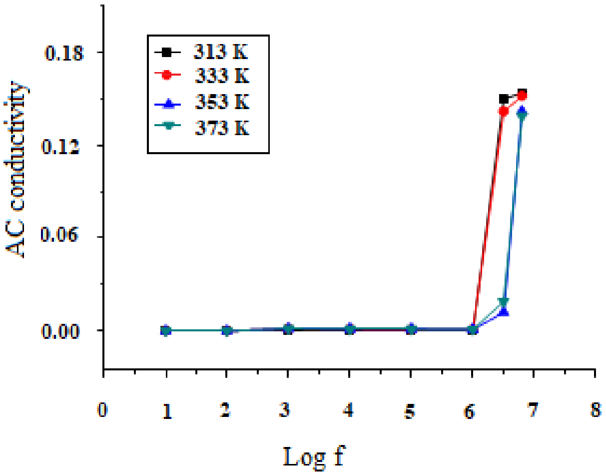

Fig. 10 (c): Variation of ac conductivity with various frequencies and temperatures.

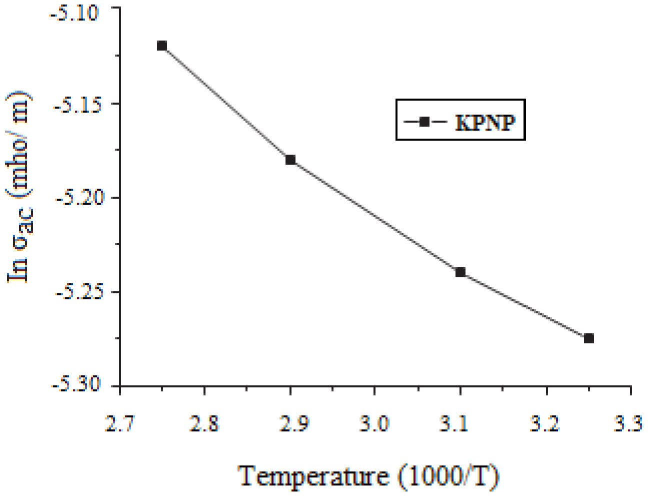

**Fig. 10 (d): Activation energy of KPNP crystal**

### *4.11 Photoconductivity studies*

In order to increase the appliance of NLO and photonic contrivance fabrications, photoconductivity measurements were made on the slash and refined sample of KPNP using KEITHLEY- 485 picoammeter in the occurrence of DC electric field [62-64]. The suitable amount of KPNP sample was set on a glass plate. Electrical contact was made on the crystal by silver tinted copper wire as electrode with an electrode distance of $0.5\times10^{-2}$ m. The sample was then joined in sequence to a DC power supply and the picoammeter. The sample was defended from all radiations then the applied field was augmented from 10 to 100 V/cm and the analogous dark current ($I_d$) in the picoammeter is recorded. The sample was subsequently elucidated with the emission from a halogen lantern lamp (100 W) to record the photocurrent ($I_p$) due to the creations of carriers by photo excitation for the similar array of applied DC power supply.

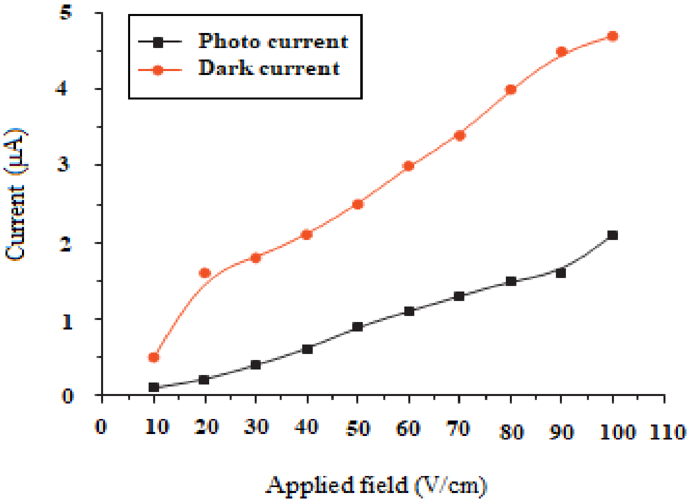

**Fig. 12: Photoconductivity behaviour of KPNP crystal**

The dark current ($I_d$) and the photo current ($I_p$) as a function of applied field is shows in Fig. 16. The dark current (Id) and the photo current ($I_p$) illustrate linear response to the applied field. It also shows that at every instantaneous, the dark current is maximum than the photo current [65]. Therefore, the above results concluded that KPNP crystal reveals unconstructive photo conductivity. This is due to the decrease in the number of charge carriers. It also describes the higher energy level is situated between the Fermi level and the conduction band. The decreases in the number of charge carriers in the incidence of radiation also due to the soaring detain cross sections for electrons and holes. This status is able to detain holes from the valence band and electrons from the conduction band, due to which the numeral of mobile charge carriers diminished and it offers negative photoconductivity in the incidence of radiation [66-67].

## 5. Conclusion:

Optically good quality single crystal of KPNP was grown successfully by the technique of slow evaporation. The structure of grown KPNP crystal is triclinic were confirmed by single crystal X-ray diffraction analysis. The lattice parameters of KPNP are a = 6.44 Å, b = 9.34 Å, c =12.25 Å, α = 89.86˚, β = 76.57˚, γ = 90.60˚and the volume V = 716 $Å^3$ were confirmed by powder X-ray diffraction pattern. The optical cut off wavelength of the grown crystal was found to be at 208 nm which represents the grown sample as potential material for device fabrication. The spectrum reveals strong absorption band assign to $\pi$ - $\pi^*$and weak band of n - $\pi^*$ transition occurring the grown KPNP crystal. The band gap energy of the material is estimated as 3.20 eV using Tauc's plot and its reveals that the grown KPNP crystal as in the category of insulating material. The vibrational frequencies of various functional groups in the crystal were confirmed by FT-IR spectrum. The measured laser damage threshold value is 1.68 $GW/cm^3$, it is achieved that the KPNP grown crystal is best acceptable for optical and electronic application. The SHG study evidently ascertained that KPNP crystal fairly shows very high competence compared to KDP counterparts. The SHG efficiency of KPNP crystal was found to be 5.1 times that of KDP crystal. The photoluminescence spectrum of analysis gives a strong emission peak of 531 nm with the corresponding intensity 1012 a.u which confirms that the grown crystal emits green radiation. The PL study also shows that Emission of ion lies in green region that corresponds to σ – $\sigma^*$ transition. The photoluminescence spectrum shows a strong green emission, which designates the high charge transfer and protonation. The hardness study shows that the KPNP crystal possesses high mechanical strength. From Z-scan the calculated nonlinear refractive index ($n_2$), nonlinear absorption coefficient (β) and third order susceptibility ($\chi^{(3)}$) values of KPNP single crystal are $1.320 \times 10^{-4} cm^2/W$ and $0.1400 \times 10^{-4} cm/W$ and $1.62 \times 10^{-12}$ esu. The dielectric study shows that the dielectric constant and dielectric loss decreases with increasing frequency with different temperature. The activation energy of title compound shows 0.5 eV shows the grown crystal is useful for various microelectronic and related second order nonlinear optical applications. The photoconductivity study confirmed that the –ve photoconductivity contributes to the absorptive nonlinearity of the grown crystal.

**References:**

[1] M. Rajkumar, M. Saravanabhavan, A. Chandramohan, Opt. Mater. 72 (2017) 247–256.

[2] K. Amudha, P.S.L. Mageshwari, R.M. Kumar, P.R. Umarani, Mater. Lett. 223 (2018): 33–36.

[3] L. Jothi, G. Vasuki, R. Ramesh Babu, K. Ramamurthi, Optik, 125 (2014) 2017 - 2021.

[4] G. Xing, M. Jiang, Z. Shao, D. Xu, Chin. J. Lasers 14 (1987) 357–360.

[5] M.J. Rosker, P. Cunningham, M.D. Ewbank, H.O. Mary, F.R. Vachass, L.F. Warren, R. Gappinger, R. Borwick, Pure. Appl. Opt. 5 (1996) 667–680.

[6] K. Srinivasan, J. Arumugam, Opt. Mater. 30 (2007) 40–43.

[7] G. Li, L. Xue, G. Su, Z. Li, X. Zhuang, Y. He, J. Cryst. Res. Technol. 40 (2005): 867–870.

[8] W. Omar, J. Ulrich, J. Cryst. Res. Technol. 38 (2003) 34–41.

[9] R.R. Babu, R. Ramesh, R. Gopalakrishnan, K. Ramamurthi, G. Bhagavannarayana, Spectrochim. Acta A. 76 (2010) 470–475.

[10] R. Valluvan, K. Selvaraju, S. Kumararaman, Mater. Chem. Phys. 97 (2006) 81–84.

[11] T. Thaila, S. Kumararaman, Spectrochim. Acta A. 82 (2011) 20–24.

[12] B. Singh, M. Shkir, S. Alfaify, A. Kaushal, N. Nasani, I. Bdikin, H. Shoukry, I. S. Yahia, H. Algarni, J. Mol. Struct. 1119 (2016) 365–372.

[13] M. Nageshwari, C.R.T. Kumari, G. Vinitha, S. Muthu, M.L. Caroline, Phys. B Condens. Matter 541 (2018) 32–42.

[14] S. Javidi, M.E. Nia, N. Aliakbari, F. Taheri, Semicond. Phys. Quantum Electron. Optoelectron. 11 (2008) 342–344.

[15] P.Y. Liao, J.G. Duh, S.R. Sheen, J. Electrochem. Soc. 152 (2005) A1695–A1700.

[16] K. Nivetha, M. Madhuri, Opt. Laser. Technol. 109 (2019) 496–503.

[17] K.S. Ramesh, M. Saravanabhavan, M. Rajkumar, D. Edison, M. Sekar, S. Muhammad, A.G. Alsehemi, Opt. Mater. 96 (2019), 109341.

[18] P. Baskaran, M. Vimalan, P. Anandan, G. Bakiyaraji, K. Kirubavathi, J. Taibah Univ. Sci. 11 (2017) 11– 17.

[19] K.V. Anand, G. Vinitha, S. Gautam, K. Chae, R. Mohan, K. Asokan, T.R. Ravindran, R. Jayavel, J. Nonlinear Opt. Phys. 27 (2018), 1850016.

[20] G. Bhagavannarayana, S. Parthiban, C. Chandrasekaran, S. Meenakshisundaram, CrystEngComm 11 (2009) 1635–1641.

[21] G. Ramasamy, G. Bhagavannarayana, S. Meenakshisundaram, CrystEngComm 14 (2012) 3813.

[22] F. Abrinaei, N. Molahasani, J. Opt. Soc. Am. B 35 (2018) 2015–2021.

[23] Z. Li, P. Zhu, Y. Chen, N. Ji, J. Liu, X. Duan, H. Jiang, CrystEngComm 21 (2019), 1570-157.

[24] G. Saravanakumar, P. Vivek, P. Murugakoothan, Spectrochim. Acta A Mol. Biomol. Spectrosc. 145: (2015) 417–424.

[25] P.V. Dhanraj, N.P. Rajesh, Mater. Chem. Phys. 115 (2009) 413–417.

[26] D. Kalaiselvi, R. Mohankumar, R. Jayavel, Mater. Lett. 62 (2008) 755–758.

[27] P. Vivek, P. Murugakoothan, Opt. Laser. Technol. 64 (2014) 1113–1119.

[28] A.T. Ravichandran, A.J. Jayarani, R. Karthick, K. Ravichandran, R. Chandramohan, Mater. Res. Bull. 20 (2015) 495–499.

[29] Y. Le Far, R. Masse, M.Z. Cherkaoui, J.F. Nicoud, Zeitschrift fur Kristallogr 210, (1995) 856–860.

[30] J. Johnson, R. Srineevasan, D. Sivavishnu, Phys. B Condens. Matter 538 (2018), 199–206.

[31] S. Mukherjee, V. Sudarsan, R.K. Vasta, A.K. Tyagi, J. Lumin. 129 (2009) 69–72.

[32] S.S. Priya, A. Alexandar, P. Surendran, A. Lakshmanan, P. Rameskumar, P. Sagayaraj, Opt. Mater. 66 (2017) 434–441.

[33] K. Nivetha, W. Madhuri, Opt. Laser. Technol. 109 (2019) 496–503.

[34] S. Selvakumar, A. Leo Rajesh, J. Mater. Sci. Mater. Electron. 27 (2016) 7509–7517.

[35] S. Selvakumar, M. Boobalan, S. Anthuvan babu, S. Ramalingam, A. Leo, Rajesh, J. Mol. Struct. 1125 (2016) 1 -11

[36] M. Mahadevan, M. Magesh, K. Ramachandran, P. Anandan, M. Arivanandhn, Y. Hayakawa, Spectrochem. Acta Part A. 0(2014) 416 – 422.

[37] G.B. Rao, P. Rajesh, P. Ramasamy, J. Cryst. Growth 440 (2016) 47–54.

[38] I.V. Kityk, B. Maruiniak, A. Mefleh, J. Phys. D Appl. Phys. 34 (2001) 1–5.

[39] S. Jeeva, S. Muthu, S.T. Selvan, M.L. Caroline, P. Purusothaman, S. Sevvanthi, G. Vinitha, G. Mani, Chin. J. Phys. 56 (2018) 1449–1466.

[40] L. Jothi, R. Ramesh Babu, K. Ramamurthi, Journal of Minerals and Materials Characterization and Engineering, 2 (2014) 308 – 318.

[41] S. Chandran, P. Rajesh, P. Ramasamy, Mater. Res. Bull. 68 (2015) 210–215.

[42] S. Chandran, R. Jagan, P. Rajesh, P. Ramasamy, J. Solid State Chem. 230 (2015), 135–142.

[43] M. Krishnakumar, S. Karthick, K. Thirupugalmani, B. Babu, G. Vinitha, Opt. Laser. Technol. 101 (2018) 91–106.

[44] P. Kanchana, A.E. Kumaran, Y. Hayakawa, C. Sekar, Spectrochim. Acta A Mol. Biomol. Spectrosc. 103 (2013) 187–192.

[45] E.M. Onitsch, U ber die Mikroharte der Metalle, Mikroscopie 2 (1947) 131–151.

[46] R.M. Wood, Laser- Induced Damage of Optical Materials, Institute of Physics Publishing, Dirac house, Bristol, UK, 2003.

[47] N. Vijayan, G. Bhagavannarayana, R.R. Babu, R. Gopalakrishnan, K.K. Maurya, P. Ramasamy, Cryst. Growth Des. 6 (2006) 1542–1546.

[48] S. Chandran, R. Paulraj, P. Ramasamy, Mater. Chem. Phys. 186 (2017) 365–371.

[49] S.M. Azhar, M. Anis, S.S. Hussaini, S. Kalainathan, M.D. Shirsat, G. Rabbani, Opt. Laser. Technol. 87 (2017) 11–16.

[50] N. Durairaj, S. Kalainathan, R. Kumar, Optik 140 (2017) 900–907.

[51] K. Nivetha, S. Kalainathan, M. Yamada, Y. Kondo, F. Hamada, Mater. Chem. Phys. 188 (2017) 131–142.

[52] P. Karuppasamy, M.S. Pandian, P. Ramasamy, S. Verma, Opt. Mater. 79 (2018), 152–171.

[53] V. Nagarajan, A.N. Ananth, S. Ramaswamy, Mater. Res. Express 4 (2017), 125102–125111.

[54] C. Amirthakumar, B. Valarmathi, I. Md Zahid, G. Vinitha, V. Seetharaman, Akilan Ramnathan, R. Mohan Kumar, Mater. Lett. 247 (2019) 25–28.

[55] D. Wang, T. Li, S. Wang, J. Wang, Z. Wang, J. Ding, W. Li, C. Shen, G. Liu, P. Huang, CrystEngComm 18 (2016) 9292–9298.

[56] P. Karuppasamy, V. Sivasubramani, M.S. Pandian, P. Ramasamy, RSC Adv. 6 (2016) 109105–109123.

[57] N. Sudharsana, B. Keerthana, R. Nagalakshmi, V. Krishnakumar, L.G. Prasad, Mater. Chem. Phys. 134 (2012) 736–746.

[58] C. Ji, T. Chen, Z. Sun, Y. Ge, W. Lin, J. Luo, Q. Shi, M. Hong, CrystEngComm 15, (2013) 2157–2162.

[59] P. Karuppasamy, M.S. Pandian, P. Ramasamy, J. Cryst. Growth 473 (2017) 39–54.

[60] A.D. Buckingham, D.A. Long, Phil.Trans.R.Soc.Lond.A 293 (1979) 239–248.

[61] K.G. Anupriya, P. Hemalatha, Mat. Sci. Res. India 15 (2018) 151–158.

[62] S.M. Risser, K.F. Ferris, Chem. Phys. Lett. 170 (1990) 349–352.

[63] A. Kumar, M.P.S. Yadav, Pramana - J. Phys. 89 (2017) 1–7.

[64] V.G. Dimitriev, G.G. Gurzadyan, D.N. Nikogosyan, Handbook of Nonlinear Optical, Crystals, Springer, Berlin, 1991.

[65] I.P. Bincy, R. Gopalakrishnan, J. Cryst. Growth 402 (2014) 22–31.

[66] S. Karthika, C. Krishnamoorthi, J. Phys. Chem. Solids 114 (2018) 133–140.

[67] K. Nivetha, S. Kalainathan, J. Phys. Chem. C 122 (2018) 4572–4582

# DIELECTRIC, MECHANICAL AND THIRD ORDER NON-LINEAR OPTICAL STUDIES ON 2-AMINO-4-METHYLPYRIDINIUM 2-CHLORO 4-NITRO BENZOATE CRYSTAL

**L. Anandaraj[1], K. Venkatesan*[2] and Jitendra Pal Singh[3]**
[1]PG and Research Department of Physics,
Sacred Heart College (Autonomous), Tirupattur-635601, India
[2]Department of Physics,
Sri Vidya Mandir Arts and Science College, Uthangarai - 636902, India
[3]Department of Physics, School of Sciences, IFTM university, Moradabad-244102, India
*Corresponding author E-mail: kvphy6@gmail.com

**Abstract:**

An organic nonlinear optical material 2-Amino-4-methylpyridinium 2-chloro 4-nitro benzoate (AMPCNB) was synthesized and large size single crystals were grown by slow evaporation solution growth method. Single crystal X-ray diffraction study showed that the title compound belongs to monoclinic crystal system with $P2_1/n$ space group. Powder XRD study was performed to ascertain its phase. The UV–VIS-NIR study was performed to investigate the transparency window and lower cutoff wavelength of the compound no absorption has been observed between 318 and 1100 nm. The third harmonic efficiency of title compound has been studied using Z-scan technique using continuous wave Nd:YAG laser to confirm its saturable absorption and self-defocusing effect. Theoretical calculation of molecular polarizability, which is helpful in device fabrication, was carried out from Penn gap, Clausius-mosotti equations and the obtained results were compared.

**Keywords**: Crystal Growth, Single Crystal XRD Z-Scan Studies, Dielectric Measurements.

## 1. Introduction:

In recent past, organic charge transfer, nonlinear optical (NLO) materials played significant role in the development of photonics due to their potential applications in communication, electro optical modulation, photo refractivity, optical storage, harmonic generation, terahertz wave generation and detection, optical switching, signal processing and laser remote sensing [1]. Organic molecules, owing to their molecular flexibility shows enhanced nonlinear optical properties in an efficient manner [2]. In general, π - electron conjugated moiety substituted by an electron donor group on one end and electron acceptor group on the other end of the conjugated structure exhibited considerable NLO activity. Under the influence of applied electric field, π - electron moiety offers desired pathway for the whole length of conjugation. Also, the donor and acceptor groups favored a special approach of proton transfer between acidic and basic organic links in various kinds of cation-anion mixtures, directing to the ground state charge asymmetry in molecules of the product, which is essential for second and third order nonlinearity [3].

In general, carboxylic acids possess ability to form expected supramolecular structure with hydrogen bonding arrangements among themselves, they grabbed considerable attention as attractive substrates for organic synthesis [4]. Pyridine molecule has been generally used in the formation of molecular building blocks in NLO materials as pyridine acts as cationic bonding site and nitrogen proceeds as proton acceptor, thus suitable as an organic base [5]. The extension of pyridine ring in NLO materials produced a notable impact in the count of π-electrons in turn produce considerable enhancement in the NLO behavior [6].

Recent investigations on pyridine and their derivatives such as 2,6-diaminopyridinium 4-nitrophenolate-4-nitro phenol (DAPNP), 2-amino-4-picolinium 4-aminobenzoate, 4-dimethylamino-N-methyl-4-stilbazolium tosylate (DAST), 2-amino-4-methylpyridinium-4-methoxy benzoate, 2-amino 5-chloropyridinium 4-carboxybutanoate, 2-amino-5-chloropyridinium-L-Tartrate and 2-amino 5-bromopyridinium-L-Tartrate have been reported to exhibit excellent nonlinear optical properties shows their significant role especially in the field of optical communications and frequency conversion applications.

In this direction, a pyridine based cation 2-amino-4-methyl pyridine (AMP) formed π-donor-acceptor molecular compound by accepting a proton ($H^+$) from 2-chloro 4-nitro benzoic acid. The formed 2-amino-4-methylpyridinium 2-chloro 4-nitro benzoate (AMPCNB) compound consists of benzoate anion and protonated 2-amino-4-methyl pyridine cation. From the information collected, in this present study, we have investigated the single crystal X-ray diffraction, powder X-ray diffraction, Optical transmittance, Z-scan, Optical limiting, photoconductivity, dielectric and mechanical properties of the title compound [7].

## 2 Experimental details:

### *2.1 Material synthesis and microanalysis*

The salt of the title compound 2-Amino-4-methylpyridinium 2-chloro 4-nitro benzoate ($C_{13}H_{12}ClN_3O_4$) was obtained by adding commercially purchased (Merck, AR grade > 99%) 2-amino 4-methyl pyridine of one mole and one mole of 2-chloro 4-nitro benzoic acid in ethanol solvent. The two solutions were mixed together and stirred for about 4 hours to get a homogeneous solution, which then turned in to a form of white colored precipitate settled at the bottom of container was separated from solution and dried at 40° C [8, 9]. Also, the synthesized material purity was enhanced by repeated recrystallization processes using ethanol as a solvent.

The reaction mechanism of 2-amino-4-methylpyridinium 2-chloro 4-nitro benzoate (AMPCNB) is shown in Fig. 1 (a). The Carbon-Hydrogen-Nitrogen (CHN) elemental composition percentage of AMPCNB crystals were determined using Vario EL III Elemental analyzer (Germany) employing helium as a carrier gas. The analyzed results were given in Table 1. From the table, it could be seen that the results obtained were in close agreement with the theoretical values, confirmed the presence of the compound..The Schematic diagram of AMPCNB single crystal as shown in Fig. 1 (b).

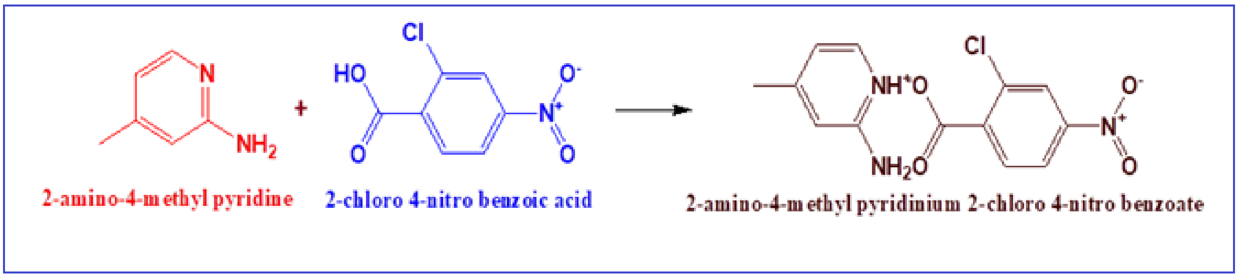

**Fig.1 (a): Reaction mechanism of AMPCNB single crystal**

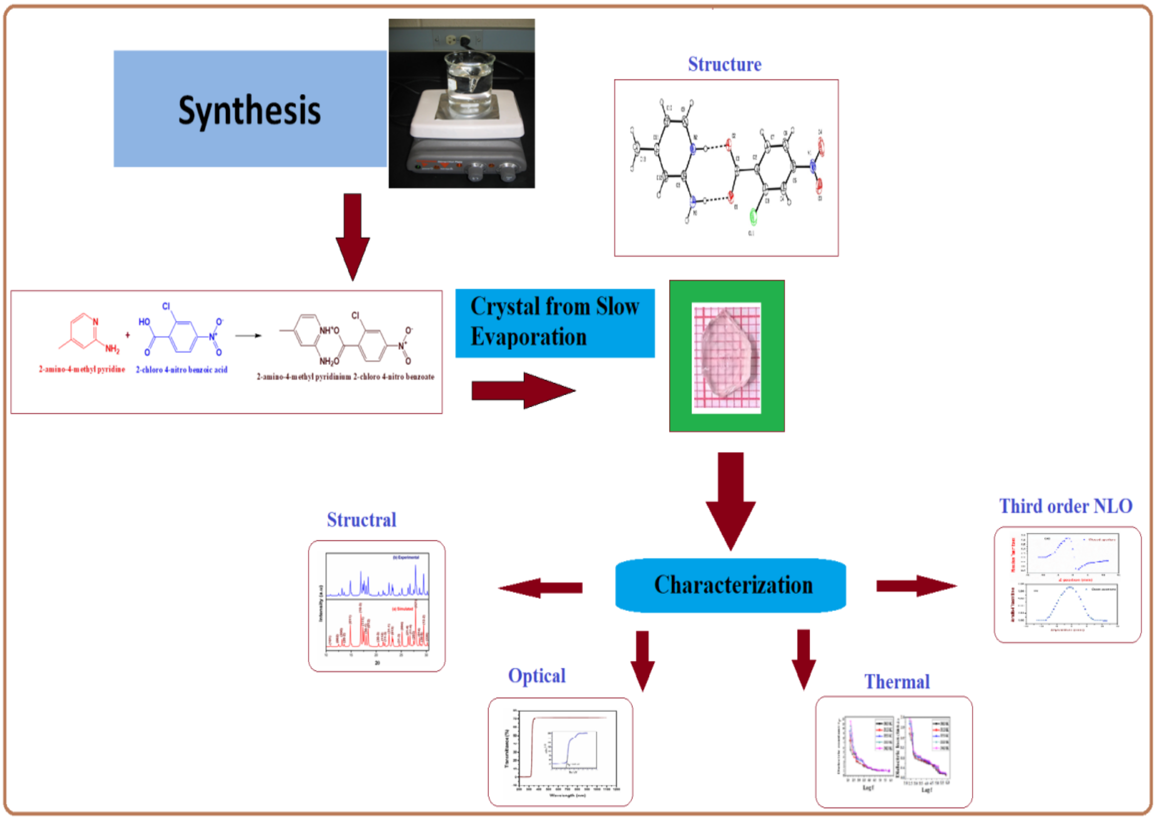

**Fig. 1 (b): Schematic diagram of AMPCNB single crystal**

**Table 1 CHN Analysis of AMPCNB**

| | Nitrogen (%) | Carbon (%) | Hydrogen (%) |
|---|---|---|---|
| Experimental | 13.6132 | 50.5131 | 3.9781 |
| Theoretical | 13.5691 | 50.4230 | 3.9110 |

### *2.2 Nucleation and Crystal growth*

The solubility study of AMPCNB was obtained using ethanol solvent for various saturation values of temperature employing conventional isothermal method by maintaining the cooling rate of 2° C per hour. The saturated solution of the title compound at 30° C was prepared and placed in a bath whose temperature could be monitored and controlled using a programmable temperature controller. During growth process, in order to eliminate spurious nuclei presence, the solution was preheated to 5° C above its saturation temperature for about 24 hours, before the cooling process was initiated. The temperature of equilibrium-saturated solution was then slowly reduced to 30° C with a cooling rate of 3° C/h until a first formed tiny crystal (considered as a nucleation site) was observed [10].

### *2.3 Characterization*

In order to establish that the grown crystal was essentially AMPCNB, a tiny single crystal obtained from spontaneous nucleation process was then subjected to single crystal X-Ray Diffraction method using Enraf-Nonius CAD-4 diffractometer employed with Cu-Kα radiation ($\lambda$ = 0.71073 Å) in the $2\theta$ range 10–79.96° at a scan rate of 0.05° /sec, at ambient temperature. The unit cell parameter determination of AMPCNB crystal was carried out by least-squares technique employing many reflections. The structural refinement of the compound was characterized using full-matrix least-squares method via SHELXL 97. The UV–VIS-NIR transmission spectrum of AMPCNB crystal was recorded using the JASCO V-630 model spectrophotometer (wavelength accuracy ±0.2 nm) [11]. Whereas, Jobin Yvon Fluorometer FL3-11 was employed to record emission and absorption spectra of the compound at room temperature. The refractive index measurement of title compound was carried out using Metricon model 2010/M at wavelength of 632 nm [12]. For the analysis of NLO property in bulk materials, the Z-scan studies were performed using continuous wave Nd: YAG laser beam ($\lambda$= 1064 nm) as an excitation source and it was focused using a lens with focal length of about 3.5 cm. In this study, the crystal sample was translated across the focal region (+z to –z) along the axial direction of a focused laser beam [13]. In open aperture Z-scan, intensity dependent absorption was obtained without placing an aperture at the detector to get data about nonlinear absorption. Whereas, in closed aperture method, transmitted energy is measured when an aperture is placed at far field position to obtain nonlinear refractive index. A photo-detector through aperture collected focused laser beam transmitted through the sample and measured its intensity with the help of a digital power meter [14, 15].

Dielectric studies ($\varepsilon_r$ and tan $\delta$) of AMPCNB were carried out in the frequency range 50 Hz - 5 MHz at various temperatures employing a Hioki LCR 3532-50 LCR meter. In order to provide good ohmic contact, a crystalline sample of typical size of about 6 × 6 × 4 $mm^3$ was selected and a pair of polished flat surface of (10-1) & (-101) crystal planes were coated with silver paste. To act as a parallel plate capacitor, sample (dielectric medium) is inserted between two copper electrodes [16].

## 3. Results and Discussion

### *3.1 X-Ray Diffraction studies*

The single crystal X-ray diffraction data of the title compound were collected at 293 K with graphite–monochromated Mo Kα radiation (λ = 0.71073 Å), and used Enraf–Nonius CAD-4 diffractometer with the ω-2θ scan mode. A suitable sample of size 0.26 mm x 0.21 mm x 0.18 mm was chosen and mounted on the goniometer. The Lattice parameters were collected from least-squares fit of many reflections. Cell refinement and data reduction were carried out using CAD-4 EXPRESS. The structures were solved by direct methods procedure using SHELXS 97 and refined by full-matrix least-squares on F2 using SHELXL -97 programs. The experimental density ($\rho_e$) of the title compound was compared with the theoretical density ($\rho_t$), and the density of AMPCNB was calculated from the expression,

$$\rho_e = \frac{MZ}{NV}$$

Where M is the molar mass, V is the volume of the unit cell and Z is the number of molecules in a single unit cell of the compound [17]. The comparatively good agreement between experimental and theoretical density data values ($\rho_e$ = 1.484 Mg/m$^3$; $\rho_t$ = 1.468 Mg/m$^3$) showed purified nature of the grown crystal. The title compound crystallized in monoclinic space group $P2_1/n$. The unit cell parameters for the crystal of AMPCNB are, a = 14.9230 (9) Å, b = 6.5971 (4) Å, c = 15.7552 (10) Å and α= 90 °, β=116.237, γ= 90 with unit cell volume equal to 1385.94 Å$^3$ and the number of molecules in unit cell was 4 [18]. The ORTEP (Oak Ridge Thermal-Ellipsoid Plot Program) diagram with atom numbering scheme of the AMPCNB crystal structure was shown in the Fig. 2. Table. 2 shows the crystal data and structure refinement of AMPCNB compound.

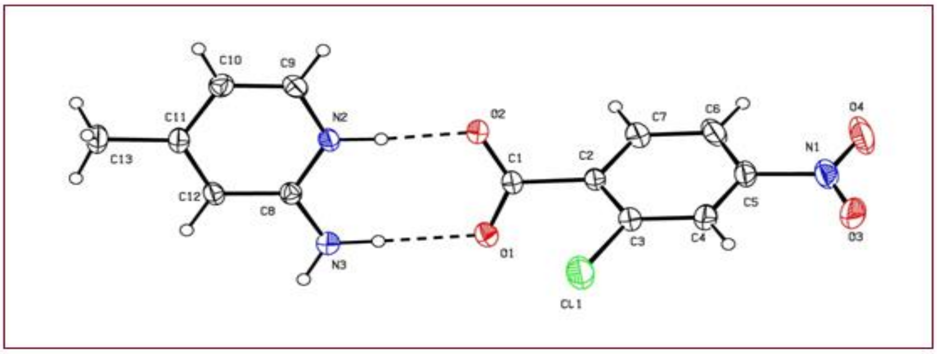

**Fig. 2: ORTEP diagram with atom numbering scheme of the AMPCNB crystal structure**

The planes of various reflections in powder X-ray diffraction data were indexed using mercury software. The indexed powder X-ray diffraction pattern using Mercury software and the experimentally obtained single crystal XRD data are shown in Fig. 3 (a) and 3 (b). The obtained experimental XRD pattern was compared and agreed well with the simulated XRD pattern [19].

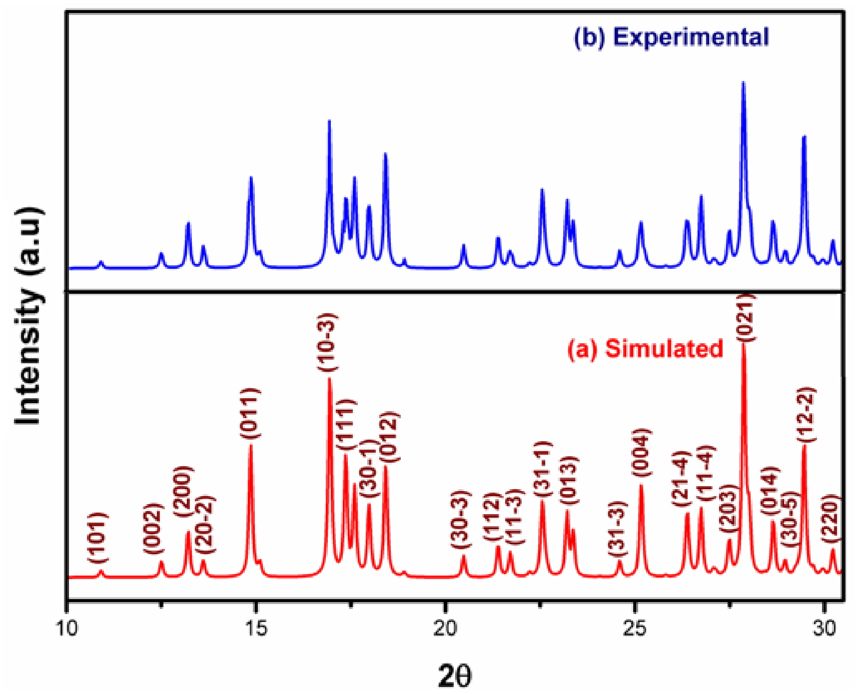

**Fig. 3: (a). Single crystal XRD, (b) Powder XRD plot of AMPCNB.**

### *3.2 Solubility studies*

Solubility curves are the critical parameters for the successful development, optimization and scale-up of a crystallization process. The solubility measurement of a material in any solvent gives indication about the nucleation and availability of the solute material for crystal growth and to decide the cooling rate during the crystal growth. Super saturation is the driving force for the crystallization and it also affects the crystal quality. For growing good quality crystals the solubility of the material should be moderate. From solubility studies, it could be observed that, solubility of the compound in ethanol solvent increases linearly with increase in temperature. Also, positive solubility response of the title compound indicated the possibility of growing large size single crystals via slow cooling and slow evaporation solution growth method [20]. Solubility plot of AMPCNB compound is given in Fig. 4 (a).

**Table 2: Crystal data and Structure Refinement of AMPCNB**

| | | |
|---|---|---|
| Empirical Formula | $C_{13} H_{12} Cl N_3 O_4$ | |
| Formula weight | 309.80 | |
| Temperature | 294 K | |
| Wavelength | 0.71073 Å | |
| Crystal system,<br>space group | MONOCLINIC<br>$P2_1/n$ | |
| Unit cell dimensions | a = 14.9230(9) Å | α=90.000° |
| | b = 6.5971(4) Å | β=116.237(1)° |
| | c = 15.7552(10) Å | ν= 90.000° |

| | |
|---|---|
| Volume | 1385.94 $A^3$ |
| Z, Calculated density | 4, 1.484 $Mg/m^3$ |
| Absorption coefficient | 0.357 mm^-1 |
| F(000) | 642 |
| Crystal size | 0.31 x 0.24 x 0.15 $mm^3$ |
| Theta range | 2.5 to 28.5 deg. |
| Limiting indices | -10<=h<=9, -12<=k<=12, |
| | -10<=l<=10 |
| Reflections collected | 5459 / 2361 [R(int) =0.035] |
| Completeness to θ = 28.5° | 99% |
| Refinement method | Full-matrix least-squares on $F^2$ |
| Data/restraints/ parameters | 2451 / 0 / 168 |
| Goodness-of-fit on F^2 | 1.045 |
| Final R indices | R1 = 0.0317, wR2 = 0.0613 |
| R indices (all data) | R1 = 0.0377, wR2 = 0.061 |
| Largest diff. peak and hole | 0.204 and -262e.A^-3 |

The variation in solubility at various temperatures is shown in Fig. 4. Using above solubility data, bright, transparent and colorless single crystals with average dimension of about 10 x5x 6 $mm^3$ of AMPCNB ($C_{13}H_{12}$ $ClN_3O_4$) were obtained. Fig. 5 (a) and 5 (b) shows grown crystal and morphology of the mentioned compound.

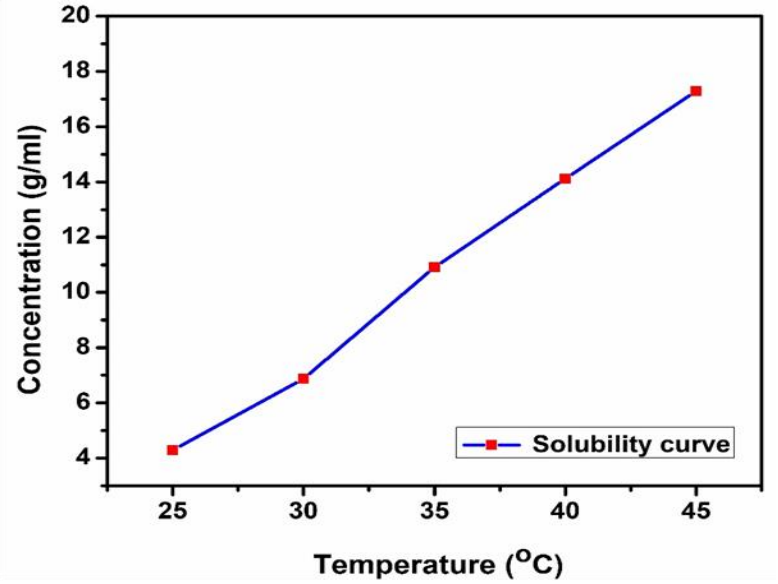

**Fig. 4: Solubility plot of AMPCNB compound**

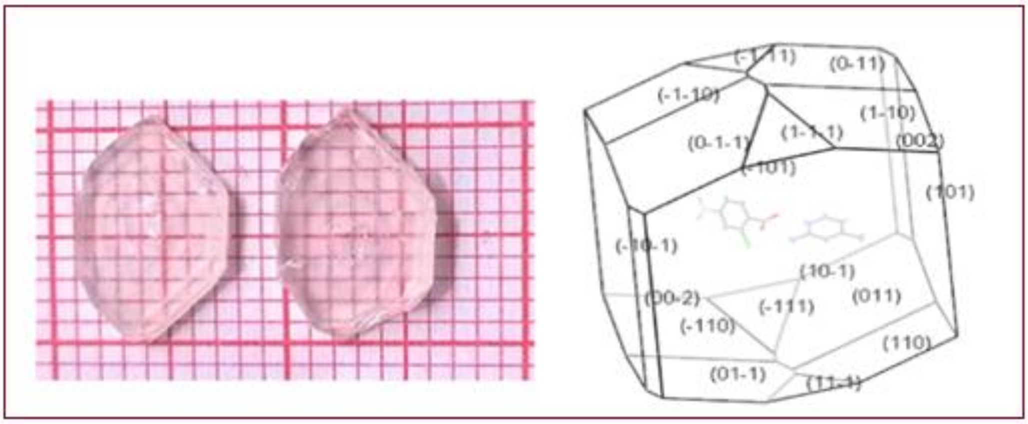

**Fig. 5: (a) Grown crystal, (b) Morphology of AMPCNB**

### *3.3 UV-VIS Spectroscopic studies*

As transmission range and transparency cutoff are most important parameters for NLO crystals, the UV-VIS-NIRspectra were recorded for the crystals in the wavelength region from 200 to 1100 nm using the JASCO V-630 model spectrophotometer. The UV-VIS-NIR transmittance spectrum of title compound is shown in Fig. 6 (a). The lower cutoff wavelength of AMPCNB was observed at 318 nm, due to electron excitation transition from non-binding ‘n’ orbital to antibonding ‘π’ orbital represented as π* (n → π*). From the plot, no absorption has been observed between 318 and 1100 nm. In addition, maximum transparency of about 71%, which indicated AMPCNB crystal, could be useful for NLO applications [21].

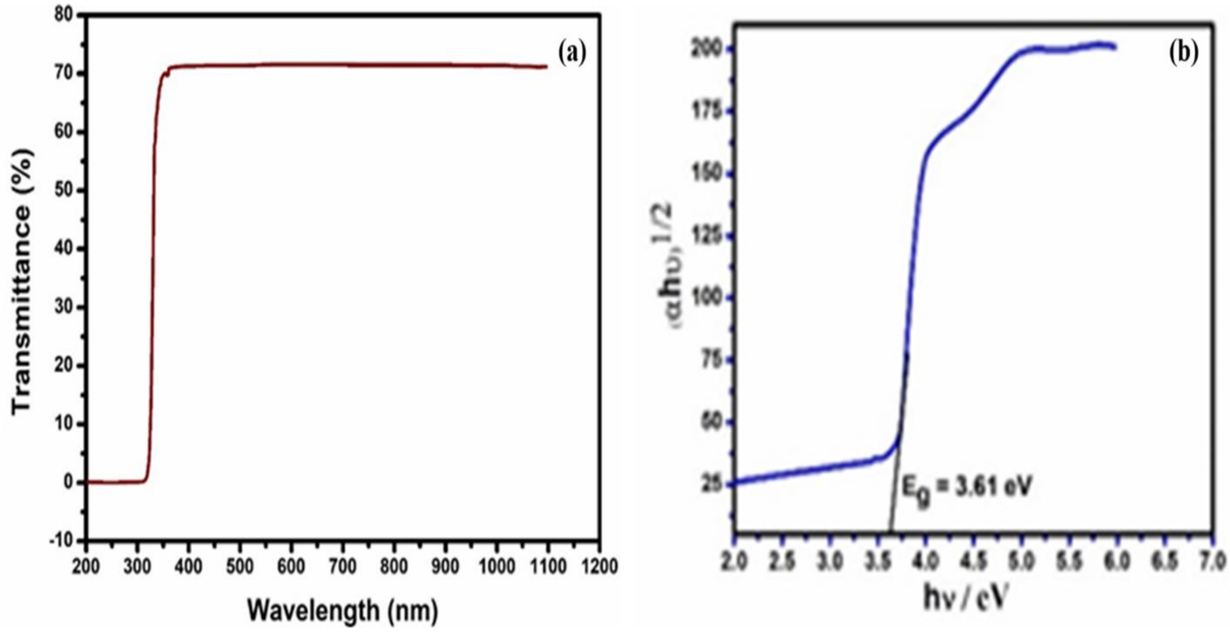

**Fig. 6: (a) UV-Vis-NIR transmittance spectrum, (b) Band gap plot (Inset) of AMPCNB.**

The optical absorption coefficient (α) was calculated by using the transmittance (T) and thickness (d) values of the crystal using the following relation

$$\alpha = \frac{2.303}{d}\log\left(\frac{1}{T}\right)$$

Owing to the direct band gap of the AMPCNB crystal, absorption coefficient (α) obeying the relation for high photon energies (hυ) is given by

$(\alpha h\nu)^n$= A $(E_g - h\nu)$

Where $E_g$ is optical band gap of the crystal and A is a constant. The plot of variation of $(\alpha h\nu)^{1/2}$ vs (hν) is shown in Fig. 6 (b) (as inset). By extrapolating the linear portion of the curve near the start of absorption edge, the optical band gap energy of the crystal was found to be 3.61 eV. As a consequence of this wide band gap, the grown AMPCNB crystal is expected to have high damage threshold and large transmittance in the visible region [22, 23].

### *3.4 Z-Scan Studies*

The analysis of NLO property in bulk materials, the Z-scan experiment were executed using continuous wave Nd: YAG laser beam (λ= 1064 nm) as an excitation source and it was focused using a lens with focal length of about 3.5 cm. A photo-detector through aperture collected focused laser beam transmitted through the sample and measured its intensity with the help of a digital power meter [24].

The plot of closed aperture setup and open aperture set up of AMPCNB as shown in Fig. 7(a) and Fig. 7 (b). The measurable quantity $\Delta T_{p-v}$, is the difference between the peak transmittance and valley transmittance values, $T_p$-$T_v$and is a function of $|\Delta\phi|$ is given by

$$\Delta T_{p-v=0.406\,(1-S)^{0.25}\,|\Delta\phi|}$$

Where$\Delta\phi$ is the on-axis phase shift and S is the linear aperture transmittance and it is given by

$$S = 1 - exp[\frac{-2r_a^2}{\omega_a^2}]$$

Where$r_a$ is the radius of aperture and $\omega_a$ is the beam radius at the aperture. The on axis phase shift ($\Delta\phi$) is related to the third order nonlinear refractive index ($n_2$),

$$n_2 = \frac{\Delta\phi}{kI_0L_{eff}}$$

Where k = 2π/λ, λ is the wavelengthof laser beam used,

α is the linear absorption coefficient,

L is the thickness of the specimen,

$I_0$ is the on-axis irradiance at focus (4.38 KW/cm$^2$)

$L_{eff}$ = [1 – exp ($-\alpha$ L)]/$\alpha$, is the effective thickness of the specimen,

$$L_{eff} = \frac{1 - e^{(-\alpha L)}}{\alpha}$$

Fig. 7(b), shows the Z-scan data related to open aperture arrangement (S=1) of the crystalline sample. The higher transmittance value at focus exhibited the saturated behavior of absorption at higher values of intensity [25]. In closed aperture Z-scan arrangement, due to the saturation behavior of the sample, the peak increased and the valley decreased, as a result symmetry nature of Z-scan curve got changed around Z=0, [26].

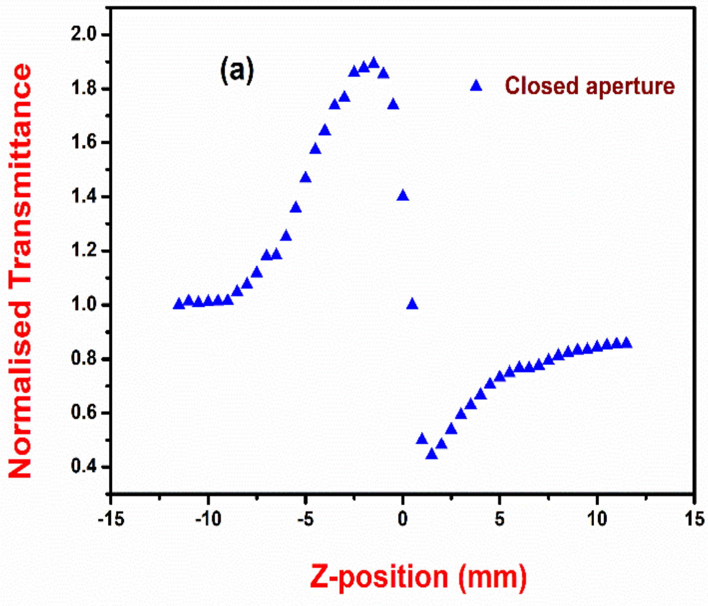

**Fig. 7 (a): Closed aperture Z-scan plot of AMPCNB.**

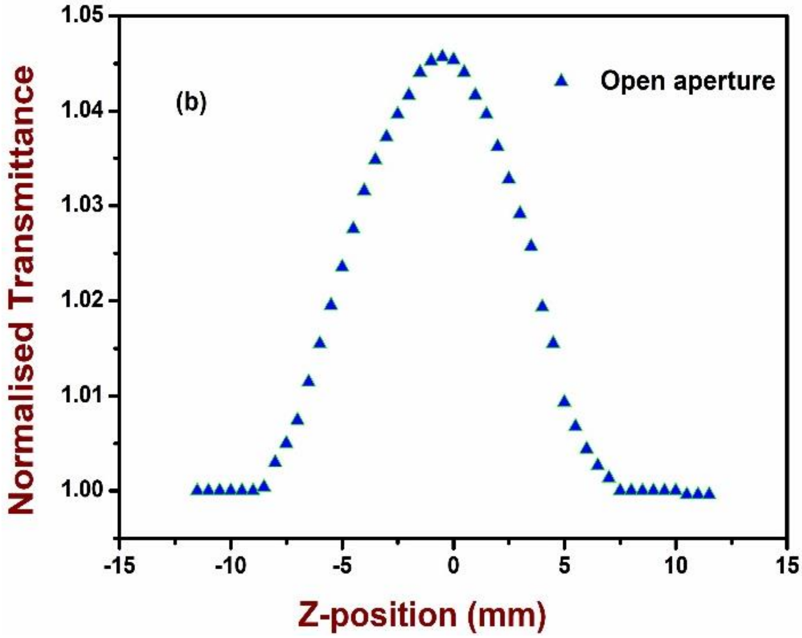

**Fig. 7(b): Open aperture Z-scan plot of AMPCNB.**

From Open aperture Z-scan set up, the nonlinear absorption coefficient can be determined as,

$\beta = \frac{2\sqrt{2}\,\Delta T}{I_0 L_{eff}}$ cm/W$^{-1}$

Herein $\Delta T$ is one valley value at the open aperture Z-scan plot. The real and imaginary parts of the third order nonlinear optical susceptibility could be determined from the experimental calculation of $n_2$ and β according to the following relations,

$$Re\chi^{(3)}(esu) = 10^{-4}\,\frac{(\varepsilon_o C^2 n_o^2 n^2)}{\pi}\left(\frac{cm}{W}\right)$$

$$Im\chi^{(3)}(esu) = 10^{-2}\,\frac{(\varepsilon_o C^2 n_o^2 \lambda\beta)}{4\pi^2}\left(\frac{cm}{W}\right)$$

The absolute value of $\chi^{(3)}$ was calculated from the following relation.

$$\left|\chi^{(3)}\right| = [(Re\chi^{(3)})^2 + (Im\chi^{(3)})^2]^{\frac{1}{2}}$$

The calculated nonlinear refractive index ($n_2$), nonlinear absorption coefficient (β) and third order susceptibility ($\chi^{(3)}$) values of AMPCNB single crystal are 5.610x $10^{-8}$ cm$^2$/W and 0.033x$10^{-4}$ cm/W and 2.942x$10^{-6}$ esu respectively [27]. The value of the nonlinear refractive index indicates the self-defocusing nature of the compound which clearly shows the title compound exhibit negative nonlinear optical properties [28, 29]. The nonlinear absorption exhibited by the specimen could be attributed to its saturation absorption process and this could make the title compound useful for optical limiting applications [30]. The third order nonlinear properties of AMPCNB crystal are provided in the Table. 3.

**Table 3: Third order nonlinear properties of AMPCNB crystal.**

Laser beam wavelength (λ) = 532 nm
Laser power output (P) = 34.3 mw
Lens focal length (f) = 3.5 cm
Optical path distance (Z) = 70 cm
Beam waist ($\omega_o$) = 15.35 µm
Radius of the laser beam ($\omega_L$) = 0.16 mm
Spot size diameter in front of the aperture ($\omega_a$) =15 mm
Aperture radius ( $r_{a)}$ = 2 mm
Effective thickness ($L_{eff}$) =1.13 mm
Diffraction length (Zo) =1.48 mm
Incident intensity at the focus (Z=0) = 4.38 KW/cm$^2$
Nonlinear refractive index ($n_2$) = 5.610 x $10^{-8}$ cm$^2$/W
Nonlinear absorption coefficient (β) = 0.033 x $10^{-4}$ cm/W
Third-order nonlinear susceptibility (χ (3)) = 2.942 x $10^{-6}$ esu

### *3.5 Dielectric studies*

The dielectric properties of the materials are important to know the charge transport phenomena and the lattice dynamics in the crystals. The dielectric behaviour of AMPCNB single crystals was studied using HIOKI 3532-50 LCR Hi-TESTER in the frequency range from 50Hz-5MHz at various temperatures ranging from 303K to 343K. The grown AMPCNB was cut into rectangular dimension and subjected to dielectric studies. To make electrical contacts opposite faces of the crystals were coated with electronic grade silver paint and the electrical contacts were obtained.

The dielectric constant was calculated using the formula,

$$\mathcal{E}_r = \frac{Ct}{A\mathcal{E}_o}$$

The variation of log frequency against dielectric constant at various temperatures is shown in Fig. 8(a). From figure it could be seen that there is exponential decrease in $\mathcal{E}_r$ with increase in frequency and linear increase in $\mathcal{E}_r$ at lower frequency region, revealed contribution of various polarization mechanisms in a solid material [31]. The highest value of dielectric constant ($\mathcal{E}_r$ =11.4) at temperature,T= 343 K was observed at lower frequencies, (f = 500 Hz) could be due to the contribution from all the four types of polarization mechanisms (electronic, ionic, orientation and space charge polarization) [32]. Since, AMPCNB possessed domains of various sizes and differing relaxation times, dielectric constant and loss values decreased gradually with increase in frequency values. The stable low value of of dielectric constant, $\mathcal{E}_r$ = 0.79 at temperature, T= 343 K was observed at f = 5 MHz frequency showed the major contribution of electronic polarization.

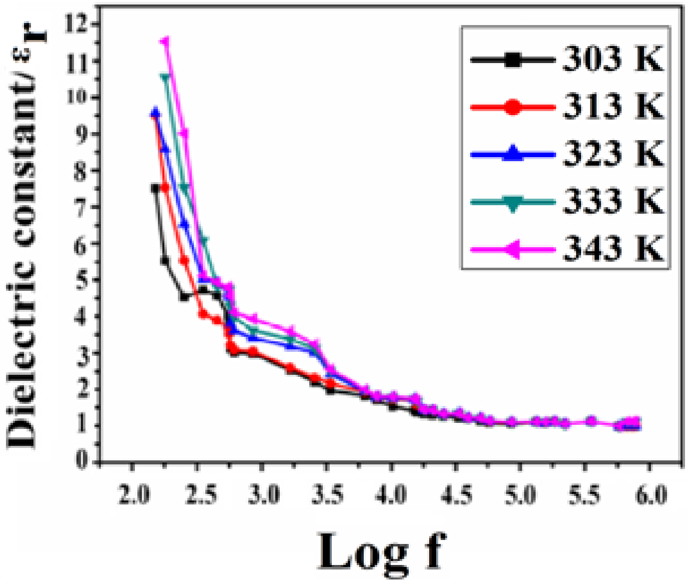

**Fig. 8(a): Variation of Dielectric constant ($\varepsilon_r$) as a function of Log frequency at different temperatures.**

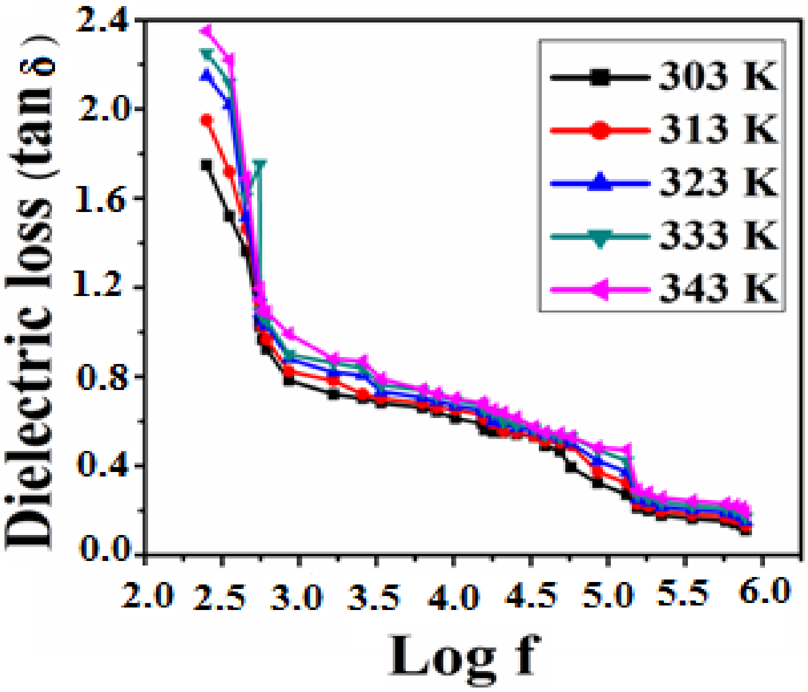

**Fig. 8 (b): Variation of Dielectric loss (tan δ) as a function of Log frequency at different Temperatures.**

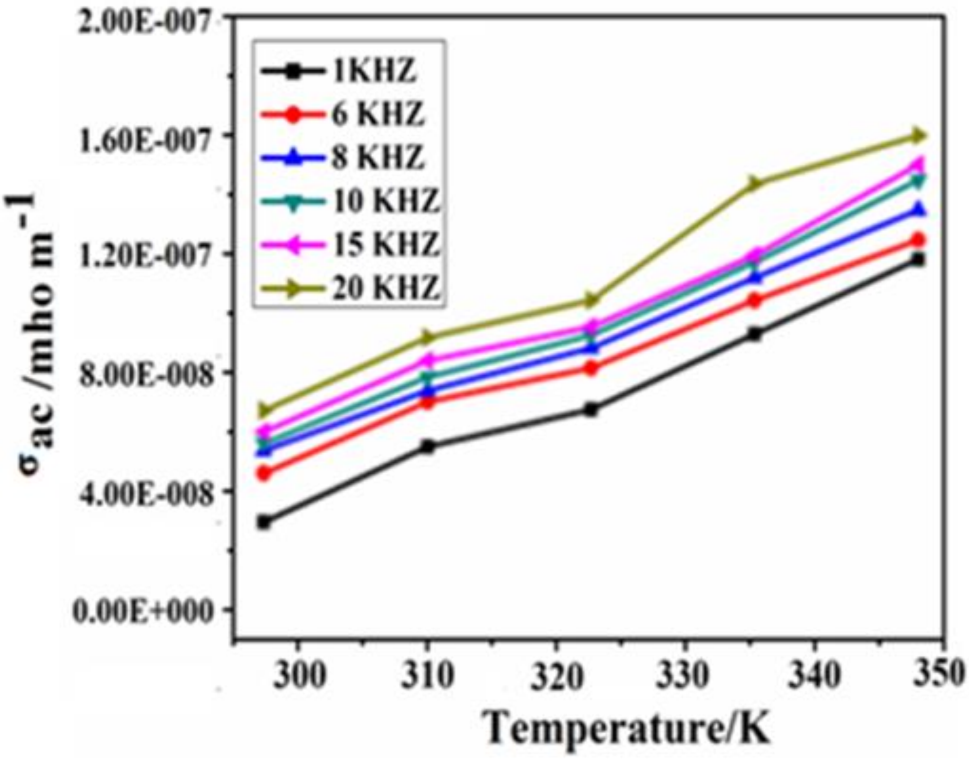

**Fig. 8 (c): Variation of Ac conductivity as a function of Log Frequency at various temperatures.**

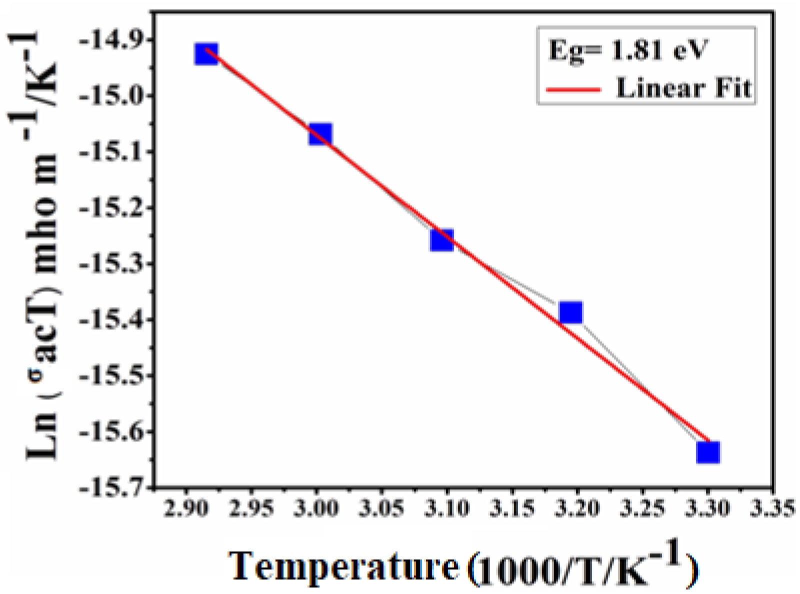

**Fig. 8 (d): Activation Energy of AMPCNB crystal.**

In addition, the lower values of dielectric constant of AMPCNB at higher frequencies indicated the material could possibly exhibit relatively low power dissipation behavior as like other organic NLO crystals, such as NSP, B2AM, 4APM, L-arginine acetate, 4-methyl benzophenone and 2-amino-5-chloro pyridine. Comparision of $\varepsilon_r$ values of different pyridine derivative crystals at T=343K is shown in Table 4. The same trend was observed in the measurement of dielectric loss values as a function of frequency and temperature [Fig. 8(b)]. At lower frequency region, material exhibited higher values of dielectric loss due to space charge polarization [33, 34]. The increase in applied electric field frequency decrease polarization and, as a result dielectric loss values are decreased. The larger value of dielectric loss (tanδ = 2.38) for the title compound is observed for a frequency of 500 Hz at temperature, T= 343 K. However smaller value of loss (tanδ = 0.18) is observed for 5 MHz frequency at 343 K, showed AMPCNB crystal could be a suitable candidate for photonic, optoelectronic and NLO applications [35]. The variation in dielectric loss and dielectric constant with the change in frequency confirmed the title compound under investigation possessed dipoles with continuously varying relaxation times which are not responded to higher frequencies [36]. Further, lower values of dielectric constant at higher frequencies ascertained the presence of lesser number of electrically active defects in the crystal, which facilitated its use in NLO applications [37, 38]. Arrhenius plot drawn between ln $\sigma_{ac}$T and 1000/T for grown AMPCNB crystal is shown in Fig. 8(c). From the figure, it could be observed that, ac conductivity noticeably increases with temperature.

**Table 4: Comparision of dielectric constant values of different pyridine deravitives.**

| **Pyridine derivative** | **Dielectricconstant ( $\varepsilon_r$) at 343 K** | **Reference** |
|---|---|---|
| 2-amino-4-methylpyridinium 2-chloro 4-nitro benzoate | 11.5 | Present work |
| 2-amino-5-chloropyridinium-4-carboxybutanoate | 9.4 | [29] |
| 2-aminomethylpyridinium picrate | 38 | [29] |
| 4-aminopyridinium p-amino benzoate | 420 | [29] |
| Dimethyl amino pyridinium 4-nitro phenolate | 1180 | [29] |

The line of best fit for the plot of ln $\sigma_{ac}$T and 1000/T obeys Arrhenius relationship,

$$\sigma_{ac} = \sigma_o \exp\left(\frac{-E_{ac}}{kT}\right)$$

Where $\sigma_o$ is pre-exponent factor, $E_{ac}$ is the activation energy for the ionic conduction process, k is Boltzmann constant and T is the temperature. Hence, crystal under investigation shows Arrhenius type of conductivity behavior in the above said range of temperature. The calculated activation energy of title compound from Fig. 8(d) due to thermally activated charge transfer process was found to be 1.81 eV, which indicated smaller defect numbers in the title compound [39].

### *3.5.1 Theoretical evaluation of plasma energy, penn gap and Fermi energy and polarisability*

In general, NLO efficiency of a nonlinear optical single crystal is strongly influenced by its electronic properties, thus it is essential to investigate them in detailed manner [40]. Theoretical evaluations indicate that $\varepsilon_r$ at high frequency explicitly depends on valence electron plasma energy, Fermi energy and an average energy gap referred to as Penn gap energy. From the fitting of dielectric constant with Plasmon energy, Penn gap is evaluated for the title crystal.

The valence electron Plasma energy ($\hbar\omega_p$) of AMPCNB is given by,

$$\hbar\omega_p = 28.8 \times \left(\frac{Z\rho}{M}\right)^{1/2}$$

Where Z= $((13Z_C) + (12Z_H) + (3Z_N) + (1Z_{CL}) + (4Z_O))$ = 160 is number of total valence electrons, M is molecular weight and ρ is density of the crystal.

The Penn gap and Fermi energy are given by,

$$E_P = \left(\frac{\hbar\omega_p}{\varepsilon_\infty - 1}\right)^{1/2}$$

$$E_F = 0.2948\ (\hbar\omega p)^{4/3}$$

Molecular Polarizability (α) is calculated using the relation,

$$\alpha = \left[\frac{(\hbar\omega_p)^2\, S_o}{(\hbar\omega_p)^2 S_o + 3E_P^2}\right] \times \left(\frac{M}{\rho}\right) \times 0.396\ \times 10^{-24}\mathrm{cm}^{-1}$$

$$S_o = 1 - \left[\frac{E_F}{4E_F}\right] + \frac{1}{3}\left[\frac{E_F}{4E_F}\right]^2$$

The calculated value of α from penn gap closely agree with that of the Clausius-Mosotti relation,

$$\alpha = \frac{3M}{4\pi N_a\, \rho}\left(\frac{\varepsilon_\infty - 1}{\varepsilon_\infty + 2}\right)$$

All the calculated values of 2A4MP2C4NB are compared with KDP and 2A5BPTA crystals and listed in Table. 5. It is found that the polarizability value of the title compound is comparable with KDP and 2A5BPTA [41].

**Table 5: Theoretical parameters of AMPCNB.**

| **Parameters** | **Values for AMPCNB (Present work)** | **Values for 2A5BPTA [32]** | **Values for KDP [32]** |
|---|---|---|---|
| Plasma energy (eV) | 18.42 | 21.24 | 17.28 |
| Penn gap energy (eV) | 5.559 | 6.132 | 2.37 |
| Fermi energy (eV) | 13.92 | 17.344 | 12.02 |
| Polarizability by Penn analysis | 5.431 x $10^{-23}$ | 5.419 x $10^{-23}$ | 2.14 x $10^{-23}$ |
| By Clausius Mosotti relation | 5.433 x $10^{-23}$ | 5.415 x $10^{-23}$ | 2.10 x $10^{-23}$ |

## 4. Conclusions:

The single crystals of AMPCNB were grown by using solution growth technique. The title compound crystal structure was elucidated using single crystal XRD method and it was concluded that the crystallize in centrosymmetric space group $P2_1/n$.The unit cell parameters for the crystal of AMPCNB are, a = 14.9230 (9) Å, b = 6.5971 (4) Å, c = 15.7552 (10) Å and α= 90 °, β=116.237, γ= 90 with unit cell volume equal to 1385.94 $Å^3$ and the number of molecules in unit cell was 4. The powdered material of the title compound was subjected to microanalysis, powder XRD to further establish the composition, crystalline phase respectively. The refractive index of AMPCNB was determined by employing Brewster's angle method from a He-Ne laser of wavelength, λ=632 nm about 1.4519.Z-Scan studies were carried out the calculated nonlinear refractive index ($n_2$), nonlinear absorption coefficient (β) and third order susceptibility ($\chi^{(3)}$) values of AMPCNB single crystal are 5.610x $10^{-8}$ $cm^2/W$ and 0.033x$10^{-4}$ cm/W and 2.942x$10^{-6}$ esu respectively. Z-Scan studies were carried out to calculate the third order NLO coefficient of AMPCNB confirmed that it exhibited self-defocusing nature. Lower values of dielectric constant at higher frequencies ascertained the presence of lesser number of electrically active defects in the crystal, which facilitated its use in NLO applications. Thus, the above mentioned studies establish that AMPCNB could act as an efficient material for NLO and opto-electronic applications.

**References:**

[1] M.Rajkumar, A.Chandramohan, Synthesis, spectral,thermal, mechanical, and structural characterization of NLO active organic salt crystal: 3, 5 – Dimethylpyrazolium -3 Nitrophthalate, Mater. Lett. 181 (2016) 354 – 357.

[2] K. Senthilkannan, S. Gunasekaran, Spectroscopic Studies and other Novel Stud- ies of 4-Bromo 4′-Chloro Benzylidene Aniline (BCBA) Crystal: A Non Linear Op- tical Material, Int. J. Chemtech Res. 5 (2013) 3051–3058.

[3] S. Anandhi, M. Rajalakshmi, T.S. Shyju, R. Gopalakrishnan, Growth and characterization of an adduct 4-aminobenzoic acid with nicotinic acid, J. Cryst. Growth 318 (2011) 774 – 779.

[4] L. Jothi, G. Vasuki, R. Ramesh Babu, K. Ramamurthi, Synthaeis, Crystal growth and characterization of organic NLO material: 4- Bromo - 4 - hydroxybenzylidene aniline, Optik, 125 (2014) 2017 - 2021.

[5] V. Krishnakumar, R. Nagalakshmi, S. Manohar, M. Piasecki, I.V. Kityk, P.Bragiel,Parametrical optical effects in the 1:1 complex of resorcinol and urea – a nonlinear optical crystal, Phys. B Condens. Matter 405 (2010) 839 – 842.

[6] U.Korkmaz, A. Bulut, 2-Pyridinium propanal hydrogen aquarate: experimental and Computational study of a nonlinear optical material,Spec – trochim. Acta Mol. Biomol. Spectros, 136 (2015) 1058 – 1068.

[7] N.Y. Maharani, A. Cyrac peter, S. Gopinath, S. Tamilvanan, M. Vimalan, I. Venitha Potheher, Growth and characterization of amino based organic nonlinear optical 1-Lysine - 1-Asparate (LLA) single crystal for electro-optic application, J. Mater. Sci. Mater. Eleectron 27 (2016) 5006 - 5015.

[8] P. Muthuraj, M. Sethuram, M.Sethu Raman, M. Dhandapani, G. Amirthaganesan,Synthesis, spectral, thermal, optical, electrical, mechanical, and structural characterization and quantum chemical study of 4 – nitrophenol: Urea molecular adduct crystal, J. Mol. Struct. 1053 (2013) 5 - 14.

[9]. A.Silambarasan, P. Rajesh, P. Ramasamy, Synthesis, growth, structural, optical and thermal properties of an organic single crystal: 4 – Nitroaniline 4 – aminobenzoic acid, Spectrochim. Acta A Mol. Biomol. Spectrosc. 118 (2014) 24 – 27.

[10]. T. Arumanayagam, P. Murugakoothan, Studies on growth, spectral and mechanical properties of new organic NLO crystal: guanidinium 4 – nitrobenzoate (GuNB), J. Cryst. Growth 362 (2013) 304 – 307.

[11]. L. Jothi, R. Ramesh Babu, K. Ramamurthi, Synthesis, growth, and characterization of organic nonlinear optical single crystal of 4 – Bromo-4'- Methyl Benzylidene aniline, Journal of Minarals Characterization and Engineering, 2 (2014) 308 – 318.

[12]. E. Selvakumar, A. Chandramohan, G. Anandha Babu, P. Ramasamy, Synthesis, growth, structural, optical and thermal properties of a new orgamic salt crystal: 3-nitroanilinium trichloroacetate, J. Cryst. Growth 401 (2014) 323 – 326.

[13]. G. Shanmugam, K. Ravikumar, B. Sridhar, S. Baradeeswaran, Synthesis, structure, growth and characterization of novell NLO organic single Crystal: morpholin – 4 –ium p – aminobenzoate, Mater. Res. Bull. 47 (2012) 2315 – 2323.

[14] M. Rajkumar, M. Saravanabhavan, A. Chandramohan, Synthesis, structural, thermal, mechanical, second order harmonic generation efficiency and laser damage threshold studies of 4 – dimethylaminopyridinium-3, 5- dicarboxybenzoate trihydrate single crystal, Opt. Mater. 72 (2017) 247 – 246.

[15] V. Murugesan, M. Saravanabhavan, M. Seker, Synthesis, characterization and pharmacological investigation of a new charge – transfer complex of 3 –aminopyridium p-toluenesulfonate, J. Mol. Struct. 1084 (2015) 95 – 102.

[16] V. Krishnakumara, M. Rajaboopathi, R. Nagalakshmi, Studies on vibrational, dielectric, mechanical and thermal properties of organic nonlinear optical co-crystal: 2, 6 – diaminopyridium – 4 – nitrophenolate – 4- nitrophenol, phys. B 407 (2012) 1119 – 1123.

[17] J. Uma, V. Rajendran, Study of optical, thermal and mechanical properties of trisglycine zinc chloride: a semiorganic non – linear optical single crystal, Arch. Appl. Sci. Res. 5 (2013) 208 - 212.

[18] M. Krishnakumar, S. Karthick, K. Thirupugalmani, S. Brahadeeswaran, Second and third – orderz nonlinear optical and DFT calculations on 2 – amino -5 – chloro pyridinium – l – tartrate: a phasematchablle organic single crystal, Opt. Mater. 66 (2017) 79 - 93.

[19] M. Saravanan, S. Abraham Rajaseker, Growth and characterization of benzaldehyde 4 – nitro phenyl hydrazine (BPH) single crystal: a proficient second order nonlinear optical material, Opt. Mater. 54 (2016) 217 – 218.

[20] G. Shanmugam, S. Brahadeeswaran, Spectroscopic, thermal and mechanical studies on 4 - methylanilinium p – toluenesulfonate – a new organic single crystal, Spectrochim. Acta A, 95 (2012) 177 – 183.

[21] M. Rajkumar, A. Chandramohan, Synthesis, growth, characterization and lase damage threshold studies on N, n – dimethylanilinium - 3 carboxy – 4- hydroxybenzenesulphonate crystal: An efficient SHG material for electro – optic applications, Opt. Mater. 66 (2017) 261 – 270.

[22] E.D. D’silva, G. Krishna Podagatlapalli, S. Venugopal Rao, S.M. Dharmaprakash, Structural, optical and electrical characteristics of a new NLO crystal, Opt. Laser Technol. 44 (2012) 1689–1697.

[23] I. Bryndal, I. Ledoux – Rak, T. Lis, H. Ratajczak, Search for molecular crystals with NLO properties: 5 – sulfosalicyclic acid with nicotinamide and iso – cicotinamide, J. Mol. Struct. 1068 (2014) 74 – 83.

[24] T. C. Sabari Girisun, S. Dhanuskodi, Linear and nonlinear optical properties of tris thiourea zinc sulphate single crystals, cryst. Res. Technol. 12 (2009) 1297 – 1302.

[25] I. P. Bincy, R. Gopalakrishnan, Synthesis, growth and characterization of new organic crystal: 2 – Aminopyridinium p – Toluenessulfonate for thid order nonlinear optical applications, J. Cryst. Growth 3 (2014) 22 – 33.

[26] M. Dhavamurthy, G.Peramaiyan, R. Mohan, Synthesis,growth, structural, optical, thermal, dielectric and mechanical studies if an organic guanidinium p – nitrophenolate crystal, J. Crysta. Growth. 399 (2014) 13 – 18.

[27] S. Jin, X. Lu, D. Chen, Crystal and molecular structure of four 1:1 adducts from 2 – methylquinoline and different acidic components, J. Mol. Struct. 1010 (2012) 17 – 25.

[28] Mohammad Sayed Alam, Dong-Ung Lee, Synthesis, crystal structure, hirshfeld surfaces, fluorescence properties and DFT analysis of hydrazine Schiff bases,Spectrochim. Acta A 145 (2015) 563 – 574.

[29] A. Silambarasan, M. Krishnakumar, A. Thirunavukkarasu, I. Md zahid, R. Mohak Kumar, P.R. Umarani, Studies on growth, spectral. Structural, electrical, optical and mechanical properties of uranium 3-carboxy-4-hydroxybenzenesulfonate single crystal for third-order nonlinear applications,Spectrochim. Acta Mol. Biomol. Spectrosc. 142 (2015) 101 – 109.

[30] R.K. Singh, A.K. singh, DFT calculations on molecular structure, spectral analysis, multiple interactions reactivity, NLO property and molecular docking study of flavanol – 2,4-dinitrophenylhydrazone, J. Mol. Struct. 1129 (2017) 128 – 141.

[31] M. Rajkumar, A. Chandramohan, Synthesis, growth, structural, optical, thermal, electrical and mechanical properties of hydrogen bonded organic salt crystal: triethylammonium-3, 5-dinitrosalicylicate, J. Mol. Struct. 1134 (2017) 762 – 769.

[32] B. Babu, A. Chandrasekeran, R. Thirumurugan, V. Jayaramakrishnan, K. Anitha, Experimental and theoretical investigation on 2-amino 5- bromopyridinium L-tartrate – a new organic charge – transfer crystal for optoelectronics device applications, J. Mater. Sci. Mater Electron. (2017) 1124 – 1135.

[33] G. Shanmugam, K. Thirupugalmani, R. Rakhikrishna, J. Philip, S. Brahadeeswaran, Thermophysical, mechanical and dielectric studies on piperidinium p-hydroxybenzoate, J. Therm. Anal calorium. 114 (2013) 1245 – 1254.

[34] N. Sudharsana, B. Keerthana, R. Nagalakshmi, V. Krishnakumar, L. Guru Prasad, Growth and characterization of hydroxyethylammonium picrate single crystal for third order nonlinear optical appicatioons, Mater. Chem. Phys, 134 (2012) 736 – 746.

[35] I. Vetha Potheher, K. Rajarajan, R. Jeyasekaran, M. Vimalan, F. Yogam, P. Sagayaraj, Growth, optical, thermal and conductivity behavior of nonlinear optical single crystals of CdHg (SCN) 4 ($CH_3OC2H_2O$), J. Therm. Anal. Calorim. 111 (2013) 1491 – 1497.

[36] A. Olajire Adegoke, Analytical, Biochemical and synthetic applications of para-dimethylaminobenzaldehyde, Int. J. Pharm. Sci. Rev. Res.11 (2011) 17 – 29.

[37] N.Sinha, B.K. Sahas, K. Singh, N. Kumar, M.K. Singh, G.C. Gupta, B. Budakoti Kumar, Solution growth and comparative characterization of L-HFB single crystals, Cryst. Res. Technol. 44 (2009) 167 – 172.

[38] V. Shiva Shanker, R. Sanker, R. Siddheswaran, R. Jayavel. P. Murugakoothanan, Growth and characterization of tetra L-lysine alanine mono hydrochloride dehydrate (TLAMHCI), a new semiorganic optical single crystal, and mater. Chem. Phys. 109 (2008) 119 – 124.

[39] T.Daisy Rani, M. Rajkumar, A. Chandramohan, Synthesis, crystal structure, thermal, mechanical and laser damage threshold studies of an NLO sctive organic molecular adduct: 4-acetylpyridine: 4-aminobenzoicacid, Mater. Lett. 222 (2018) 118 – 121.

[40] V. Sivasubaramani, M. Senthil Pandian, K. Boopathi and P. Ramasamy, Crystal growth, structural, optical, thermal, and dielectric studies of nonlinear optical 2-amino-5-nitropyridinium nitrate (2A5NPN) single crystal, Mater. Res. Innovations, (2016) 1 – 9.

[41] V. Venkataramanan, S. Matheswaran, J.N. Sherwood, H.L. Bhat, Crystal growth and physical characterization of a semiorganic bis (thiourea) cadmium chloride, J. Cryst. Growth. 173 (1997) 605 – 610.

# PHYSICAL AND MATERIAL SCIENCE INNOVATION AND ITS SOCIETAL IMPACT

ISBN: 978-93-48620-63-7

## About Editors

Dr. Jitendra Pal Singh, presently working as Assistant Professor Department of Physics, School of Sciences, IFTM University, Moradabad, Uttar Pradesh. He has been teaching since last 10 years. He has published more than 10 Research papers in high impact Journals including SCI, Scopus, WoS indexing. He has 2 patent grants and 6 patent publications. Two scholars are pursuing research in rare earth doped nanomaterials their Ph.D. under his supervision. He is the author of more than 4 books and 23 book chapter written for science and engineering students and working as editorial and reviewer capacity for regular of reputed journals. He awarded Young Research awarded 2024 by IFTM University, Moradabad. He has participated in FDP, conference, workshop and other programmes.

Dr. Atanu Nag, presently working as Associate Professor and Head in the Department of Physics, School of Sciences, IFTM University, Moradabad, Uttar Pradesh. He is a recognized innovation ambassador by the Ministry of Education Innovation Cell and is currently working as the Convener of the Institution's Innovation Council at IFTM University with a mission to develop a robust start-up ecosystem there. He has been teaching since last 17 years. He has published more than 50 Research papers in high impact Journals including SCI, Scopus, WoS indexing and over 40 proceeding papers in conferences. One research scholar had completed her Ph.D. and five scholars are perusing their Ph.D. under his supervision. He is the author of more than 10 books written for engineering and science students and working as editorial and reviewer capacity for regular and special issue of reputed journals and conferences. He had organized two national conferences and many workshops, faculty development programmes as convener or coordinator.

Dr. L. Anandaraj is an Assistant Professor in the Department of Physics at Sacred Heart College (Autonomous), Tirupattur-Dt, Tamilnadu, India. He is having more than ten years of experience in Academic, Research and Innovations. Twenty one Post graduate students completed dissertation in Physics under his supervision. He has published many articles in national and international and conference Proceedings. He presented his work in many national, international conferences and received best paper presentation awards. Dr.L.Anandaraj received "Best Short Invited Lecturer award" from ISCMNB salangor, Malaysia. He organized one national conference. He received dedication and achievements award from Indian Red Cross society.

Dr. Yogesh Kumar Sharma is currently serving as Professor of Physics and Principal at Mahayogi Guru Gorakhnath Government Degree College, Bithyani, Yamkeshwar (Pauri Garhwal), affiliated with Sri Dev Suman Uttarakhand University, New Tehri. With 29 years of teaching experience, Dr. Sharma has held several key positions, including Professor and Head, Department of Physics at SDSUV Rishikesh Campus, Honorary Director at Deen Dayal Upadhyay Kaushal Kendra, Rudrapur, and Senior Scientific Officer at IIT Delhi. He was awarded a Young Scientist Project by DST, Govt. of India. He has guided six Ph.D. scholars and supervised 25 postgraduate dissertations. He completed four major research projects funded by UGC and UCOST and has authored or edited nine books. He has presented papers in 44 conferences and published 60 research articles in reputed journals. Holder of two patents, Dr. Sharma received the 2024 Excellence in Research Award and is a life member of IAPT, IPA, and other scientific societies.

Bhumi Publishing

ISBN 978-93-48620-63-7